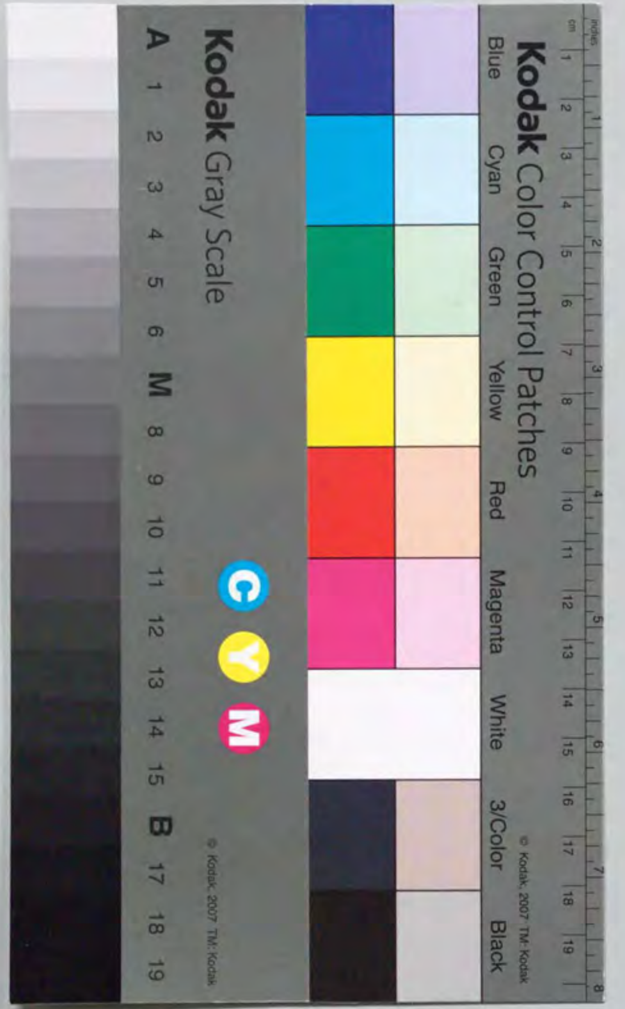

# 対流圏大気の南北半球間交換過程に関する研究

田口彰一

# 対流圏大気の南北半球間交換過程
# に関する研究

1993年12月

田口　彰一

# The study on

# the Inter-Hemispheric Exchange of

# Tropospheric Air Masses

December 1993
Shoichi Taguchi

# Table of Contents

## Abstract

The three-dimensional structural and seasonal variations of the inter-hemispheric exchange processes between the Northern and Southern Hemispheres were studied in order to develop a tropospheric chemical transport model (CTM). A global atmospheric transport model (ATM) and a Lagrangian trajectory model (LTM) were developed using twice daily three-dimensional wind fields analyzed at the European Centre for Medium-Range Weather Forecasts (TAGA Basic, 1989). A CTM was developed incorporating a simple planetary boundary layer and chemical reactions using meteorological data reported every 6 hour (TOGA Advanced, 1992). The three-dimensional distribution of carbon dioxide ($CO_2$) was studied to evaluate the planetary boundary layer (PBL)formulations. The three-dimensional distributions of methyl chloroform (trichloroethane; $CH_3CCl_3$ ) and methane ( $CH_4$ ) were used to evaluate the performance of the CTM.

A compositional gradient zone (CGZ) associated with the Inter Tropical Convergence Zone (ITCZ) between the Northern and Southern Hemisphere were observed in the lower troposphere of the ATM. A partial barrier between the Northern and Southern Hemispheric air masses was observed in the distribution of the extrema of the latitudes of trajectories during the 30 days of integration in the LTM and is consistent with the CGZ in the ATM. The CGZ coincided with the ITCZ in the Pacific throughout the year and shifted to 30°N in Asia in the northern summer and to 30°S in South America in the northern winter.

Although upper tropospheric trajectories crossed the CGZ both in January and July, there was an asymmetry for trajectories passing between hemispheres in the lower troposphere. Trajectories from the summer hemisphere to the winter hemisphere went via the lower troposphere in the tropics then they were lifted in the tropics. Those from the winter hemisphere to the summer hemisphere crossed the CGZ only in the lower troposphere.

PBL effects in the CTM were investigated using a current estimate of the sources and sinks of $CO_2$ due to fossil fuel combustion ( fossil run) and land ecosystem ( vegetation run). The annual mean surface concentration in the vegetation run was sensitive to the formulation of the PBL.

The interhemispheric exchange time between the Northern and Southern Hemispheres in the ATM was about one year, although the ATM includes neither vertical mass transport nor horizontal diffusion arising from cumulus convection. The interhemispheric exchange time in the CTM was also about one year, even though the meteorological data in the CTM are reported every 6 hours, rather than every 12 hours as used in the ATM.

The inter-hemispheric gradient of methyl chloroform was about 25pptv, which is consistent with the Atmospheric Lifetime Experiment (ALE/GAGE) data. The global average hydroxyl radical concentration required to reproduce the inter-annual trend as observed by the ALE/GAGE was $4.7x10^{5}(molecules/cm^{3)}$. The inter-annual trend of $CH_4$ as reported by the Climate Monitoring and Diagnostics Laboratory (CMDL) was well simulated by using the required amount of the OH radical, adjusted for methyl chloroform's inter-annual trend and a 524 Tg/year source of methane. However, the seasonal variation of all sites, except at the highest northern hemisphere latitudes, was modeled successfully. The interhemispheric contrast was not large enough and the base amount in the southern hemisphere was larger than observed.

Based on these experiments, we can conclude that the CTM represents atmospheric transport precisely and has a potential capability to assess the the source strength of minor constituents.

# Chapter 1: General Introduction

## 1. Atmospheric composition

Nitrogen and Oxygen occupy 99% of the atmosphere in volume and they are transparent to infrared radiation. On the other hand, other constituents, such as water vapor, $CO_2$ and $CH_4$, have global warming effects due to their absorption of infrared radiation, and have an important role in maintaining the atmospheric temperature. The amount of the minor constituents changes with natural variation of the solar-earth system as well as human activities. Global warming is predicted in the next century due to the increase of these minor constituents.

In spite of the importance of the concentration of the minor constituents in the atmosphere, our knowledge of their sources and sinks shows significant uncertainty. Furthermore, to evaluate human activities on the atmospheric environment, we have to synthesize all the processes connecting the sources and sinks with the receptor: emission, transport, chemical and physical modification and deposition.

Some aspects of the transport of the minor constituents are illustrated in Figure 1. The atmosphere can be divided into PBL, Troposphere and Stratosphere. The constituents released from the surface are injected into the PBL. Inside the PBL, the concentration is well within a few hours. The time scale of the exchange between PBL and free troposphere ranges from a few hours to few days, depending on the strength of the stratification of the inversion layer at the top of the PBL. The concentrations of some minor constituents, such as $CO_2$ or Chlorofluorocarbons (CFCs), indicate that the exchange rate of the air in the Northern Hemisphere and that in the Southern Hemisphere is about one year (Keeling, 1960, Prather *et al.*, 1987). The stratosphere and troposphere are divided by the tropopause, and the exchange rate through the tropopause is estimated as two years, in terms of the turn over time of the stratospheric air. Observation of the concentration of the minor constituents in remote areas from the source may be interpreted if the above mentioned transport process is taken into account in a model.

The amount released into the atmosphere is known for some constituents, such as CFCs and sulphur hexafluoride ($\mathbf{SF}_6$), because they are purely artificial products. The concentrations of CFCs have been observed in ALE/GAGE, and have been used to evaluate or calibrate the atmospheric transport models (Prather *ed.* 1990), although there are uncertainties in their lifetimes (Kaye *et al.*, 1994). The observation of the concentration of $\mathbf{SF}_6$ have been accumulated (Maiss and Levin, 1994), and may be used to evaluate the transport model in the future, because the atmospheric life time of $\mathbf{SF}_6$ is 3200 years.

Stable $^{14}C$ isotopes are created in the upper atmosphere, due to cosmic radiation, and are used to calibrate the mass transfer rate between the stratosphere and the troposphere. Stable $^{222}\mathbf{Rn}$ isotopes are released from the soil and are used to calibrate the mass exchange rate between the planetary boundary layer and the free troposphere (Heimann and Keeling, 1989), although the observation of $^{222}\mathbf{Rn}$ is not enough, in terms of the coverage of the area and seasons.

The size of sources and sinks of some constituents are not well known, such as Krypton-85 ( $^{85}\mathbf{Kr}$), $CO_2$ and $CH_4$. In the reprocessing of nuclear fuel waste products, $^{85}\mathbf{Kr}$ is released into the atmosphere and its mean life time is 15.6 years. Although the source distribution was not known well in the former Soviet Union, the concentration of $^{85}\mathbf{Kr}$ was used to calibrate the atmospheric transport model (Heimann and Keeling, 1989, Zimmermann *et al.*, 1989) when the data of CFCs were not available.

Atmospheric concentration of $CO_2$ has increased since the industrial revolution. The emission of $CO_2$ due to combustion of fossil fuel is estimated as 5 to 6 GtC per year, and 3GtC remains in the atmosphere. We do not know the fate of the remaining 2GtC. The surface concentration of the atmospheric $CO_2$ has a seasonal peak to peak cycle of 5 ppm in the Northern Hemisphere and 0.5 ppm in the Southern Hemisphere. Resent observations of stable isotopes (Nakazawa *et al.*, 1993) indicate that the seasonal variation of the $CO_2$ concentration in the west Pacific can be explained only with the biological activity over the land. This seasonal variation has made the detection of the so-called missing $CO_2$ sink difficult, due to the complex distribution of the sources and sinks and their irregular variation with time.

Minor Constituents in the atmosphere

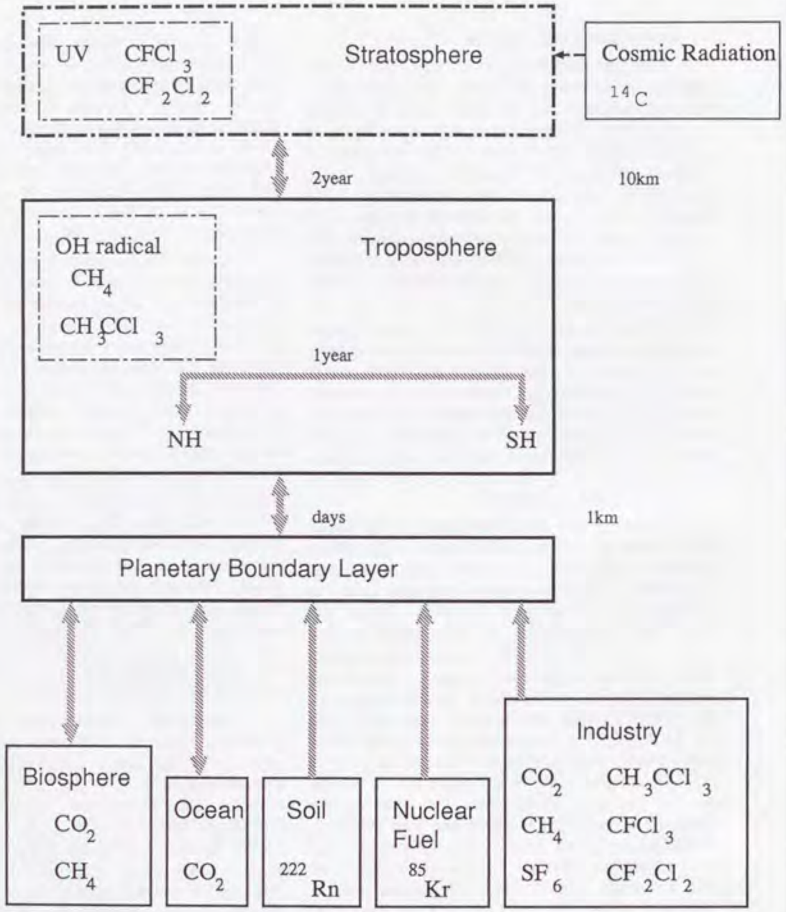

Fig.1 Minor constituents in the atmosphere. The atmosphere can be divided into three parts in the vertical direction: PBL, troposphere and stratosphere. The troposphere can be devided into two parts near the Equator: the Northern and Southern Hemisphere.

The amount of $CH_4$ in the atmosphere is increasing but the source distribution is not well known. In 1990's, this increase has stopped but there is no explanation for this phenomena because of the lack of knowledge about $CH_4$ sources. The major removal mechanism of $CH_4$ is a reaction with the OH radical,

$$CH_4+OH \rightarrow CH_3+H_2 \quad (1)$$

Both the estimates of the sources of methane in the atmosphere and the rate of its removal have large uncertainties ( Taylor *et al.*, 1991 ; Fung *et al.*, 1991).

The OH radical is also the most important factor in the removal of methyl chloroform in the troposphere,

$$CH_3CCl_3+OH \rightarrow CH_2CCl_3+H_2O. \quad (2)$$

Since the source strength of methyl chloroform is relatively well known, it is sometimes used to estimate the global OH radical concentration (Prinn *et al.*, 1992, etc.).

For a minor constituent with a life time longer than one year, an interhemispheric exchange process between the Northern and Southern Hemisphere in the troposphere is a key factor in determining its current global distribution, while the understanding of this process is very limited because of the poor meteorological data in the tropics. Recent improvements in the quality of the meteorological data may make it possible to study this process. This study attempts to resolve the interhemispheric exchange process through the tropics using the best meteorological data set available. Based on the results of the interhemispheric transport, a global transport model is used to reproduce the current distribution of some minor constituents.

## 2. Transport of trace constituents between hemispheres

Earlier observations of minor constituents (Keeling, 1960: Newell *et al.*, 1974) have already identified a compositional gradient zone or a mixing barrier in the lower latitudes, around the Inter Tropical Convergence Zone (ITCZ). Halter *et al.*, (1988) showed that the variability of atmospheric $CO_2$ at American Samoa (14° S, 171° W) was the result of alternating influences of air masses from separate source regions. They suggested that the ITCZ and South Pacific Convergence Zone (SPCZ) function as barriers. Prinn *et al.*, (1992) showed that the variation of concentration of methyl chloroform at American Samoa shows a remarkable sensitivity to the El Nino-Southern Oscillation (ENSO). Although the position of the barrier over the oceans has been extensively studied, its position is not known in the upper part of the atmosphere, nor over land.

## 3. Exchange Through the Barrier

Junge (1962) discussed the interhemispheric exchange rate based on $CO_2$ data published by Keeling (1960) and on data published by Bishop *et al.*, (1961) on tritium content in methane. Junge(1962) estimated an interhemispheric exchange time of about one year, based on the amplitudes of seasonal variations in $CO_2$ concentration in the Northern and Southern Hemispheres. Newell *et al.* (1969) studied the interhemispheric exchange processes using meteorological data and the distribution of ozone. Newell *et al.* (1974) later extended their study to include the distribution of CO. Czeplak and Junge (1974) summarized interhemispheric exchange times estimated from several species. The exchange times varied greatly, from 0.7 to 4.4 years, depending on the species and the estimation method.

The strength of the interhemispheric exchange is critical in the distribution of minor constituents in each hemisphere. Even for the simplest framework of a reaction between two constituents, such as methane or methyl chloroform and the hydroxyl(OH) radical, the interhemispheric exchange time may affect the global distribution of the OH radical. The OH radical concentration and distribution are therefore adjusted for different transport models. (Spivakovsky, *et al.* 1990, Hartley and Prinn, 1991, Cunnold and Prinn, 1991).

The seasonal variation of the exchange strength and transport paths between the hemispheres are also important factors that affects the concentration of minor constituents in the atmosphere. Pearman and Hyson (1980) suggested that the correlation which exists between the release and the absorption of $CO_2$ due to biological activity, and that the strength of the interhemispheric exchange may indicate a net flux from one hemisphere to another.

Despite the work discussed above, the actual exchange mechanism has not been clearly understood because of unreliable wind data in the tropics. Newell *et al.* (1969) showed the importance of the upper tropospheric transport in the tropics, based on the large value of the mean meridional circulation (indicating a high level of transport) and on the standard deviation of the meridional component of the wind (indicating a high level of dispersion) in the upper troposphere. Yamazaki and Chiba (1992) investigated the interhemispheric exchange process using a semi-Lagrangian model combined with a GCM. Yamazaki (1992) investigated the interhemispheric exchange process using a global Lagrangian model with observed wind fields. Both studies indicated the importance of the exchange in the upper part of the troposphere. However, because both studies are restricted to the analyses of the zonal mean, the horizontal distribution of exchange paths remains unclear.

## 4. Model

Among the global three dimensional transport models, only models which made a comparison with observations of tropospheric concentration of any species are listed in Table 1. The order of appearance in the literature is approximately reflected in the order in the list. The first two appeared in 1970's. Models after the number eight appeared in 1990's. The last line shows the present study.

The Euler method corresponds to a finite difference method including spectral representations of the mixing ratio. A slope method, that is alternatively called second order momentum methods, was used in the GISS transport models (3,4,5,8,9). The Lagrangian method means a large number of particles are traced in the model. The Semi-Lagrange method uses back trajectory of a particle at each time step at each grid point to estimate the mixing ratio at a grid point.

As the continuous observation of the concentrations were accumulated, many attempts were made to adjust the model transport with the observation, using known source strengths. One reason for the wide use of GISS/Harvard model may be the functionality for the adjustment of the interhemispheric exchange time using horizontal diffusion. Prather *et al.,* (1987) simulated the global distribution and temporal variability of chlorofluorocarbons (CFCs) using the original GISS model. They found that interhemispheric transport rates for trace gases, as resolved by the parent GCM, were too slow to account for the CFC concentration observed in the Southern Hemisphere. They adjusted the interhemispheric transport time of the model by scaling diffusion rates in the tropics.

Despite its attractive features, the GISS transport model has a strong limitation in its application because it uses the wind field generated by the GISS climate model. Heimann and Keeling (1989) simulated atmospheric $CO_2$ and $^{13}C/^{12}C$ using the GISS/SIO model, in combination with observed wind field data derived from the First GARP Global Experiment (FGGE). They adjusted the interhemispheric exchange time to 1.3 years by reducing the strength of convection in the model by half.

Taylor (1989) simulated the global distribution of $CO_2$ and Taylor *et al.,* (1991) simulated the global distribution of methane using a Lagrangian transport model, combined with 5-years of atmospheric analyses from the ECMWF. Their interhemispheric exchange time was 1.2 years and required no adjustment.

Kao *et al.,* (1992) simulated global CFC11(**$CFCl_3$**) concentration using the Los Alamos chemical tracer model. They showed that simulated amounts of CFC11 at Samoa and Tasmania are sensitive to the interhemispheric exchange time.

A global material transport model may be created with either on-line or off-line methods. ("Off-line" means that meteorological information relating to tracer transport is taken from the GCM and used in a different model). The transport model may be constructed in either Eulerian (Hunt and Manabe, 1968, etc.) or Lagrangian form (Taylor *et al.,* 1991; etc.) A semi-Lagrangian form of the transport model has also been used by Yamazaki and Chiba (1992) and Hartley *et al.,* (1993). A review of the development of transport models is given by Brasseur and Madronich (1992). In this work, three off-line models have been developed, one in Lagrangian and two semi-Lagrangian form, in order to make use of recently improved meteorological analysis data.

## 5. Meteorological Data

Global gridded meteorological data has been available since the First Global GARP Experiment (FGGE), conducted from late 1978 to the end of 1979. The ECMWF compiled the FGGE-IIIb data using a four dimensional data assimilation system (Bengtsson, *et al.,* 1983). In this system, data at grid points where observations are sparse are filled with the data generated by a numerical weather prediction system.

| No | CODE | Scheme | User(constituent) | Wind | mode |
|---|---|---|---|---|---|
| 1 | GFDL | Euler | Rayner ($CO_2$) | GFDL GCM | off |
| 2 | MIT | Euler | Golombek(CFC) | Cunnold GCM | off |
| 3 | GISS | Slope | Fung($CO_2$) | GISS GCM | off |
| 4 | GISS | Slope | Prather(CFC), Jacob(85Kr) | GISS GCM | off |
| - | /Harvard | - | Spivakovsky(OH,$CH_3CCl_3$) | - | - |
| - | - | - | Fung($CO_2$,$CH_4$) | - | - |
| 5 | GISS/SIO | Slope | Heimann($CO_2$) | ECMWF/FGGE | off |
| 6 | MPI | Euler | Zimmerman ($^{85}Kr$) | Oort | off |
| 7 | ANU | Lagrange | Taylor($CO_2$,$CH_4$) | ECMWF/WMO | off |
| 8 | GISS/Ta | Slope | Tans($CO_2$) | GISS GCM | off |
| 9 | MPI/TM2 | Slope | Heimann($^{222}Rn$,$CO_2$,CFC) | ECMWF/WMO | off |
| 10 | LANL | Euler | Kao(CFC) | LANL GCM | on |
| 11 | LLNL | Lagrange | Penner(CFC) | CCM1(NCAR) | off |
| 12 | CCM2 | Semi-Lag | Hartley(CFC),Erikson($CO_2$) | CCM2(NCAR) | on |
| 13 | NIRE | Semi-Lag | Taguchi($CH_3CCl_3$,$CH_4$,$CO_2$) | ECMWF/TOGA | off |

Table 1. List of the global three dimensional trace transport models. Each row shows the name of the organization (or the name of the model, if appropriate), the numerical scheme used to calculate the transport, the name of the user of the model and the constituent(s) investigated, the wind field used, and calculational mode: on or off line. The abbreviations of the institutions are listed in the appendix.

Table 2 lists the data set released from the ECMWF, including data yet to be released (ECMWF Newsletter December 1993, ECMWF 1994).

The quality of the data vary in each archive. Figure 2 ( copied from Trenberth 1992, Figure 35) shows the zonally averaged vertical velocity at 500 hPa for two data set of ECMWF: (a) WMO and (b) TOGA. In both figures, the vertical velocity increased significantly, probably not due to natural variation, but to the ECMWF analysis procedure. During 1985 to 1989, the zonal mean omega is confined in more narrow region in the TOGA archive than in WMO archive. In May 1989, significant changes were observed in both archives when the vertical mass flux scheme was introduced in the physical parameterization of the ECMWF numerical prediction model. The re-analysis project (ERA) has been conducted at the ECMWF to respond to the request from researchers for a data set with a homogeneous quality. They are not yet available.

The following chapter contains a discussion of the atmospheric barriers in the tropics and the atmospheric exchange of mass between hemispheres in the ATM. In chapter 3, the same subjects are discussed for the LTM. In chapter 4, CTM is described in detail and the result of $CO_2$ simulation is discussed. Simulations of $CH_3CCl_3$ and $CH_4$ are performed with the CTM and the results are compared with ALE/GAGE and CMDL observation network in chapter 5. Conclusions are summarized in chapter 6.

| Name | NM-init | H-res. | V-res. | Int. | period |
|---|---|---|---|---|---|
| FGGE-IIIb | initialized | 2.5 | 14 | 12H | 1978/Dec - 1979 |
| WMO | initialized | 2.5 | 7 | 12H | 1978/Dec - 1989 |
| FGGE-SOP-A | non-init | 1.875 | 15 | 6H | 1979/Feb and 1989/June |
| FGGE-SOP-B | initialized | 1.875 | 19 | 6H | 1979/Feb and 1989/June |
| TOGA/Basic | non-init | 2.5 | 15 | 12H | 1985-now |
| TOGA/Advanced | non-init | 0.5 | 15 | 6H | 1989-now |
| ERA | non-init | 0.5 | 15 | 6H | 1979-1994 |

Table 2. List of ECMWF archive. SOP stands for the special observation periods. TOGA is the tropical ocean and global atmosphere. ERA is the ECMWF Re-analysis Data. For details of the evolution of the data, refer to the description of the data given from the ECMWF.

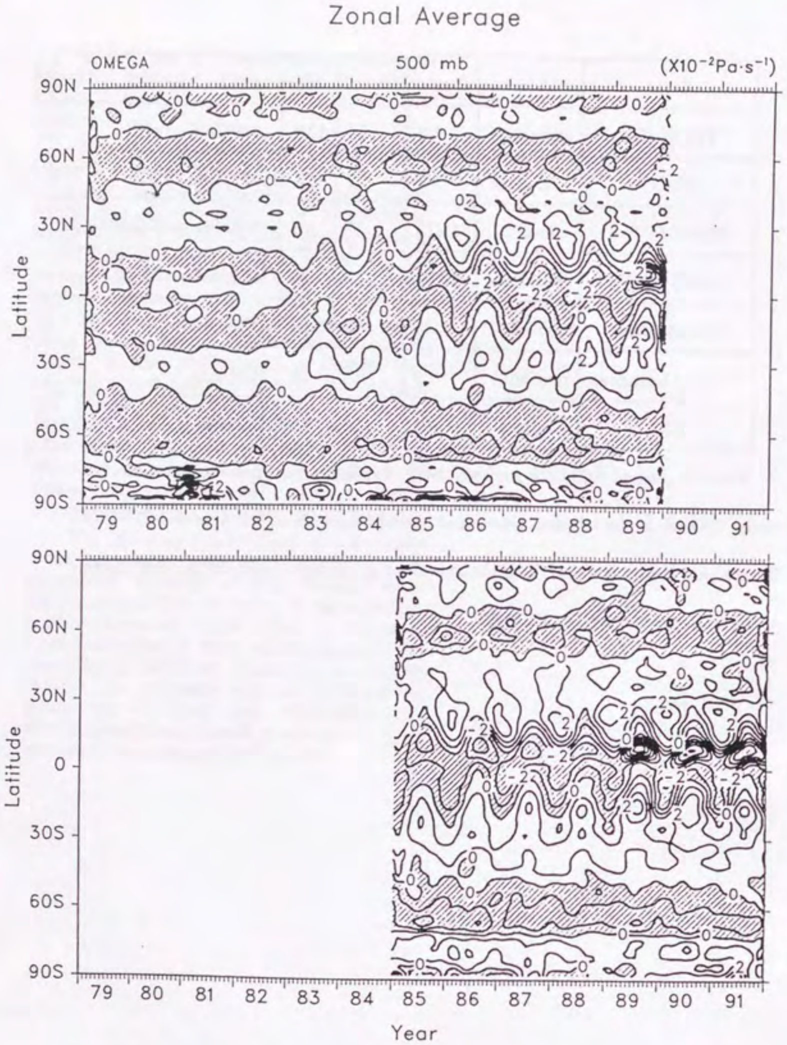

**Fig.2** Latitude-time series of monthly and zonal means of $\omega$ at 500 hPa in $10^{-2}$Pas$^{-1}$ from the WMO archive( initialized)(top) and from TOGA archive (uninitialized)(bottom) (from Trenberth, 1992).

# Chapter 2 : Interhemispheric Exchange in the Troposphere by an Atmospheric Transport Model.

## Abstract

A global atmospheric transport model was developed using a simple semi-Lagrangian method and the inter-hemispheric exchange was investigated. The time evolution of the mixing ratio of an artificial tracer at grid points with resolution of 2.5° horizontal and 14 vertical pressure levels is obtained using three-dimensional wind fields analyzed at the European Centre for Medium Range Weather Forecasts.

A steep horizontal gradient zone was observed in the equatorial region of the lower troposphere and indicates a boundary between the hemispheres. The latitude of this boundary changed with longitude and the seasons; it was located north of the equator, on the average. The boundary coincided with the Inter Tropical Convergence Zone in the Pacific throughout the year and shifted to 30°N in Asia in the northern summer and to 30°S in South America in the northern winter.

Monthly flux of mass across this zone was estimated. The maximum mass exchange from south to north occurred in December and the minimum in May; the maximum from north to south was in May and the minimum in October. The interhemispheric exchange time was about one year.

The results of this experiment suggest that sources and sinks of atmospheric constituents along the Indo-China peninsula may affect air quality in the Southern Hemisphere during the northern summer while such sources and sinks in the Amazon Basin may affect air quality in the Northern Hemisphere during the northern winter.

## 1. Introduction

Air mass exchange between the Northern and Southern Hemispheres is slow compared with the diffusion inside each Hemisphere. The spatial variation of the mixing strength can be recognized by a steep compositional gradient zone (CGZ) that divides the Hemispheric air masses near the equator. Intermittent fluctuations of this zone account for the daily variations of minor constituents as shown in American Samoa by Halter *et al.* (1988).

Let us consider the formation of the CGZ in detail. If the contribution of sources and sinks is negligible when compared with the initial distribution, then the CGZ is formed as a result of different mixing strengths as well as initial conditions. In horizontal shear situations, when transport is faster than mixing along the shear boundary, the transported air-mass maintains its characteristics and forms the CGZ as it moves. When mixing is dominant, individual air masses of different compositions cannot be identified. Transport and dispersion are defined by an averaging procedure. If the average time is very long or the area very wide, then mixing may dominate transport in an observation. If air motions can be resolved precisely, then it is not necessary to worry about diffusion because mixing is described by wind fields. In summary, the reproduction of the CGZ in a simulation depends on the space and time resolution of transport wind fields.

The importance of the CGZ between Hemispheric air masses has been recognized since the 1970's because the interhemispheric exchange time was used as an indicator of transport model performance. Czeplak and Junge (1974) compared a two-box model with a large scale diffusion model and concluded that "it is quite realistic to approximate the troposphere with respect to inter-hemispheric exchange by a two-box model." They used tracer gas data and obtained an estimate of one year for an exchange time. Global transport of chemical constituents has been studied extensively for the Atmospheric Life Time Experiment (ALE) (Prinn *et al.*, 1987). Prather *et al.* (1987) investigated global transport by following fluorocarbon distributions using a three-dimensional chemical transport model with wind derived from a GCM developed at the Goddard Institute for Space Studies (GISS). Subgrid scale diffusion was necessary for their model to reproduce the observed inter-hemispheric exchange. Jacob *et al.* (1987) investigated the global distribution of $^{85}Kr$ using the same model as Prather *et al.* (1987). They obtained an interhemispheric exchange time of 1.1 years. Taylor *et al.* (1991) investigated methane sources using a particle diffusion model driven by the 7 layer wind fields analyzed by the European Centre for Medium Range Weather Forecasts (ECMWF). Their interhemispheric exchange time was 1.2 years. Heimann and Keeling (1989) investigated the global circulation of carbon dioxide with a global transport model driven by the observed wind fields analyzed at ECMWF. Heimann and Keeling (1989) used parameters to express the effect of diffusion by cumulus activity and obtained an interhemispheric exchange time of 1.3 years.

Global transport of an artificial constituent has been investigated by Kida (1983a, 1983b) with a Lagrangian particle diffusion model driven by the wind generated by a hemispheric GCM, and by Yamazaki and Chiba (1992) with a semi-Lagrangian transport model driven by the whole globe GCM winds. With an artificial tracer, they were able to demonstrate the performance of the model efficiently, because they could single out transport characteristics from emission and washout. The semi-Lagrangian scheme used by Yamazaki and Chiba (1992) is a simple method for describing advection which requires positive definite transport and stability of the computation for a relatively large time step. A review is provided by Staniforth *et al.* (1991).

Despite wide awareness of slow exchange through the CGZ, the global structure of the zone has not been well characterized. The first aim of the present model is to visualize important aspects of atmospheric diffusion fields, especially the CGZ. The second purpose of the model is to evaluate the transport characteristics of a semi-Lagrangian scheme driven by the ECMWF winds, without any tuning for subgrid scale mixing. The need for a three-dimensional global transport model was demonstrated by Tans *et al.* (1989) when they failed to estimate accurately the magnitude of sources and sinks of carbon dioxide. Diffusion due to cumulus activity introduced in the previous model (Prather, *et al.*, 1987, Jacob, *et al.*, 1987 and Heimann and Keeling, 1989) was based on statistics from the GISS climate model. Since the statistics cannot reflect the annual variation of the circulation, for analysis of regional sources and sinks, the cumulus diffusion must be replaced by observations. Total mass conservation was not intended. The model is unsatisfactory for the estimation of sources and sinks of minor constituents.

This paper describes the model, the time evolution of the mixing ratio of an artificial constituent, and inter-hemispheric exchange through the CGZ.

## 2. Model description

### *2.1 Semi-lagrangian model*

An off-line type semi-Lagrangian model was developed with pressure coordinates for the vertical and longitude-latitude coordinates for the horizontal plane. The backward trajectory was obtained with wind data generated at 30 minute intervals by linear interpolation of 12-hour-interval data. The procedure for obtaining mixing ratios at grid points in the semi-Lagrangian model is comprised of a backward trajectory calculation and an interpolation of the mixing ratio at departure points. The grid point at which the mixing ratio at a certain time is considered is called the arrival point, and the point calculated by the backward trajectory is called the departure point.

Though several sophisticated designs of semi-Lagrangian transport have been proposed (Williamson and Rash 1989, *etc.*), all complex treatments were avoided to keep the model as simple as possible. The linear interpolation in space and time of observed winds was used as the carrier in the present model.

The data, the method of trajectory calculation, interpolation in space, the boundary conditions and the time interval for the backward trajectory are described in this section.

### *2.2 Data*

The wind data that drives the circulation is ECMWF's WCRP/TOGA basic level III data set. Data are given at 14 pressure levels (1000, 850, 700, 500, 400, 300, 250, 200, 150, 100, 70, 50, 30 and 10 hPa), with 2.5 × 2.5° horizontal resolution at 00UTC and 12UTC. These data are a product of ECMWF's four-dimensional data assimilation system, acquired before the application of normal-mode initialization. The one year period from January to December 1989 was used in this study. Quality of these data is reported by Trenberth (1992).

The data is archived at ECMWF from data produced in the forecast analysis cycle. The data at a grid point are interpolated horizontally from the very dense data field (T106 spectral truncation = 1.125 × 1.125°). The data are extrapolated or interpolated in the vertical direction from sigma coordinates to fit the vertical profile of the pressure scale data.

The wind data were not modified further for the following reasons.

(1) Data sampling maintained the profile of the fields in time and space although the delicate mass balance in the original data was lost.

(2) There is no way to recover the information related to smaller scale fluctuations.

(3) While the mass balance in the wind field may be equivalent to that of the Eulerian type model, it is not necessarily equivalent to the mass balance in a semi-Lagrangian model.

The quality of the data is influenced by changes in forecast and analysis methods. The vertical velocity included in the model was changed drastically by modifications in analysis methods during 1989 (Trenberth, 1992). The major changes occurred in May, August and November, 1989. The results of the present calculation must be considered with these changes in mind. The procedure for construction of this data set and quality of the data before 1989 are reported by Shaw *et al.* (1986), Trenberth and Olson (1988) and Hoskins *et al.* (1989).

### *2.3 Trajectory calculation*

The departure point $\vec{r}_{depart}$ at times $t$-12 hour, for an arrival point $\vec{r}_{arrival}$ at time $t$ was estimated by a backward trajectory. A backward trajectory consists of 24 short trajectories calculated sequentially along the trajectories from the wind at times $t$ and $t$-12 hour. The procedure follows:

(1) Obtain a set of three-dimensional wind data at each of two times, $t$ and $t$-12 hour, at the arrival point, $\vec{r}_{arrival}$. Interpolate to a time of $t$-15 minute, and obtain the wind; $\vec{v}\,(\vec{r},\ t\text{-}15$ minute).

(2) Move backward 30 minutes from $\vec{r}_{arrival}$ along $\vec{v}\,(\vec{r}_{arrival},\ t\text{-}15$ minute) and obtain point $\vec{r}_1$.

(3) Obtain the wind vectors at the eight grid points surrounding $\vec{r}_1$ at $t$ and estimate the wind vector at $\vec{r}_1$ by interpolation in space ($\vec{v}\,(\vec{r}_1,\ t)$). Obtain the wind $\vec{v}\,(\vec{r}_1,\ t\text{-}12$ hour) by the same procedure. Obtain the wind vector $\vec{v}\,(\vec{r}_1,\ t\text{-}45$ minute) by interpolation in time of the two winds, $\vec{v}\,(\vec{r}_1,\ t)$ and $\vec{v}\,(\vec{r}_1,\ t\text{-}12$ hour).

(4) Move back 30 minutes by $\vec{v}\,(\vec{r}_1,\ t\text{-}45$ minute) from $\vec{r}_1$, and obtain $\vec{r}_2$ at $t$-1 hour.

(5) Repeat steps (3) and (4) until the position at $t$-12 hour, $\vec{r}_{24}$, is obtained.

The rationale for choosing a 30 minute time interval will be discussed later.

### *2.4 Spatial interpolation*

The spatial interpolation used in this model is a simple one in longitude (x), latitude (y) and pressure (p) coordinates as shown in Fig. 1. The wind at a point $P\ (x,\ y,\ p)$ surrounded by eight grid points (a, b. . .h) is obtained by the following equation:

$$\vec{V} = \sum_{i=1}^{8} \vec{V}_i W_i \qquad (1)$$

where $W_i$ is the weight of each of the three wind components at the grid point. The weight is calculated by the volume of a box defined by $P$. The point $P$ defines the volumes of eight weighting boxes inside the eight grid points. The weight of a grid point is determined by the volume of the weighting box in the diagonally opposite corner.

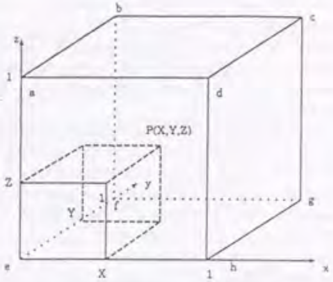

Fig. 1. A schematic view of the linear interpolation in three-dimensional space. Grid points are located at eight corners of the cube denoted by a, b, c, d, e, f, g and h. The size of the cube is one. Three-dimensional wind and the mixing ratio at the point $P\ (X,\ Y,\ Z)$ are obtained by summing each value at the points multiplied by the weights. The weight is calculated from the volume of the box defined by the interpolation point and the opposite corner of the cube. For example, the volume of the small box inside the cube is the weight for the value at grid point c.

Sub-grid scale mixing is not explicitly defined in this model but is implicitly calculated when the mixing ratio at a departure point is interpolated from the grid point values surrounding it.

### *2.5 Boundary conditions*

This model assumes that the top and bottom pressure levels are boundaries for the atmosphere. The bottom boundary is the 1000 hPa pressure level and does not recognize topography, although the wind is analyzed according to topographic conditions. If the departure point is obtained at a pressure greater than that of the bottom boundary, the value at 1000 hPa is used instead. If the departure point is obtained above the upper pressure boundary, the value at 10 hPa is used.

The model may create an artificial source or sink of the tracer with this boundary condition. This effect will be taken into account in the calculation of the exchange time.

### *2.6 Time interval for the backward trajectory*

Wind data should be frequent enough so that the length of air mass advection for one step is less than the distance between grid points. This requirement is not based on the stability of the computation but on the simple relation between spatial variation of the wind and the length of advection of one time step. Advection beyond the next grid point will not follow the wind field if the wind field changes in the distance between grid points (unless the spatial variation of the wind is not considered in the departure point calculation).

A wind of 100 m/sec transports air mass at 360 km/hour; the grid distance at 45° is about 180 km. In this situation, typical at the core of the jet stream, the time required to traverse one grid interval is 30 minutes. Thus, a 30-minute time step was chosen for interpolation of the winds. With this time scale, the trajectory calculation takes advantage of the information of the spatial change in the winds. It is not clear how much error is introduced by the backward trajectory calculations.

One test to evaluate the error generated by the wind sampling interval is to investigate the difference in the departure points calculated using 30-minute intervals and using a 12-hour interval. Because the observed wind data for 30-minute intervals are not available, alternative data are prepared from the output of a GCM. The winds derived from the National Center for Atmospheric Research's community climate model version one (CCM1: Williamson *et al.*, 1987) were used to test the departure points. This model performs the integrations of the primitive equations with a spectral method using R15 and 12 vertical sigma levels, and with a semi-implicit time integration method. The grid point system converted from spectral space in CCM1 has a resolution of 7.5° long by 4.5° lat. Departure points were first calculated using wind data from CCM1 at 30-minute intervals. Departure points were next calculated from twelve-hour interval CCM1 data, using the sequential interpolation to 30-minute data previously described. A maximum difference between the two results of about 6° was found in the upper troposphere of the Middle Latitudes. A smaller difference of about 2° to 4° appeared at the Middle Latitudes through the troposphere. In the Equatorial Latitudes the difference was less than 2°. Although the model may introduce artificial mixing in the Middle Latitudes, the model can be expected to perform well for 12-hour interval winds in the Equatorial Latitudes.

## 3. Time integration

### *3.1 Initial distribution*

The time evolution of the distribution of an artificial tracer was investigated. The tracer was introduced in a small enough concentration to ignore contributions to the total mass. The concentration distribution at grid points over the globe is defined (in arbitrary units) by

$$C(x, y, p) = (90 - y)/180 \tag{2}$$

where $x$ is longitude, $y$ is latitude (negative values in the Southern Hemisphere) and $p$ is pressure. There is no variation in concentration with $x$ or $p$. The sensitivity to the initial condition will be addressed later in this paper. The tracer has no buoyancy and no sources or sinks.

### *3.2 Time evolution in the first month*

The time integration was carried out for one year beginning at 00UTC January 1, 1989. Horizontal distributions of the constituent at 850 hPa in the first month are shown in Fig. 2. For the sake of clarity, only five contours (0.4 to 0.6) are drawn.

At the initial condition (a) contour lines are straight and parallel to the equator. Five days later (b), contour lines have already twisted because of transport and mixing in the tropical region. Contour lines are compressed from the Indian Ocean to Northern Australia.

Ten days later (c), air in the tropics has moved southward near the international date line, and over the Amazon basin where it has formed a tongue-shaped distribution. Fifteen days later (d), contour lines almost overlap each other over southern Africa and equatorial Asia and form a CGZ. It must be stressed that the motion of the contours is not caused by transport alone. The mixing ratio on either side of the CGZ is also dependent upon diffusion in its respective hemisphere. The CGZ forms a barrier between the hemispheres, across which mixing is inhibited.

### *3.3 Seasonal change in the lower troposphere*

Figure 3 shows the monthly mean horizontal distribution of mixing ratio at 850 hPa for February (a), April (b), June (c), August (d), October (e) and December (f). The contour interval for these months has been varied from 0.05 (a) to 0.01 (f) in order to show more clearly the distribution of the tracer in the steep gradient region.

In February (a), though the initial distribution still remains, the steep gradient region has extended from the Indian ocean to the South Pacific ocean where the South Pacific Convergence Zone (SPCZ) is observed. From the center of the Pacific to the Atlantic the steep gradient zone is located along the equator. A kink in the zone is observed along the west coast of South America. The features remain until May.

In May, the steep gradient zone shifts north over the Indian ocean and South America. In July, the entire Indian and Indo-China peninsulae are covered by Southern Hemispheric air. It may be important to note that the barrier which separates the Hemispheres is composed not only of the Inter-Tropical Convergence Zone (ITCZ) but also the monsoon area. The CGZ remains until September over Africa (10°, 10°N), the Middle East (90°E, 30°N) and the international dateline (180°, 10°N). The CGZ returns to its previous position near the equator in December (f). In December the CGZ is not as evident over the Pacific as in other months. Out-going long wave radiation data provided from ECMWF as the ECMWF/TOGA Supplementary Fields Data Set indicates that the ITCZ over the Western Pacific was not active at this month.

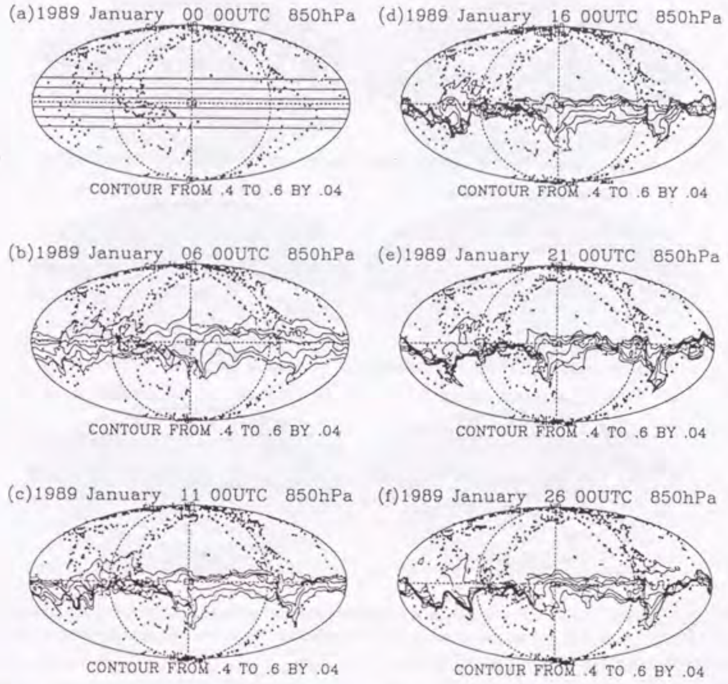

Fig. 2. Time evolution of the steep gradient zone at 850 hPa in January. Contour interval is 0.04. Note that a compositional gradient zone was formed in about one half month.

As indicated in the introduction, the CGZ is created by the combination of the transport and mixing. The trajectories of separate air masses which originate in distant regions can create CGZ if they pass adjacent to each other. A trajectory analysis (not shown) indicates that the air masses converge at the CGZ and are forced upward. It must be stressed repeatedly, that air mass on either side of the CGZ is mixed quite rapidly. Thus, the results of this experiment suggest that sources and sinks of atmospheric constituents along the Indo-China peninsula may affect air quality in the Southern Hemisphere during northern summer while such sources and sinks in the Amazon Basin may affect air quality in the Northern Hemisphere during northern winter.

### *3.4 Seasonal change in the upper troposphere*

Horizontal distributions of monthly-average mixing ratio at 300 hPa are shown in Fig. 4 for the same months as Fig. 3. A comparison of the two figures shows that, although the CGZ can still be recognized in the tropical region at 300 hPa, for each month the horizontal gradient is smaller at 300 hPa than 850 hPa. In the Northern Middle Latitudes, a CGZ is formed near the core of the jet stream.

### *3.5 Local effect of the barrier*

Daily variations and seasonal migration of the CGZ are indicated in Figs. 2 and 3, respectively. Both of these effects are crucial in determining the atmospheric composition of local environments near the CGZ.

As indicated in Fig. 2, the CGZ varies daily, especially in the tongue-shaped features of the CGZ. The CGZ sometimes closes upon itself, allowing a

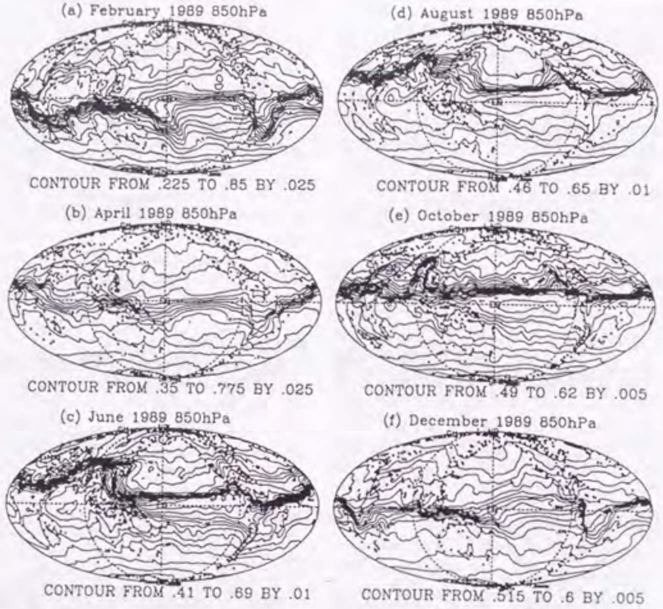

Fig. 3. Horizontal distribution of an artificial constituent for selected months at 850 hPa; (a) February, (b) April, (c) June, (d) August, (e) October and (f) December. Note that the contour interval varies in each frame and is indicated in each frame.

teardrop shaped body of air from one Hemisphere to move into the other. These masses of air may change the atmospheric composition in the downstream area from one Hemispheric air type to the other. Daily variations in $CO_2$ concentration at American Samoa, for example, may be explained by such a phenomena (Halter *et al.*, 1988).

The seasonal variation of the CGZ may influence the local level of atmospheric chemical activity over India and the Indo-China Peninsula. Over that area, Southern Hemispheric air is supplied continuously during the northern summer. The lifetime of atmospheric methane depends on the hydroxyl radical concentration, which is different in the Northern and Southern Hemispheres (Taylor *et al.*, 1991). The implication here is that the seasonal variation of the CGZ may create a difference in the lifetime of methane emitted from India in the northern summer and that emitted from the Amazon Basin in the southern summer.

## 4. Exchange between the northern and southern hemispheres

### *4.1 Seasonal change in the zonal mean mixing ratio*

The latitudinal profiles of zonally- and monthly-averaged mixing ratios, integrated over pressure levels from 1000 to 100 hPa are shown in Fig. 5. The ordinate scale corresponds to the sine of the latitude to express the relative weight at a given latitude.

North of 30°N and south of 30°S, the mixing ratio changes monotonically with time toward a final equilibrium value. In the tropics, however, the tracer concentration undergoes a seasonal cycle of increasing concentration from January through August, and decreasing concentration from September through December.

The coordinates of triangles plotted on monthly lines correspond to the global-average mixing ratio and the latitude at which the mixing ratio coincides with the global-average.

The total mass of the tracer increased from January through April. The final global-average mixing ratio was 0.56. There are several possible causes of the tracer mass conservation error.

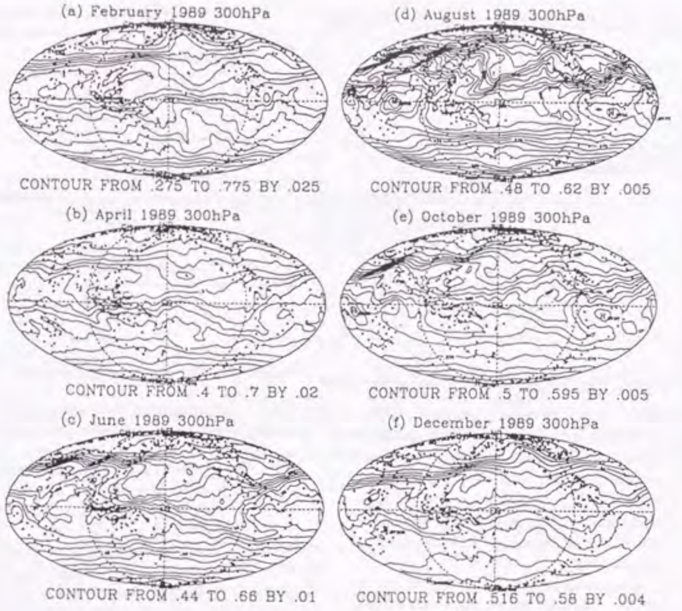

Fig. 4. Same as Fig. 3 but for 300 hPa.

1. The accumulation of truncation error generated by the precision of IEEE 32 bit floating point data must be considered. The mass conservation error is on the order of that which would be caused by a 10 % skew in the randomness of the sign of the error, an unlikely occurrence at best.

2. If we observe the continuous growth of error through the first four months of the integration, there is reason to question the use of such a simple boundary condition. It is obvious that the current boundary condition must be modified to include the emission or deposition of mass if the model is to be used to simulate real gases. Further modification of the model has been delayed pending implementation of a more sophisticated boundary condition.

3. The vertical pressure coordinate system may also present a problem. In the pressure coordinate system the region below the topographic surface is not treated properly. Sigma coordinates are required for proper expression of the boundary conditions. Modifications to correct this situation also await future study.

Because major modifications to the model would be required in order to close accurately the mass balance, another strategy was implemented. Such a strategy permits the investigation of inter-hemispheric mass exchange phenomena without the necessity of mass conservation.

### *4.2 Two box model*

The inter-hemispheric exchange rate is defined as the fraction of the atmospheric mass transferred from one Hemisphere to the other as shown in Fig. 6. Suppose the mixing ratio of the Southern Hemisphere is $A$ and that of the Northern Hemisphere is $B$ at a time $T - \delta T$ and that the respective weight fractions of the total are $p$ and $1 - p$. A volume of air of mass $x$ is transferred from the Southern to the Northern Hemisphere, and a different mass, $y$ moves, from the Northern to the Southern Hemisphere. The fraction of the total atmospheric mass in the Southern Hemisphere, $q$ at time $T$ may be written

$$q = p - x + y. \tag{3}$$

The mixing ratios $C$ and $D$ at time $T$ in either Hemisphere satisfy the following relations:

$$Cq = Ap - Ax + By + r \tag{4}$$

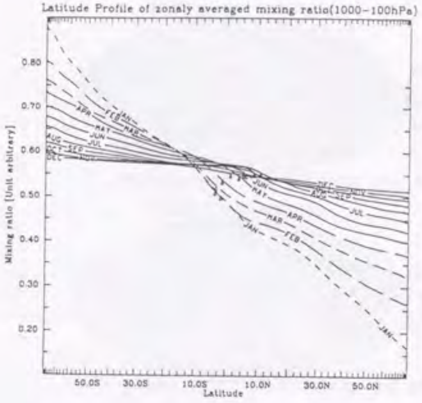

Fig. 5. Latitude profiles of the zonally-averaged concentration of an artificial trace integrated over the troposphere; from 1000 hPa to 100 hPa. The ordinate is the mixing ratio and the abscissa is the sine of the latitude. The month is labeled on each line.

for the Southern Hemisphere, and

$$D(1-q) = B(1-p) + Ax - By + s \tag{5}$$

for the Northern Hemisphere, where $r$ and $s$ are small residual terms. We may get the best estimate of $x$ and $y$ by minimizing the residuals $r^2 + s^2$. If we substitute for $y$ from Eq. (3) in Eqs. (4) and (5) this condition can be written as

$$\frac{d(r^2+s^2)}{dx} = 0 \tag{6}$$

then we have,

$$x = \frac{(A-B)p + (2B-D-C)q + D - B}{2(A-B)} \tag{7}$$

$$y = q - p + x. \tag{8}$$

Turn around time or inter-hemispheric exchange time is defined as

$$T_{south} = \frac{p}{x} \tag{9}$$

for the Southern Hemisphere and

$$T_{north} = \frac{1-p}{y} \tag{10}$$

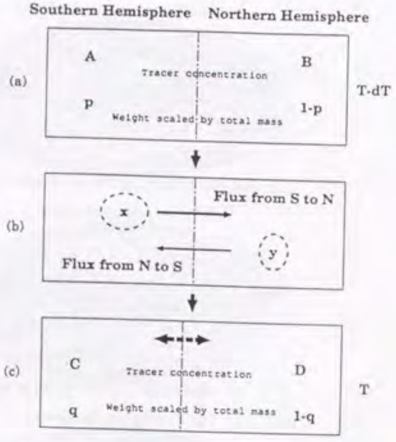

Fig. 6. Two-box model with moving barrier. A globe is separated into two boxes with the fraction $p$ and $1-p$ for time $T-dT$ and $q$ and $1-q$ for time $T$. The mixing ratio of the boxes is A, B, C and D, respectively. The exchanged mass is expressed by $x$ and $y$ depending on the direction of the movement. Note that $x$ is not equal to $y$ because the boundary of the box was taken into account in this system. In this paper, $dT$ is one month.

for the Northern Hemispheric air. These expressions are equivalent to the resistance time seen in Jacob *et al.* (1987) and Heimann and Keeling (1989).

The boundary was defined as the latitude for the zonal vertically (1000–100 hPa) and monthly-averaged tropospheric mixing ratio, which is given by the coordinates of the triangles in Fig. 5.

*4.3 Two initial conditions*

The boundary of the Hemispheric air masses and exchanged mass are shown in Fig. 7a. The latitude of the boundary moves from 4°S in February to 11°N in August and September. On the average, the boundary is located in the Northern Hemisphere (6.4°N) resulting in the unequal partitioning of air mass between the Hemispheres.

Exchanged mass as a fraction of the total changes with the seasons. The maximum exchange from south to north (Eq. 7) occurred during December, while that from north to south (Eq. 8) occurred in April. The reason for this seasonal difference in maximum exchange rate for each Hemisphere is that the mass exchanged contributes both to the movement of the boundary position and to the change in

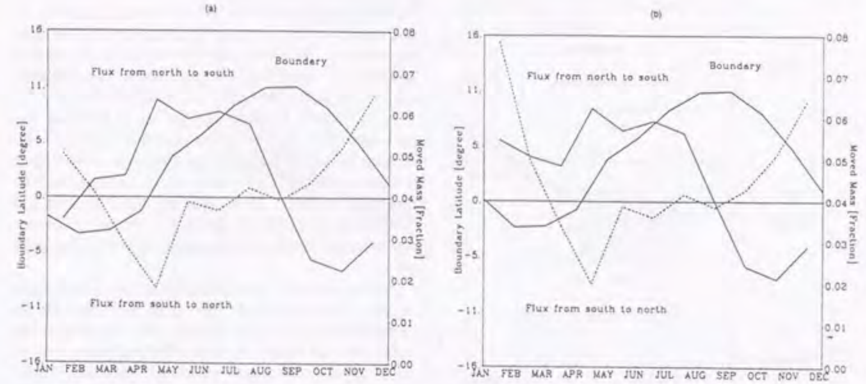

Fig. 7. The position of the boundary and the flux from north to south and *vice-versa*. (a) for a linear initial distribution with zero at the Arctic Pole and one at the Antarctic Pole. (b) for a step function case such with zero in the Northern Hemisphere and one in the Southern Hemisphere. The flux is scaled by total atmospheric mass.

hemispheric mixing ratios as a function of time as shown in Figs. 7a and 5, respectively. The exchange time may be calculated by Eqs. (9) and (10). A value of 0.04 for exchanged mass corresponds to a value of slightly more than one year for an inter-hemispheric exchange time if the difference in atmospheric mass between the Hemispheres is ignored. The overall average of the monthly exchange times is 1.27 for the Southern Hemisphere (Eq. 9) and 0.95 years for the Northern Hemisphere (Eq. 10).

The exchange time in this model is quite similar to the values in previous calculations, even though the present model does not include the effects of cumulus convection or sub-grid scale mixing. In the case of GCM winds (Prather *et al.*, 1987) or observed wind data (Heimann and Keeling, 1989), the model required mixing by cumulus convection to get the proper inter-hemispheric exchange time. The effect of convection can be summarized: dry convection near the surface mixes materials released from surface of the earth in the planetary boundary layer. Moist convection transports materials near the surface vertically in the mesoscale convective complex, especially in the tropics. The proper exchange rate in the present model may be due to the 14 vertical levels of wind data which resolve the inter-hemispheric flow in the upper troposphere quite well, and to the representation of mass flux by mesoscale convection complexes by the ECMWF winds.

To test the robustness of the analysis, another simulation, with a different initial condition may be compared. A tracer concentration step function with respect to latitude is used;

$$C(x,y,p) = \begin{cases} 1 & \text{if } y > 0 \\ 0 & \text{if } y \le 0 \end{cases} \tag{11}$$

where $x$ is longitude, $y$ latitude and $p$ pressure. The results are displayed in Fig. 7b.

The position of the boundary is nearly the same as in the linear case (a) after April. The fraction of mass exchanged in months after April is also nearly the same as the linear case (a). The global average mixing ratio is 0.39 in December. If this result is compared with the value of 0.56 obtained in the linear case (Fig. 5) it indicates that the model tends to weight the information of the Southern Hemisphere more heavily than that of the Northern Hemisphere. These results indicate that the exchange ratio and exchange time are almost independent of the initial condition.

*4.4 Mixing by a moving boundary*

Let us consider the effect of movement of the boundary on exchange through the boundary. A simple wall model is used to make an estimation of the effect of the movement of the boundary. Figure 8 shows the notation for two boxes separated by a moving wall. The wall entrains some air mass in the direction of motion as it moves. Diffusion inside the box is assumed to be fast enough to ignore the spatial distribution of the tracer. Consider a step function distribution of concentration of a tracer along a line from the South Pole to the North Pole. The step occurs at some point $s$ between the poles, with a value of one (in arbitrary units) on the southern side of $s$ and zero on the northern side. This initial distribution occurs in February. The boundary moves from the southern limit, $s$ in February to a

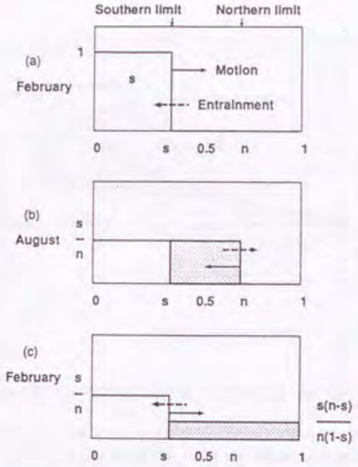

Fig. 8. A simple model of mixing by a half-transparent wall. Assume the whole globe is separated by a wall which moves between s and n during a seasonal cycle shown in Fig. 2 or Fig. 7a. The material of the northern side is moved to the southern side by the motion of a wall which entrains the air mass of the other side of the wall as it moves.

northern limit, $n$ in August. The total amount of the constituent is $s$. When the boundary moves from $s$ to $n$, the mixing ratio changes from one to $s/n$ on the southern side, but remains zero in the northern side because the barrier entrains air from the northern side as it moves north. When the boundary returns from $n$ to $s$, the boundary entrains air from the southern side. Thus the mixing ratio on the northern side is $s(n-s)/n/(1-s)$ in February. The mass exchanged in one year $x$ is

$$x = \frac{(n-s)s}{n}. \tag{12}$$

If $n = 0.62$ and $s = 0.49$ (based on data from Fig. 7a), then $x = 0.1$ and the exchange time is $0.5/x = 5$ years. The entrainment of the air at the barrier seems to have a significant effect on the exchange time, but is not rapid enough to account for the actual exchange between sides.

### *4.5 Effect of vertical velocity*

To investigate the effect of vertical mass flux, a diffusion experiment was conducted without vertical flux, and compared with the actual model results. The profiles of the zonal- and monthly-averaged mixing ratios are displayed in Fig. 9. The profiles for two pressure levels, 300 hPa and 850 hPa, are presented for the vertical-flux and the no-vertical-flux cases. The initial distribution in both cases is identical. The mixing ratio profiles for the two pressure levels show very different characteristics.

In the lower troposphere (a, c), a striking feature appeared in the no-vertical-flux case (c). No mixing between hemispheres occurred, resulting in a different equilibrium value of the mixing ratio for each hemisphere. These profiles resemble Fig. 2 of Prather *et al.* (1987) in which two mixing ratio versus latitude profiles of an artificial tracer are compared.

In the upper troposphere, the tracer mixed faster in the no-vertical-flux case (Fig. 9d) than in the vertical-flux case (Fig. 9b). In the no-vertical-flux case, the air mass in both Hemispheres was almost totally exchanged within six months. In the vertical-flux case, information in the lower troposphere seems to play an important role in maintaining the upper troposphere composition gradient.

This comparison demonstrates the two roles of vertical motion: to relax the inter-hemispheric contrast in the lower troposphere and to maintain the inter-hemispheric gradient in the upper troposphere. In other words, the inter-hemispheric exchange occurs mainly in the upper troposphere due to a combination of the CGZ and vertical motion, as suggested by Prather *et al.* (1987) and Yamazaki and Chiba (1992).

## 5. Conclusions

A simple semi-Lagrangian tracer transport model was developed and the time evolution of the mixing ratio of an artificial constituent was analyzed. The results obtained in this study can be summarized as follows:

(1) A steep compositional gradient zone is formed in the lower troposphere in the low latitudes. There is a barrier to the exchange of the tracer across the zone. A seasonal variation of the CGZ occurs. In the central Pacific, the barrier is located near the ITCZ for most of the year. It shifts to 30°N during the northern summer over Southern Asia. It also shifts to 30°S during the northern winter over the Amazon Basin.

(2) Daily fluctuations of the position of the boundary are observed. A teardrop-shaped intrusion of one Hemispheric air into the other is frequently observed in the lower troposphere. Although this inter-hemispheric exchange contributes little to total inter-hemispheric mass exchange, it may have a significant effect on the local atmospheric composition.

(3) The average position of the barrier is located in the Northern Hemisphere (= 6.4°N) resulting in a different mass and volume for either hemisphere.

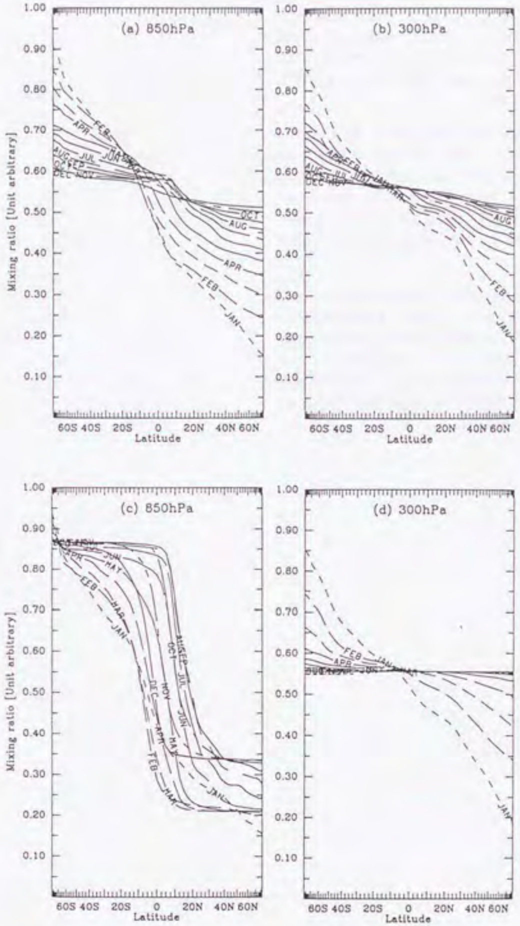

Fig. 9. same as Fig. 2, but for two selected pressure levels for cases with and without vertical motion: With vertical motion, (a) for 850 hPa, (b) for 300 hPa and without vertical motion, (c) for 850 hPa and (d) for 300 hPa.

(4) The seasonal cycle of the monthly inter-hemispheric mass exchange was different for either hemisphere, due to the movement of the boundary. The flux from the Northern Hemisphere to the Southern Hemisphere showed a maximum in May and a minimum in October. Flux from the Southern Hemisphere to the Northern Hemisphere showed a maximum in December and a minimum in May.

(5) A one-dimensional model with a moving boundary and atmospheric entrainment at the boundary was used to study exchange time. Based on the observed position of the CGZ, an inter-

hemispheric exchange time 5 years was estimated. The discrepancy between actual exchange time and that estimated from this simple model indicates the importance of other mixing mechanisms.

(6) The inter-hemispheric composition gradient is observed in the upper troposphere. A diffusion simulation without vertical mass flux indicates rapid mixing of the air mass in the upper troposphere. This result indicates that the gradient is maintained by vertical flux in the troposphere.

The implication of observed seasonal variation of the CGZ is that sources and sinks of constituents along the Indo-China peninsula may affect air quality in the Southern Hemisphere during the northern summer while such sources and sinks in the Amazon Basin may affect the Northern Hemisphere during the northern winter.

# Chapter 3 : Interhemispheric Exchange in the Troposphere by a Lagrangian Transport Model

## Abstract

The trajectories of passive tracers in the global atmosphere were statistically analyzed with emphasis on the exchange paths crossing the boundary between the Northern and Southern Hemispheres. Twice-daily three-dimensional wind data for January and July 1989 from the European Centre for Medium-Range Weather Forecasts were used for the trajectory calculation.

The statistics of the latitudes of tracers indicated that the partial barrier between the Northern and the Southern Hemispheric air masses was at 15°S and 5°S in January and at 10°N and 30°N in July. Tracers moving from the northern side of the boundary to the southern side and those moving in the opposite direction were selected with a criterion for the trajectory. The trajectories were classified into three types: one passing through only the lower part of the troposphere; one passing through only the upper part of the troposphere; and one going into the tropics from the lower troposphere, lifted to the upper troposphere in the ITCZ, and entering the other hemisphere. The trajectory from the summer to the winter hemisphere consists of an upper-only path and a lifted path, whereas the trajectory from the winter to the summer hemisphere consists of a upper-only path and a lower-only path.

Although individual trajectories were sensitive to the methods of computation, a set of trajectories was insensitive to them. The regional characteristics of the trajectories were discussed by making a comparison among the three trajectories obtained from instantaneous wind fields, and from twice-daily, and monthly-averaged wind fields.

## 1. Introduction

The tropospheric air mass in the Northern and Southern Hemispheres is exchanged through the tropics. In the tropics, atmospheric motion is characterized by vertical drift from isentropic surfaces due to diabatic heating and cooling induced by condensation or evaporation of water vapor and by interaction with cloud droplets which have effective infrared radiation to space. These diabatic processes make isentropic analysis useless and make trajectories of air motion impenetrable. Until recently, these complexities have restricted our understanding of the tropical atmospheric motion in the model atmosphere. Recent development of assimilated winds (Bengtsson *et al.*, 1982) might allow us to overcome the above-mentioned complexities. The aim of this paper is to resolve the atmospheric motion in the tropics associated with inter-hemispheric airmass exchange, which is crucial for global tracer simulation in the troposphere.

Tracer simulation relies on the atmospheric motion that can be classified into transport and diffusion based on the time and spatial scales of the observations. Atmospheric flow relevant to transport in the assimilated wind data in the tropics consists of at least three classes over a finite time interval, say one month. One is flow that is closed in the tropics, for example a vertical eddy such as the Hadley circulation or a horizontal eddy such as a tropical cyclone. The second is the flow connected to the middle latitudes of either the Northern or the Southern Hemisphere. The third is some kind of flow connecting each hemisphere. We will call the third class the conveyor belt and focus our attention on this class.

Atmospheric flow relevant to diffusion in the assimilated wind data, sometimes called sub-grid scale mixing, is composed of mesoscale eddies, advection in the cumulus convection, turbulence in the planetary boundary layer, *etc.* While the sub-grid scale mixing has a major role in the mixing of the sub-grid scale structure (the formation of the sub-grid structure was demonstrated by Pierrehumbert and Yang, 1993), these processes are outside the scope of the present study because there is no simple way to deal with sub-grid scale diffusion using the assimilated wind data.

The importance of inter-hemispheric exchange processes in the upper part of the troposphere was reported by Newell *et al.* (1969). They estimated the inter-hemispheric exchange using meteorological data and trace material observations, and discussed the relative role of mean motion and eddy motion in the inter-hemispheric exchange. They suggested the importance of eddy motion near 150–200 hPa based on the standard deviation of the meridional current. Prather *et al.* (1987) showed that the inter-hemispheric transport of CFC's occurred between 150–200 hPa in their global three-dimensional transport model. Yamazaki (1992), and Yamazaki and Chiba (1993) also demonstrated the upper tropospheric path in a three-dimensional model, although they did not consider the horizontal distribution of the path.

The position of the barrier which divides mid-latitude air and tropical air was discussed by Pierrehumbert and Yang (1993). They found a barrier between the middle latitudes and the tropics on the 315 K surface, and a pipeline which connects the middle latitudes and the tropics. The boundary which divides the two hemispheric air masses was discussed by Taguchi (1993). He showed that the boundary can be obtained in a three-dimensional simulation of an artificial material and moves north and south with season. A tracer simulation with an artificial material, however, cannot show the location and strength of mixing because the air mass entering the other hemisphere loses its identity soon after the invasion owing to the mixing there. Trajectory analysis is an alternative way to investigate interhemispheric mixing (Kida 1983a, b, Noda 1988, and Yamazaki 1992) although previous studies did not consider the horizontal position or seasonal migration of the boundary.

The trajectory obtained from the time-dependent three-dimensional wind field is sensitive to the computational procedure and even to the computer architecture due to the representation of floating-point numbers. That sensitivity reduces the reliability of a path. One way to increase reliability might be to use monthly-mean wind fields for the trajectory calculation. In fact, some transport models are designed to use long-term averages of the wind, such as a monthly or bi-monthly average (Zimmermann *et al.*, 1989, Taylor *et al.*, 1991, *etc.*). They are taking into account the effect of fluctuations of the wind direction and strength by using the standard deviation of the wind as well. If we use monthly-mean wind fields without considering the standard deviation, we will lose the time variation in the atmospheric motion which might have a crucial role in the inter-hemispheric exchange. Another way to increase reliability is to use statistical analysis from long-term atmospheric trajectories. We will use the latter method in this paper, because including the standard deviation of the wind in the trajectory analysis confuses the interpretation of the results; once the transport and diffusion are combined they cannot be separated again. Only a small number of cross-tropical trajectories are selected from the widespread trajectories over the entire atmosphere. Without using this selection, the conveyor belt cannot be determined from the figures.

Even if we use time-dependent three-dimensional wind fields, we cannot avoid the effects of the turbulent nature inherent in the grid-scale flow. The turbulent nature of the grid-scale current includes both the time variation and spatial structure of the wind. To investigate the effects of the turbulent nature, the trajectories are calculated by three methods. The first uses the time-dependent wind field (Section 4), the second uses the frozen or fixed wind field (Section 5), and the third uses the monthly-mean wind field (Section 6). Most of the following discussions are confined to the time-dependent wind mode; the other two modes are treated to illustrate how the trajectories are distorted from reality.

## 2. Analysis methods and data source

### *2.1 Meteorological data*

The trajectory used in this study was calculated from the assimilated data from the European Centre for Medium-Range Weather Forecasts (ECMWF). ECMWF's TOGA basic level-III data set was used. The data are given with 2.5° horizontal spacing and at 14 vertical-pressure levels: 1000, 850, 700, 500, 400, 300, 250, 200, 150, 100, 70, 50, 30, and 10 hPa. Three-dimensional winds and surface pressure were used in the calculation of the trajectory. Temperature and humidity fields were used to assess the reliability of the trajectory. Trajectories were calculated for January and July 1989.

ECMWF has been using the T106 resolution atmospheric model since 1985. The data for the 2.5° resolution were interpolated from this fine-resolution data at ECMWF. The advantage of this data set compared to previous ones (WMO archive) is that it has a larger number of vertical levels and it does not suffer from normal-mode initialization. As a result of excluding the normal-mode initialization, the vertical velocity sometimes exceeds 1000 hPa/day in the middle troposphere in the tropics. This rapid vertical motion was retained in the conversion process in which omega was sampled (not averaged) to the low-resolution grid (2.5°) from the high-resolution analysis (T106). In the high-resolution model, some of the mesoscale features in the tropics are possibly realized to some degree, which may affect the current data through the assimilation procedure. The disadvantage of this data set is that the three-dimensional wind has lost its mass balance in the Eulerian coordinate system. The trajectory analysis is, however, rather insensitive to this deficiency.

ECMWF is continuously changing the forecast models in resolution and the physical processes. Since the data are the product of the four-dimensional assimilation system, the quality of the data pertains to changes in the forecast models. The data used in this paper do not experience a major change during each month, while a mass flux form of the cumulus parameterization scheme was introduced in May and it affected the quality of the data (Trenberth, 1992). One has to consider this fact if one wishes to discuss the difference in the results between January and July.

### *2.2 Trajectory calculation*

A total of 143,136 passive particles were released from every grid point except the poles and they were traced for 30 days. The three-dimensional position of the particles was recorded and analyzed later.

Vertical spacing is not uniform in terms of number per air mass, which emphasizes the upper part of the atmosphere. It was intended to investigate the upper part of the transport more closely since the importance of the upper part of the troposphere was suggested in previous studies (Newell *et al.*, 1969, Prather *et al.*, 1987, Yamazaki 1992, *etc.*). This bias hinders us from evaluating the relative importance in the vertical direction in this model. Number density per area in the meridional direction is also uneven and the air masses in the polar region are more emphasized than those in the tropics, so care is required for the interpretation of latitude dependency of the trajectories.

The method for tracing the trajectory is the same as that of Taguchi (1993), except that the direction of time is reversed. The intention of this algorithm is to use the spatial distribution of the three-dimensional wind field as precisely as possible. The time interval is 30 minutes.

The arrival point $\vec{r}_{t+12\ \mathrm{hour}}$ for a departure point $\vec{r}_t$ is estimated by a set of forward trajectories. The estimate consists of 24 short trajectories calculated sequentially along the trajectories from the wind at times $t$ and $t+12$ hour. The procedure is as follows:

(1) Obtain the wind vectors at the eight grid points surrounding $\vec{r}_t$ from the wind data at $t$.

(2) Estimate the wind vector at $\vec{r}_t$ ($\vec{v}(\vec{r}_t,\ t)$) by linear interpolation in space.

(3) Obtain the wind vectors at the eight grid points surrounding $\vec{r}_t$ from the wind data at $t+12$ hours

(4) Estimate the wind vector at $\vec{r}_t$ ($\vec{v}(\vec{r}_t, t+12$ hours)) by interpolation in space.

(5) Estimate the wind vector $\vec{v}(\vec{r}_t, t+15$ minute) by linear interpolation in time of the two winds, $\vec{v}(\vec{r}_t,\ t)$ and $\vec{v}(\vec{r}_t, t+12$ hour).

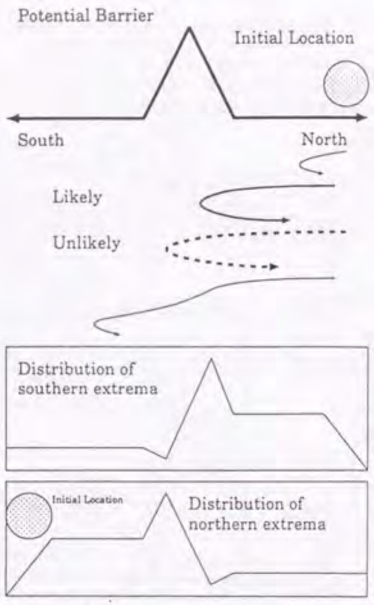

Fig. 1. Schematic diagram of the frequency distribution of extrema latitudes when there is a barrier for atmospheric motion in one-dimensional form.

(6) Move forward 30 minutes by $\vec{v}(\vec{r}_t, t+15$ minute) from $\vec{r}_t$, and obtain $\vec{r}_{t+30\ \mathrm{minute}}$.

(7) Repeat steps (1) to (6) until the position $\vec{r}_{t+12\ \mathrm{hours}}$ is obtained.

The wind is interpolated in the pressure-coordinate system, while the horizontal motion is calculated in the Cartesian coordinate system fixed to the earth. If a trajectory descends below the surface pressure, the particle is lifted to that level. Particles initially under the ground are traced above the ground from the second time step. If a particle ascends over 1 hPa, it is set to 1 hPa.

Trajectories are calculated on CRAY/XMP/UNICOS, IBM/R6000/AIX, and SUN/Sparc/Solaris. Calculated trajectories are different from machine, to machine probably due to difference in precision in floating point number. When the time interval to calculate trajectory was reduced to 15 minutes, calculated trajectories were also changed. Different trajectories were selected when the criteria which will appear later in this paper were applied to the trajectories calculated on the different machines

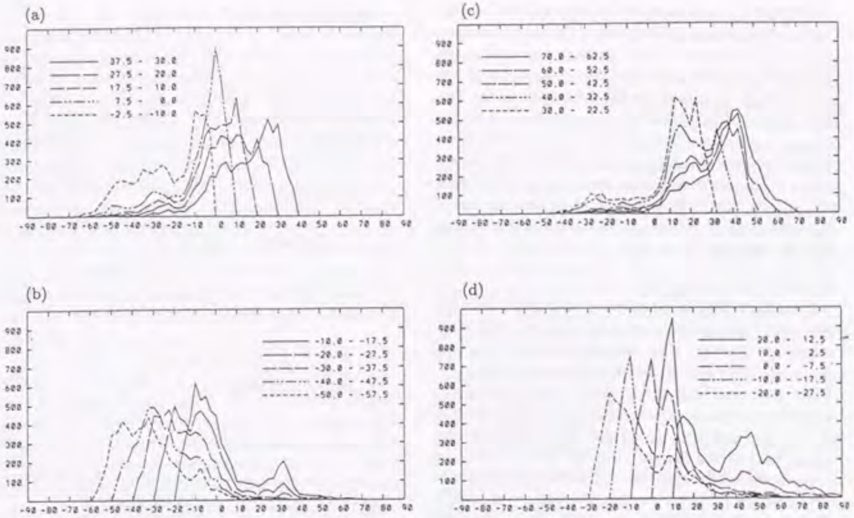

Fig. 2. Parcel frequency of extreme latitudes achieved during 30-day tracing in January (a) for the southern extreme and (b) for the northern extreme and in July (c) for the southern extreme and (d) for the northern extreme released from five latitudinal bands indicated in the figures.

and with different time intervals. The spatial patterns, however, for the selected trajectories were almost the same. The results displayed in this paper were obtained on the IBM.

## 3. Statistics characterizing mixing

### *3.1 Partial barrier*

A particle would travel over all latitudes if it is traced over a long time. But if the tracing time is limited to one month, the particle travels over a relatively narrow latitude band because it tends to stay in an eddy or in the original hemisphere. In fact, most of the particles remained in the original hemisphere and only a small number migrated into the other hemisphere.

For the first step, the extrema of the latitudes of trajectories obtained during 30 days were investigated to show the partial barrier between Northern and Southern Hemispheric air masses. This barrier can be considered as a field boundary, not a material boundary, because air masses are transported through this barrier. The northern and southern extrema latitudes were defined only once for each direction and for each trajectory. If there is a boundary for the mixing of air masses in a fluid, one may see a high density region in the frequency distribution of extrema, as illustrated in Fig 1. This diagram explains the situation in one dimension, where energy or inertia is required for a tracer to penetrate a region that contains a mountain (top figure). If a cluster of tracers is released from the right side of this mountain, most of the tracers are forced to remain on the right side of the mountain so that a high frequency of southern extrema latitudes is expected there. A small amount of tracer turns to the north at the left side of the mountain, because the turning at that position requires high energy, so a gap in the frequency distribution is expected there. If the tracers are released from the left side, a peak at the left side and a gap at the right side are expected, as indicated at the bottom of the figure.

Figure 2a shows the frequency distribution of southern extrema latitudes of a trajectory initially located between 1000 and 100 hPa in the vertical and the following five latitude bands: 37.5–30°N, 27.5–20°N, 17.5–10°N, 7.5°N-EQ, and 2.5–10°S. The frequency rapidly reduces from north to south around 5°S and increases again south of 20°S for all groups. The implication of this figure is that the partial barrier is located somewhere between the Equator and 10°S.

Figure 2b shows the frequency distribution of the northern extrema latitudes of a trajectory initially located between 1000 and 100 hPa at the following five latitude bands: 10–17.5°S, 20–27.5°S, 30–37.5°S, 40–47.5°S, and 50–57.5°S. The frequency reduces gradually from south to north southward of 12.5°S and increases again where a local maximum at 7.5°S is observed.

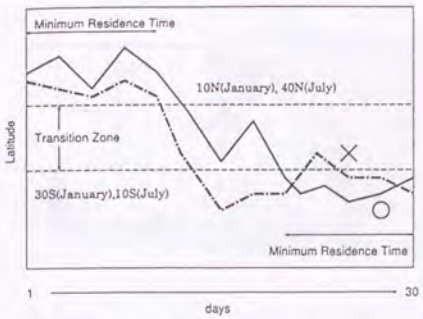

Fig. 3. Schematic diagram for selection of trajectory. Transition zone and minimum residence time was set to confirm the part of the air that belongs to each hemisphere at initial and terminal periods. See text for details.

Table 1. Number of trajectories selected from those calculated during 30 days for (a) January and (b) July 1989. Latitudes at each column indicate the transition zone. Minimum residence time is five days. For details, see text.

(a) January

| | 20S-EQ | 10S-10N | EQ-20N |
|---|---|---|---|
| North to South | 445 | 597 | 1014 |
| South to North | 475 | 599 | 489 |
| | 30S-EQ | 20S-10N | 10S-20N |
| North to South | 134 | 176 | 295 |
| South to North | 171 | 133 | 137 |
| | 40S-EQ | 30S-10N | 20S-20N |
| North to South | 17 | 39 | 85 |
| South to North | 36 | 26 | 23 |
| | 50S-EQ | 40S-10N | 30S-20N |
| North to South | 4 | 4 | 15 |
| South to North | 18 | 5 | 3 |

(b) July

| | 10N-30N | 20N-40N | 30N-50N |
|---|---|---|---|
| North to South | 981 | 1514 | 1629 |
| South to North | 432 | 394 | 419 |
| | EQ-30N | 10N-40N | 20N-50N |
| North to South | 448 | 454 | 765 |
| South to North | 175 | 107 | 126 |
| | 10S-30N | EQ-40N | 10N-50N |
| North to South | 184 | 177 | 157 |
| South to North | 111 | 36 | 25 |
| | 20S-30N | 10S-40N | EQ-50N |
| North to South | 11 | 54 | 53 |
| South to North | 45 | 26 | 21 |

If the local minima in Fig. 2a (20°S) and 2b (12.5°S) are used as a clue, a partial barrier can be detected at 15°S. If the steep gradient in Fig. 2a (5°S) and the local maxima in Fig. 2b (7.5°S) are used as a clue, a partial barrier can be detected at 5°S. These multiple barriers can be explained by the longitudinal variations of the latitudes of partial barriers deduced from the compositional gradient zone in the previous study (Taguchi, 1993). A longitudinal variation was also observed in the horizontal distribution of extrema latitudes (not shown).

The same statistics are presented in Fig. 2c and 2d for July, when the latitude bands for the selection of trajectories are 70–62.5°N, 60–52.5°N, 50–42.5°N, 40–32.5°N, and 30–22.5°N for southern extrema latitudes, and 20–12.5°N, 10–2.5°N, EQ-7.5°S, 10–17.5°S, and 20–27.5°S for northern extrema latitudes. For southern extrema latitudes (Fig. 2c), the frequencies decrease from north to south northward of 40°N and at 12.5°N. For northern extrema latitudes (Fig. 2d), the frequencies decrease gradually south of the Equator, forming a local minimum at the Equator and a local maximum at 7.5°N. A local minimum is observed at 32.5°N for the tracers released from 20–12.5°N. Therefore, partial barriers are speculated at 10°N and 30°N. Longitudinal variations of the horizontal position of extrema latitudes are also observed (not shown).

### *3.2 Transition zone*

The statistics of extrema latitudes presented in the previous section suggest that a large number of tracers are returned to the original hemisphere, even if tracers crossed the equator. Therefore, it is not sufficient to detect a trajectory relevant to the inter-hemispheric exchange by simply picking up any cross-equatorial trajectory which does not necessarily cover the equal area separated by the Equator. To ensure the migration, we can set two latitudes separated by a transition zone (Fig. 3). In addition to this zone, to ensure the residence in the hemisphere, we can request a minimum residence time during which parcels stay in either the northern or southern part of this zone. A minimum residence time is required in both the first and final part of the analysis period.

Table 1 shows the dependence of the zone setting on the number of trajectories selected for a minimum residence time of 5 days. The transition zone was set to cover the tropics. The zone width varies from 20 to 50°.

For the January case (Table 1a), more than 400 trajectories can be selected for the case of 20° zone width. With the same minimum residence time, the zone width was increased as the row decreases. The

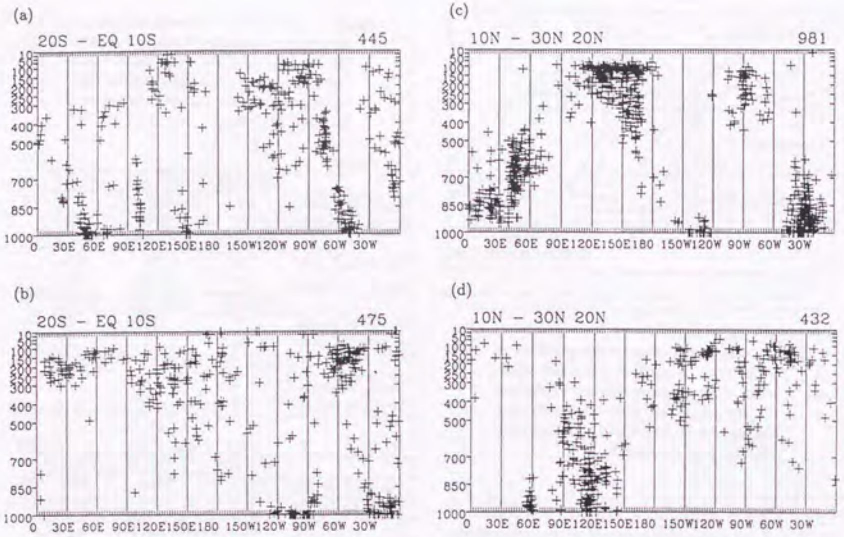

Fig. 4. Entry points for trajectory relevant to interhemispheric exchange: (a) entry point at 10°S for north-to-south motion for the transition zone of 20°S and the Equator for January, (b) south-to-north motion, (c) at 20°N for north-to-south motion for the transition zone of 10°N and 30°N for July, and (d) south-to-north motion.

number selected is reduced with the increase of zone width because a smaller number of tracers could transverse the zone.

The number selected also changes with the shift of the zone from south (left) to the north (right). The number selected for north-to-south migration increases with the northward shift of the zone. On the other hand, for south-to-north migration, the number decreases with northward shift. Thus, the number selected results in asymmetry between north-to-south and south-to-north, depending on the position of the zone.

The dependence of the selected number on the zone setting indicates a balance of two factors. One is the time required for a parcel to transverse the transition zone. The migration velocity from north to south and that in the opposite direction are probably different because of the antisymmetric vertical path of these trajectories as will be seen later (Section 4). The other is the probability of a parcel to stay outside of the transition zone. If the edge of the zone is cutting an intensive eddy, such as the Tibetan High pressure system, then the probability for a tracer sitting on either side of the edge is greatly reduced. The probability is also a function of the initial tracer distribution. In the present study, this number is affected by the net flux of tracer from high to low latitudes resulting from the latitude dependent initial distribution.

In the southward shift case (left column), the number of north-to-south migrations is smaller than south-to-north. This indicates the north-to-south transport velocity is much less than the south-to-north motion if the probability of residence on each side of the transition zone is the same. If the velocities are the same for both directions, then the difference in probability might explain this contrast. An opposite relation is observed in the northward shift case (right column).

In July (Table 1b), the number selected for north-to-south migrations does not increase with northward shift of the zone, while it decreases for south-to-north migrations.

### *3.3 Entry point*

Longitude and pressure of the entry point of the trajectories are plotted in Fig. 4. The entry point was defined as the position of a trajectory which crossed 10°S for January and 20°N for July. Only the first-time crossing was plotted for each trajectory.

In January, clusters of the entry points of trajectories from the north-to-south case (Fig. 4a) are

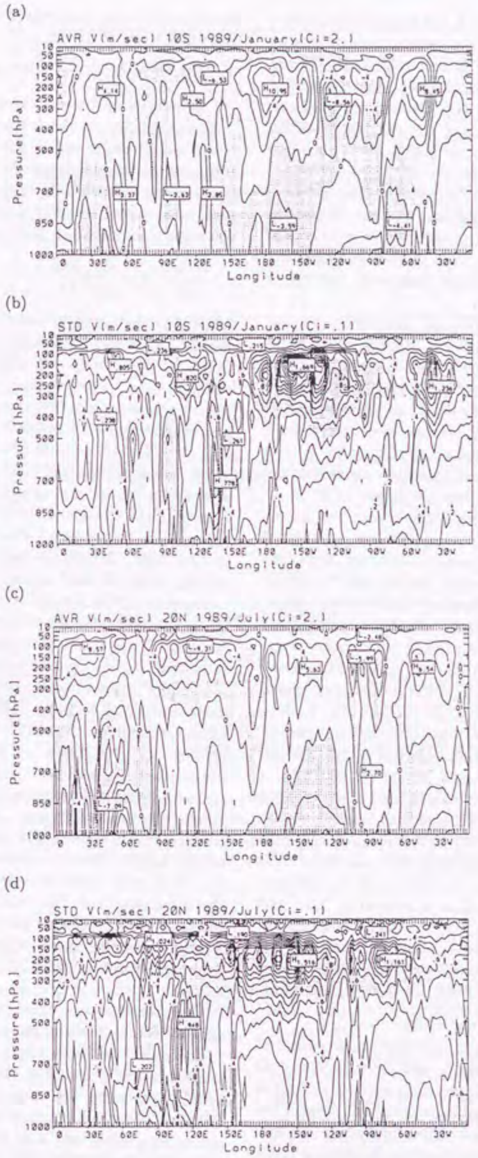

Fig. 5. Monthly average and standard deviation of the meridional component of the wind at 10°S for January and at 20°N for July of 1989: (a) mean in January, (b) standard deviation in January, (c) mean in July, and (d) standard deviation in July.

observed in four regions in the lower troposphere. A cluster is observed in the middle troposphere at 70°W. Two clusters (130°E, and 150°W–90°W) are observed in the upper troposphere. For the south-to-north cases (Fig. 4b), two clusters are observed in the lower troposphere and two clusters (0–90°E, 60°W) and scattered feature (90°E–90°W) are observed at upper troposphere.

For the north-to-south case in July (Fig. 4c), two clusters in the lower troposphere and two clusters in the upper troposphere were observed. For the south-to-north cases (Fig. 4d), one cluster in the lower troposphere and a scattered feature in the upper troposphere are observed.

These clusters are indicating that there are preferred areas for atmospheric motion relevant to inter-hemispheric exchange. Let us compare these preferred areas with monthly-averaged meridional winds and the standard deviation of the winds. Figure 5 shows the monthly average of the northward winds (a, c) and its standard deviation (b, d). In January, the average and standard deviation are shown at 10°S. In July, they are shown at 20°N.

The distribution of the entry points has a correspondence with the average of the northward winds rather than the standard deviation, such that north-to-south entry points correspond to southward winds and south-to-north entry points correspond to northward winds. Therefore, in general entry points could be expressed in monthly average of the northward winds. At some points, however, monthly-averaged wind has no correspondence with the entry points. At 170°W, 850 hPa, in January, a large southward wind (3.6 m/sec) was observed (Fig. 5a) but there is only one north-to-south entry point (Fig. 4a), while at 70°W, 850 hPa, a large number of north-to-south entry points were accompanied with similar-size (4.4 m/sec) southward winds. At 70°W, 500 hPa, a number of north-to-south entry points are observed but only weak southward wind is there. In July, at 90°E, 150 hPa, the southward wind region is extending from the East, but there are only a few north-to-south entry points. These differences are demonstrating that there is a limitation to defining the distribution of entry points using a monthly average of the winds.

### *3.4 Tying together the trajectories*

To display the conveyor belt, it is not necessary to show all of the trajectories in each belt. In fact, if all of the trajectories are drawn on a horizontal map or a latitude vertical projection, one cannot observe the conveyor belt because all trajectories are combined. Instead, it might be helpful to bundle them in order to perceive the conveyor belt clearly. One way to tie them together is to show a representative path by making the conditions more strict. Table 1 is used as a basis for the tightening of the criteria. For January, the transition zone of 30°S to 10°N is used, and 10°S to 40°N for July.

## 4. Characteristics of the Lagrangian motion

### *4.1 Hysteresis of the trajectory*

The reliability of the trajectory calculation was tested using water vapor amount. The potential temperature should change with the change of the water vapor amount if the trajectory follows the real atmospheric motion. For a saturated atmosphere, the energy conservation law results in

$$\frac{D\log\theta}{Dt} = -\frac{L_c}{c_pT}\frac{Dq_s}{Dt}, \qquad (1)$$

where $\theta$ is the potential temperature, $L_c$ the latent heat of evaporation or condensation, $c_p$ the heat capacity of dry air, $q_s$ the saturation mixing ratio, and $t$ is time. This relation is satisfied if the trajectory traces air motion precisely and condensation and evaporation take place without exchange of energy with the air outside of the parcel. Time variation over an increment of 12-hours is used instead of dividing the variation by the seconds in 12 hours. Note that the change of about 3 K in potential temperature corresponds to about 0.01 change in the vertical axis. If the atmosphere is not saturated, mixing ratio $q$ is used instead of $q_s$.

There are three limitations for this method. One is the spatial resolution of the atmosphere that we can use. Even if the grid-scale atmosphere is not saturated, it may contain a fraction of cloud which can reduce the grid-scale temperature by the evaporation of cloud droplets. The second is that if the whole atmosphere is saturated, a trajectory connecting any two points in the atmosphere satisfies the relation (1), because both potential temperature and saturation mixing ratio are a unique function of pressure and temperature. The third is the poor observation of water vapor, especially at high altitudes. Dispite these limitations, a departure from Eq. (1) is still useful to evaluate the departure of the trajectory from the real motion of the air, because a wrong tracing of air motion can easily make a large difference in water vapor amount since the water vapor mixing ratio has a fine horizontal structure.

Figure 6 shows an example of the time sequence of a trajectory selected as north-to-south migration in January. The latitude (a), pressure (b), potential temperature (c) , mixing ratio of water vapor and relative humidity (d), time derivative of the logarithm of potential temperature, and time change of the mixing ratio with a factor in rhs of Eq. (1) (e) are shown for 30 days. The first day is not shown. The transition zone is indicated in (a) by a dotted line.

An air parcel was initiated at 50°N and stayed north of 40°N for the first four days. Then it turned southward until Day 28. It was initiated at 400 hPa and stayed above 500 hPa for the first four days, then went down to the lower troposphere in the tropics as it turned southward and upward around Day 19 (b). Potential temperature (c) was almost constant before it moved upward on Day 19. The water vapor mixing ratio (d) is inversely correlated with the time variation of pressure. It decreased at Day 19 along with the uplift accompanied by increasing potential temperature (c).

The time change of potential temperature and the mixing ratio of water vapor is compared in Fig. 6e. The solid line is for the twelve-hour difference of the natural logarithm of potential temperature, and the dotted line for that of the water vapor mixing ratio. The variations almost parallel each other, indicating that the change in potential temperature is due to condensation of water vapor and evaporation of liquid water.

The correlation between potential temperature and water vapor is analyzed for the trajectories selected for inter-hemispheric migration. Figure 7 shows a scatter diagram for both terms in Eq. (1), when the tracers are located between 800 and 300 hPa in the transition zone. The diagram is shown for each set of motions, January north-to-south (a), south-to-north (b), July north-to-south (c), and south-to-north (d). Open marks indicate

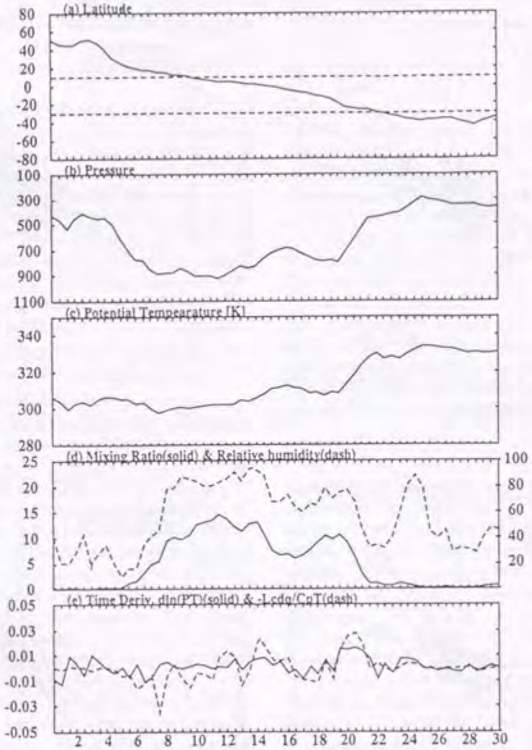

Fig. 6. An example of the time chart of the parcel which was selected in January as north to south migration. Latitude (a), pressure (b), potential temperature (c), mixing ratio (solid), and relative humidity (dash) (d), time derivative of the logarithm of potential temperature (solid) and the time derivative of the mixing ratio with a factor in Eq. (1) (dash) (e). The transition zone in this month is shown in (a).

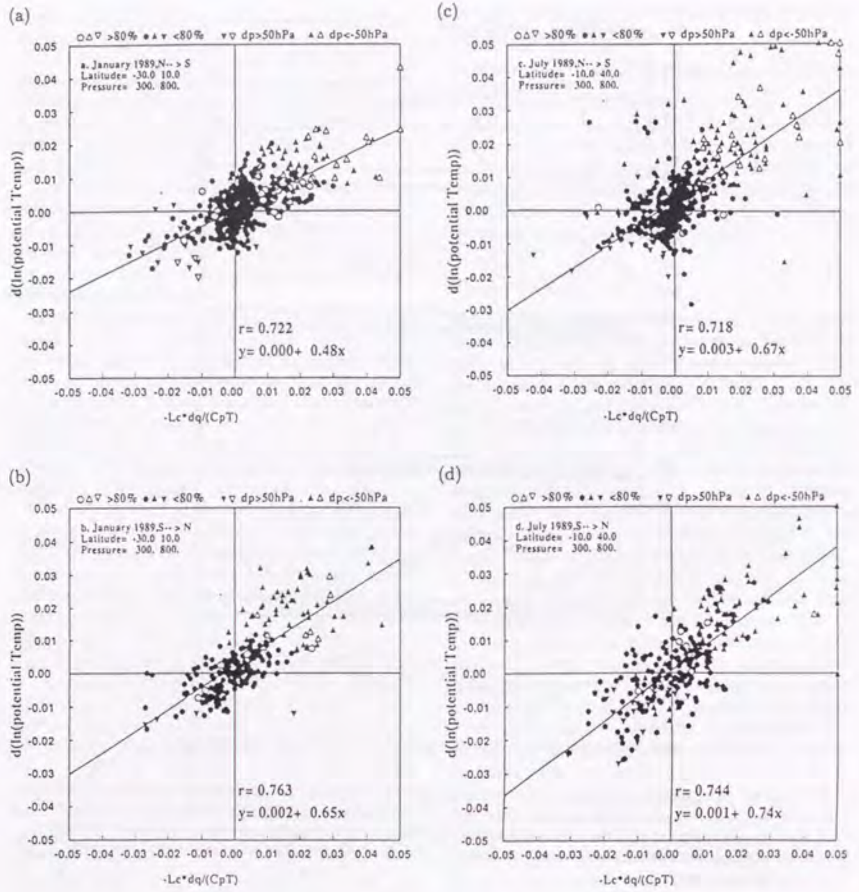

Fig. 7. Time change of potential temperature versus the mixing ratio with the factor indicated in Eq. (1). The directions of triangles indicate the motion of the air, and circles indicate that the pressure change is less than 50 hPa. Open marks indicate the relative humidity is larger than 80 %. Data were plotted only when the mean position was inside the transition zone and between 300 and 800 hPa. The line indicates the regression relationship. The relative coefficient was shown in the right bottom position. (a) January, north to south, (b) south to north, (c) July, north to south and (d) south to north.

that the relative humidity is above 80 %. The shape indicates the direction of the motion of the tracer; upward triangles indicate that the pressure decreased more than 50 hPa, downward triangles that the pressure increased more than 50 hPa, and circles that the pressure changed less than 50 hPa. A regression line and relative coefficient are also drawn in the diagram.

In all of the migrations, an increase of potential temperature is associated with upward motion and the condensation of water vapor amount (upper right side of the diagram). Decrease of potential temperature is not necessarily accompanied by downward motion or evaporation of water vapor. In

spite of the asymmetry in the distribution of the time variation in potential temperature, the regression line cuts almost through the original point, indicating that there is no systematic drift in the tracing.

Although the dots are clustered around the original point, indicating that the trajectories almost follow isentropic surfaces, this diagram also demonstrates that tracing atmospheric motion on isentropic surfaces in the tropics is useless.

If this analysis is extended to the upper troposphere (not shown), the correlation is distorted owing to insufficient water vapor observations. If it is extended below 800 hPa, the correlation is also distorted because the trajectories sometimes enter the planetary boundary layer and surface of the ground. In those situations, the conservation of energy cannot be expected.

### *4.2 3-D structure of conveyor belt in January*

The conveyor belt which connects the Northern and Southern Hemisphere can be displayed in a horizontal map and a latitude height projection. Figure 8 shows the horizontal (a) and vertical (b) distributions of trajectories which migrated from north to south in January. In the horizontal plane (a), the color indicates the instantaneous pressure level of the particle. Along the Equator, there are three regions where trajectories are clustered: east Indian Ocean, the East-Pacific, and Amazon. The trajectories at the Indian Ocean and the Amazon are colored in red, indicating that they are moving in the lower part of the troposphere. The particles in the East-Pacific region are colored in yellow to blue, indicating that the trajectories pass through the upper part of the troposphere. Those regions are consistent with Fig. 4a.

In the vertical plane (b), color indicates the pressure level of the origin. Most of the trajectories initiated from the middle latitudes while the altitude diverged in the troposphere. Some trajectories colored in yellow and green descended as they moved to the tropics and ascended gradually after invading the Southern Hemisphere. Some trajectories colored in blue in the upper part of the troposphere directly invaded the Southern Hemisphere. They correspond to the paths in the East-Pacific in Fig. 8a.

Figure 9 is the same as Fig. 8 except for the trajectories from south to north. If the trajectories are classified according to the position at the Equator, we can recognize three groups: (1) Atlantic, (2) Indonesia, and (3) Africa. They are shown in Fig. 4b, while entry points at the East Pacific in Fig. 4b are missing in Fig. 9. We can observe the change of color from red to yellow around the Equator. The change of color indicates that the trajectories are lifted in convection since the color change is more rapid than in the case in Fig. 8a. This situation can be confirmed in Fig. 9b where the trajectory is lifted almost vertically from 20°S to the Equator. There is a set of trajectories which passes only around 100 hPa and is observed at the east coast of south America. This group has the largest contribution in Fig. 4b.

Note that the vertical distribution of the trajectories for north to south (Fig. 8b) and for south to north (Fig. 9b) are not symmetric. This asymmetry might be important to the hemispheric inventory of materials and momentum.

There are three convective centers in the tropics: Africa, Indonesia, and the Amazon. The role of the exchange of material is different for each convection center. Convection in Africa acts as a barrier, that in Indonesia transports material from south to north. Convection at the Amazon exchanges materials between north and south by the baroclinic flow structure: southward transport in the lower part and northward transport in the upper part.

### *4.3 3-D structure in July*

Figure 10 is the same as Fig. 8 except for July. Most of the trajectories are confined in a narrow region over the West Pacific in the upper troposphere. There are some trajectories in Africa and Central America, which changed their color from red to green. These three groups are consistent with the entry point in Fig. 4c. In the vertical plane (b), two typical flows are obvious: one is the path in the upper troposphere only and the other is moving in the lower troposphere and lifted in the tropics.

Figure 11 is the same as Fig. 9 except for July. Most of the trajectories are confined over the Indian Ocean (a). Most of the upper tropospheric trajectory associated with the entry points in Fig. 4d was eliminated in this case.

Again, the vertical distributions of the trajectory are not symmetric with respect to the migration direction (Figs. 10b and 11b). For the trajectory from the winter to the summer hemisphere, the typical paths are observed near the ground. For the case from the summer to the winter hemisphere, trajectories descend to the lower troposphere in the original hemisphere and are lifted in the ITCZ and transported to the other hemisphere.

The basic features in this analysis for January and July were obtained using meteorological data of a different year (not shown).

## 5. Trajectories in frozen winds

### *5.1 January*

In order to see the effect of time variation of the wind contributing to the exchange of the trajectory between hemispheres, the same statistics are performed on the trajectories calculated for the wind at 00UTC January 16. This date is selected because the wind fields in the middle of January are

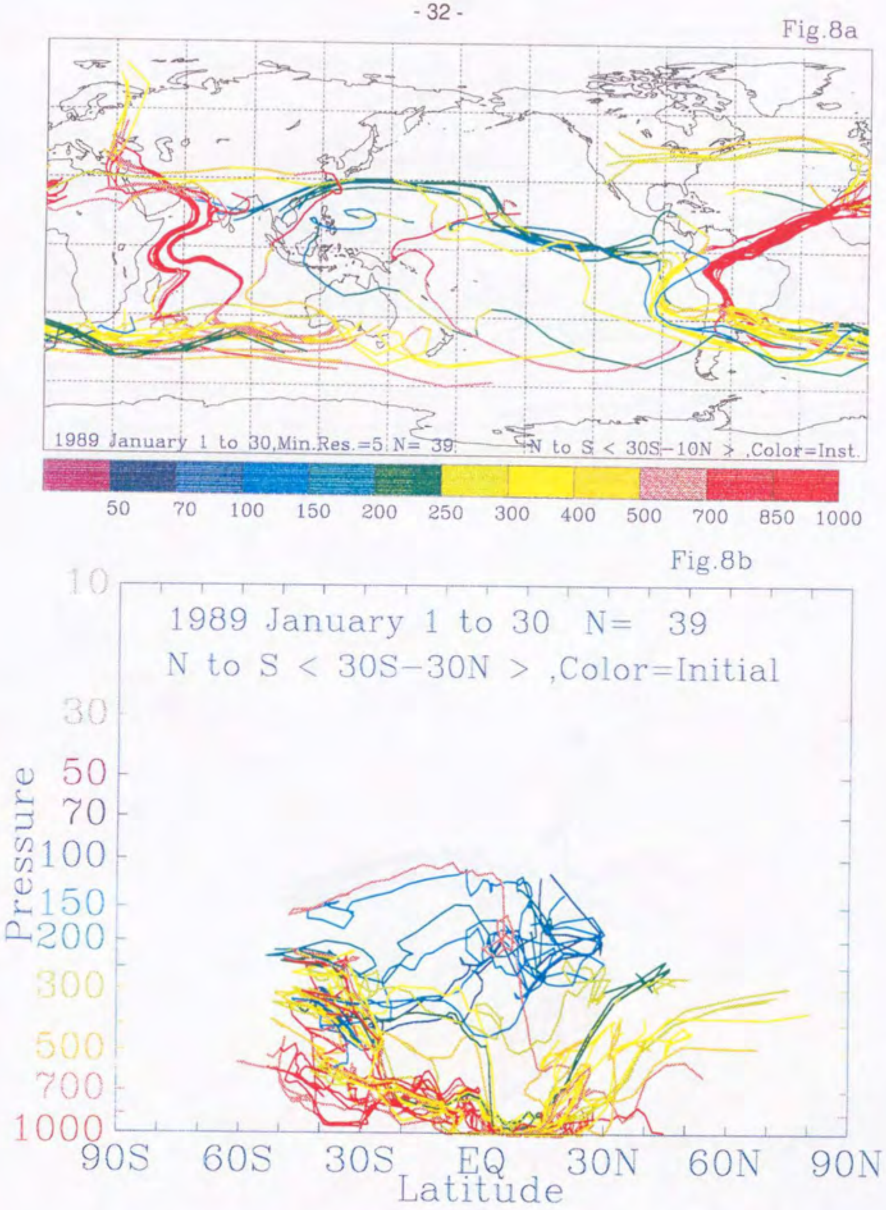

Fig. 8. Selected trajectories in January from north to south for the transition zone between 30°S and 10°N: (a) horizontal plot, (b) vertical plot. For details, see text.

Fig.9a

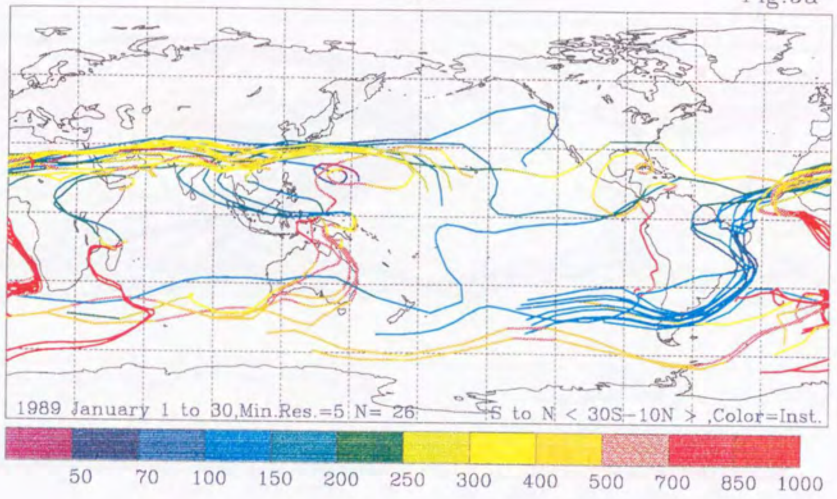

Fig.9b

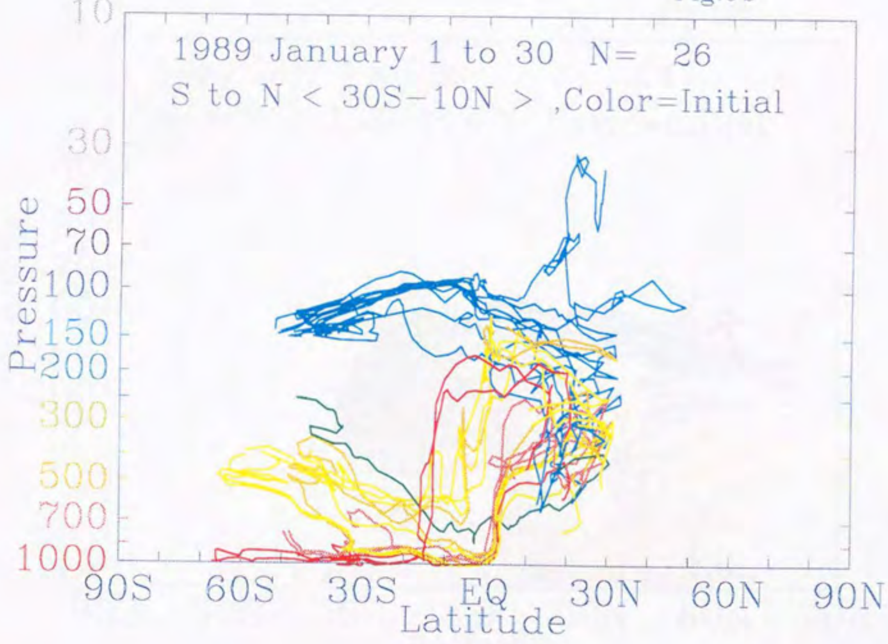

Fig. 9. Same as Fig.8 except for south-to-north.

Fig.10a

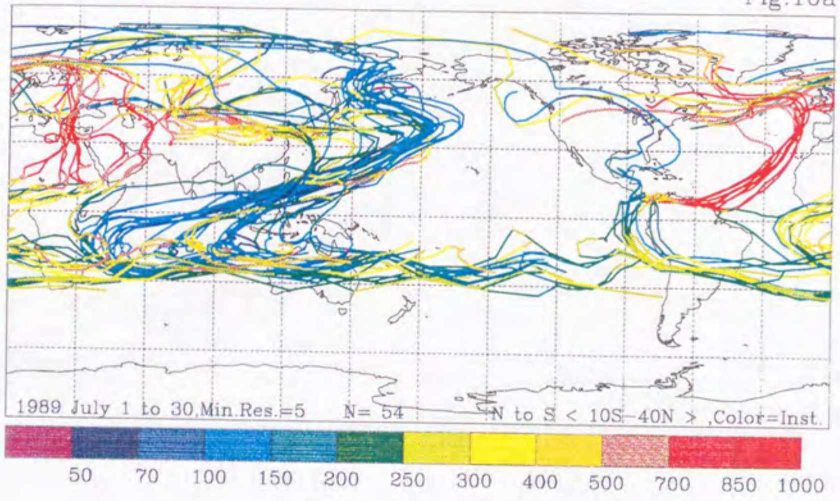

Fig.10b

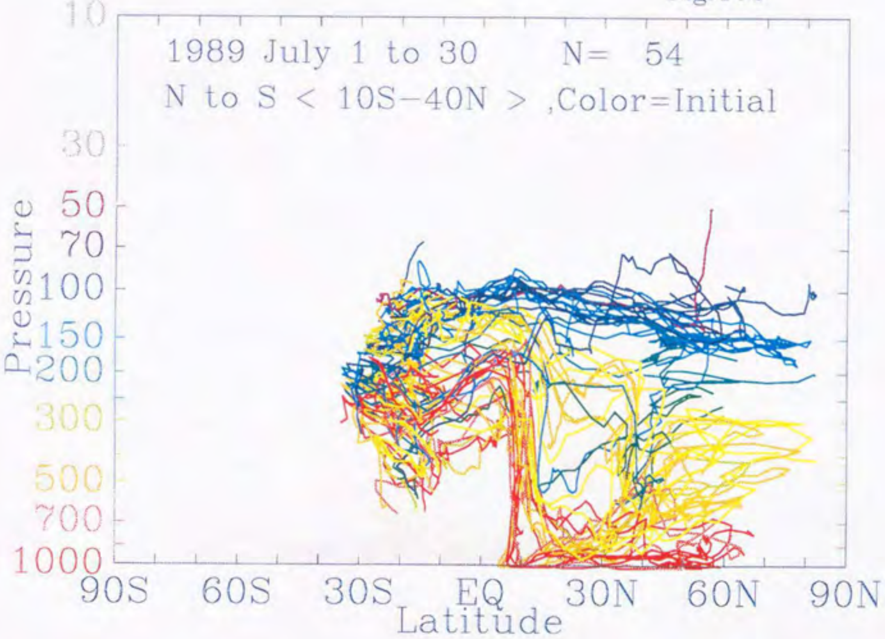

Fig. 10. Same as Fig.8 except for July for the transition zone between 10°S and 40°N.

Fig.11a

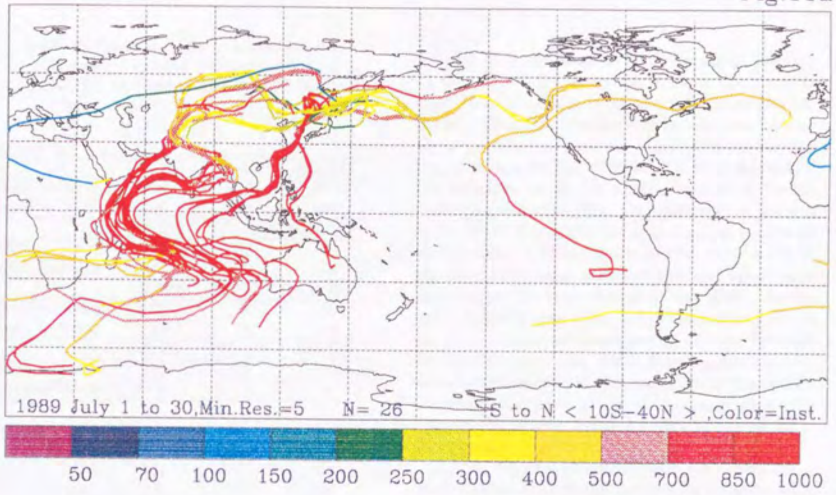

Fig.11b

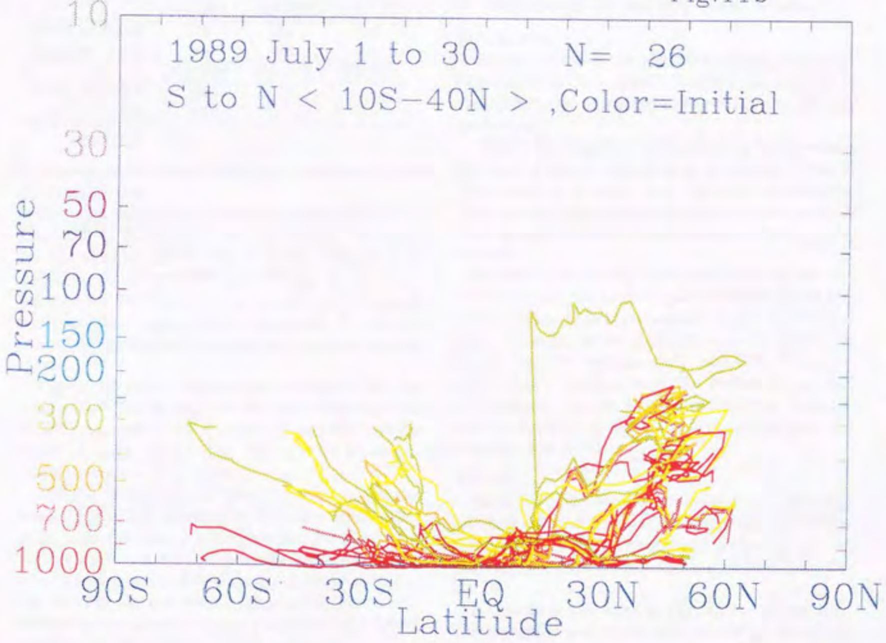

Fig. 11. Same as Fig.9 except for July.

Table 2. Same as Table 1, except for trajectories calculated for fixed wind of (a) 00UTC 16 January and (b) 00UTC 15 July.

(a) January

| | 20S-EQ | 10S-10N | EQ-20N |
|---|---|---|---|
| North to South | 499 | 616 | 617 |
| South to North | 729 | 885 | 549 |
| | 30S-EQ | 20S-10N | 10S-20N |
| North to South | 146 | 196 | 159 |
| South to North | 142 | 312 | 210 |
| | 40S-EQ | 30S-10N | 20S-20N |
| North to South | 25 | 66 | 48 |
| South to North | 15 | 26 | 59 |
| | 50S-EQ | 40S-10N | 30S-20N |
| North to South | 15 | 21 | 15 |
| South to North | 0 | 2 | 4 |

(b) July

| | 10N-30N | 20N-40N | 30N-50N |
|---|---|---|---|
| North to South | 902 | 373 | 183 |
| South to North | 590 | 337 | 322 |
| | EQ-30N | 10N-40N | 20N-50N |
| North to South | 398 | 155 | 27 |
| South to North | 277 | 108 | 107 |
| | 10S-30N | EQ-40N | 10N-50N |
| North to South | 156 | 55 | 11 |
| South to North | 152 | 18 | 37 |
| | 20S-30N | 10S-40N | EQ-50N |
| North to South | 23 | 15 | 4 |
| South to North | 54 | 8 | 2 |

most responsible for the trajectory presented in the previous section.

Table 2a lists the numbers selected for the criterion used in Table 1, but for trajectories calculated for the wind at 00UTC January 16. Compared to Table 1a, for 20 and 30° zone widths, the numbers selected for south-to-north migration are increased while all other numbers are decreased. The results cannot be generalized because only one case was analyzed.

Figure 12 shows trajectories calculated for the wind at 00UTC January 16. For the transition zone of 30°S and 10°N, 66 trajectories are selected for north-to-south motion (Fig. 12a) and 26 for south-to-north motion (Fig. 12b).

For the north-to-south case (a), paths over the Indian Ocean are observed as in Fig. 8 while other path, over the East Pacific and the Amazon, cannot be seen. Some trajectories are observed in the West-Pacific where a few trajectories are observed in Fig. 8a. For the south-to-north case (b), three convection centers-South Africa, Indonesia, and South America-are responsible for the transport.

### *5.2 July*

Table 2b is the same as Table 2a except for July 15 00UTC. If the transition zone is the same as Figs. 10 or 11, the number selected was greatly reduced. Thus, the southern boundary was relaxed 10° to get reliable statistics. Figure 13 is the same as Fig. 12 except for July 15th 00UTC with the boundary latitudes set at the equator and 40°N. In the north-to-south case (Fig. 13a) the relative amount in the lower and upper paths is changed compared to Fig. 10a. The reduction of the upper path in the fixed-wind mode indicates that the upper path depends on the time change of the wind. In the south-to-north case (Fig. 13b), the major path in the Indian Ocean as shown in Fig. 11a was detected but another path over South America was also observed. This indicates that the path in the Indian Ocean is stationary and that the exchange path with helicoid shape over south America appeared for a short period.

Figures. 12 and 13 demonstrate that there are a large number of exchange paths in an instantaneous wind field. And also, these exchange paths partly explain those observed in Figs. 9, 10, 11, and 12.

## 6. Trajectories in monthly-mean winds

### *6.1 January*

In order to assess the possibility of using monthly-mean wind for the global transport, an analysis of the trajectories using monthly-averaged winds was performed.

Table 3 lists numbers selected using the monthly-averaged wind for the criteria of Tables 1 and 2. The numbers selected were reduced dramatically. No trajectory was selected for the transition zone in the time-dependent mode, so the condition is greatly relaxed.

Figure 14 shows the trajectories selected for the transition zone set at 20°S and 10°N from those calculated in the monthly-averaged wind fields for January. Trajectories are confined in narrow longitude bands. For the north-to-south case (Fig. 14a), trajectories are obtained over the Indian Ocean and the Amazon. For the south-to-north case, trajectories are obtained in the upper troposphere over the Amazon (Fig. 14b).

### *6.2 July*

Table 3b is the same as 3a except for July. The numbers selected for south-to-north paths are larger than Table 1b in the southward shift case but, in general, the numbers selected are smaller than Table 1b.

Figure 15 is the same as Fig. 14 except for July. The transition zone is the same with Figs. 10 and 11. In the north-to-south case (a), only one set of trajectories is obtained over Africa. The particles are

Fig.12a

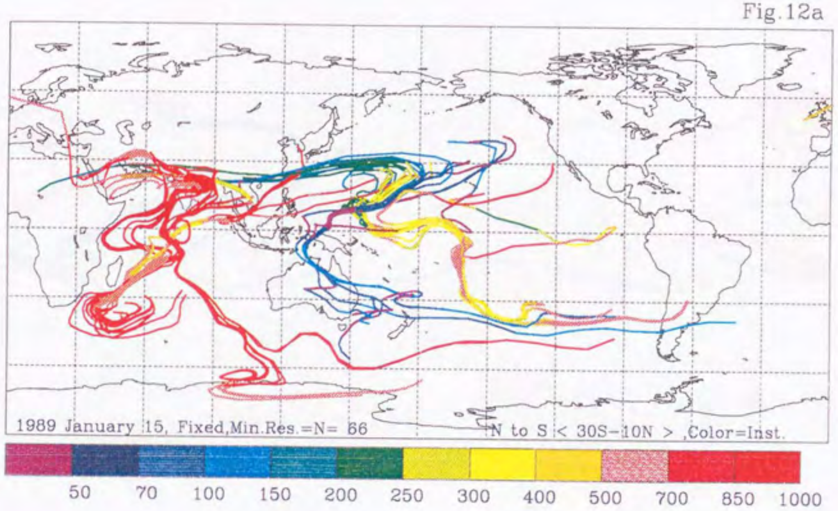

Fig.12b

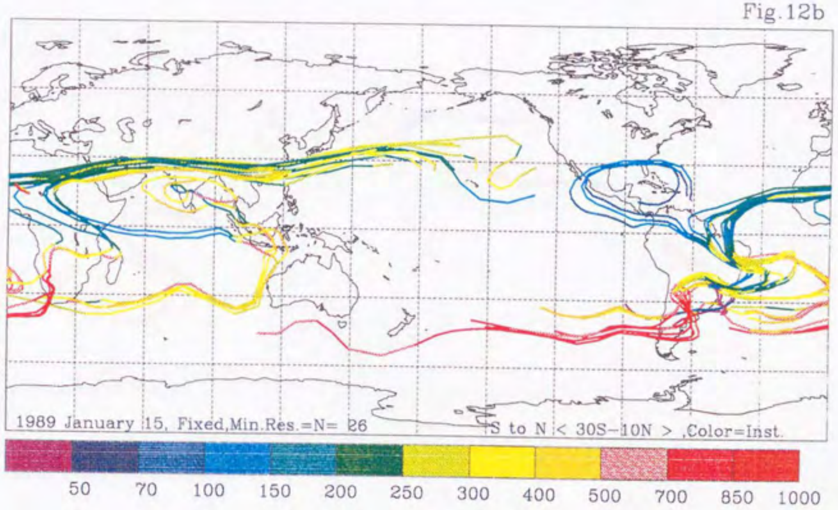

Fig. 12. Selected trajectories from north to south for fixed or frozen winds at January 16 00UTC, for the transition zone between 30°S and 10°N: (a) north to south, (b) south to north.

Fig.13a

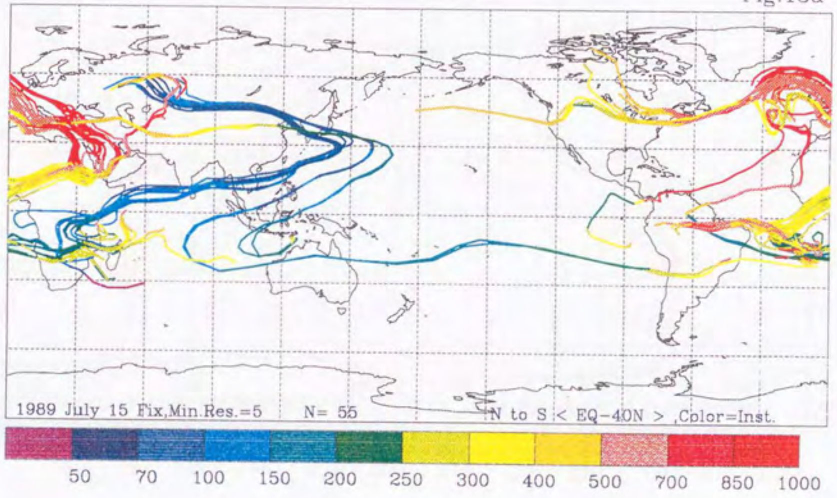

Fig.13b

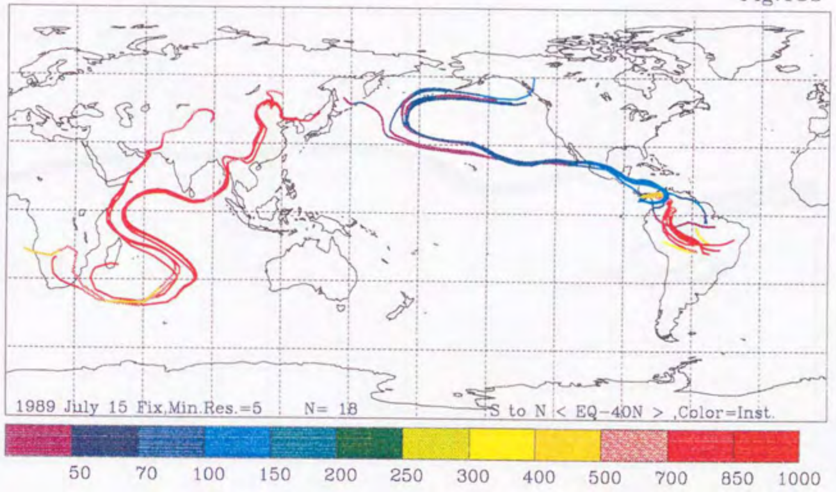

Fig. 13. Same as Fig. 12, except for July 15 00UTC, for the transition zone of the Equator and 40°N.

Fig.14a

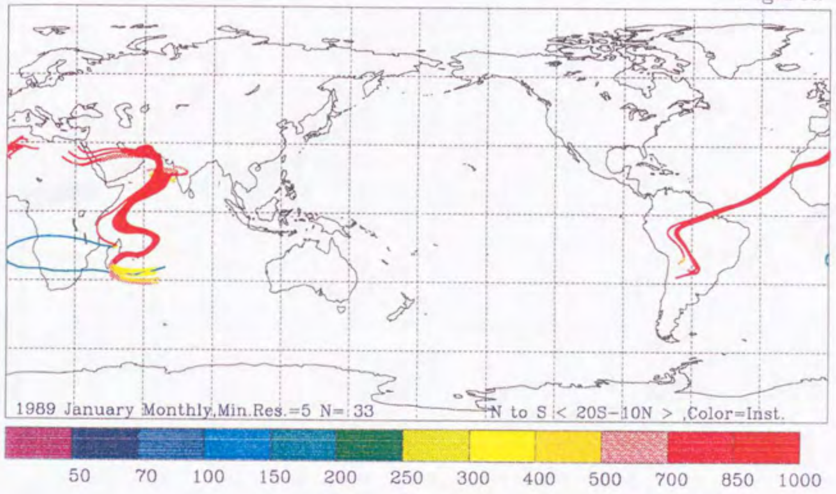

Fig.14b

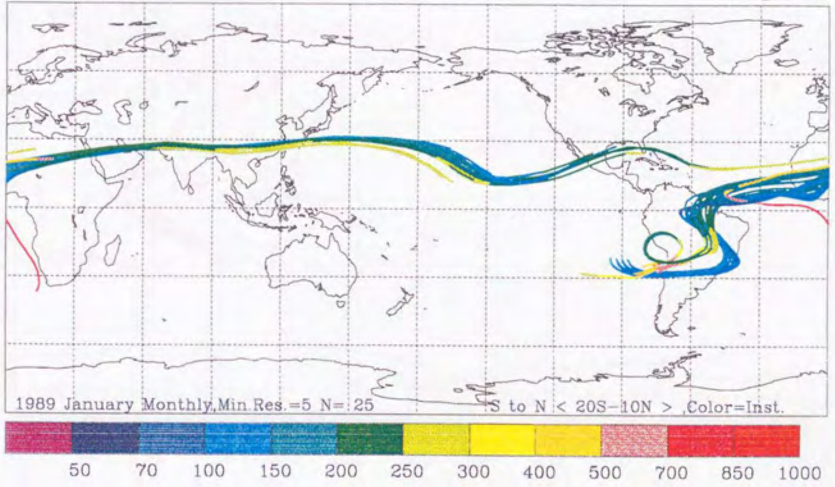

Fig. 14. Selected trajectories from north to south for monthly-averaged winds in January, for the transition zone of 20°S and 10°N: (a) north to south, (b) south to north.

Fig.15a

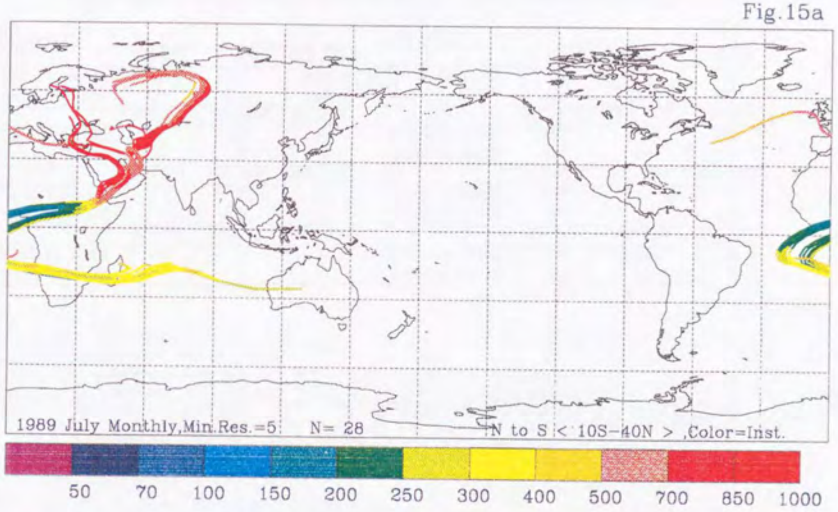

Fig.15b

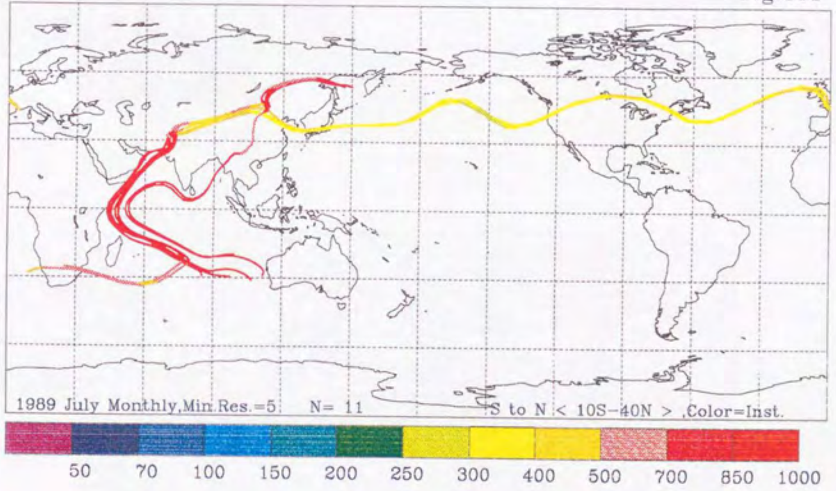

Fig. 15. Same as Fig.14, except for July, for the transition zone of 10°S and 40°N.

Table 3. Same as Table 1, except for monthly-averaged wind at (a) January and (b) July 1989.

(a) January

|  | 20S-EQ | 10S-10N | EQ-20N |
|---|---|---|---|
| North to South | 71 | 272 | 609 |
| South to North | 138 | 357 | 218 |
|  | 30S-EQ | 20S-10N | 10S-20N |
| North to South | 1 | 33 | 101 |
| South to North | 37 | 25 | 48 |
|  | 40S-EQ | 30S-10N | 20S-20N |
| North to South | 0 | 0 | 12 |
| South to North | 1 | 12 | 4 |
|  | 50S-EQ | 40S-10N | 30S-20N |
| North to South | 0 | 0 | 0 |
| South to North | 1 | 5 | 3 |

(b) July

|  | 10N-30N | 20N-40N | 30N-50N |
|---|---|---|---|
| North to South | 737 | 378 | 238 |
| South to North | 570 | 168 | 180 |
|  | EQ-30N | 10N-40N | 20N-50N |
| North to South | 360 | 211 | 69 |
| South to North | 251 | 40 | 21 |
|  | 10S-30N | EQ-40N | 10N-50N |
| North to South | 227 | 64 | 34 |
| South to North | 97 | 13 | 4 |
|  | 20S-30N | 10S-40N | EQ-50N |
| North to South | 4 | 28 | 14 |
| South to North | 60 | 11 | 3 |

(a)

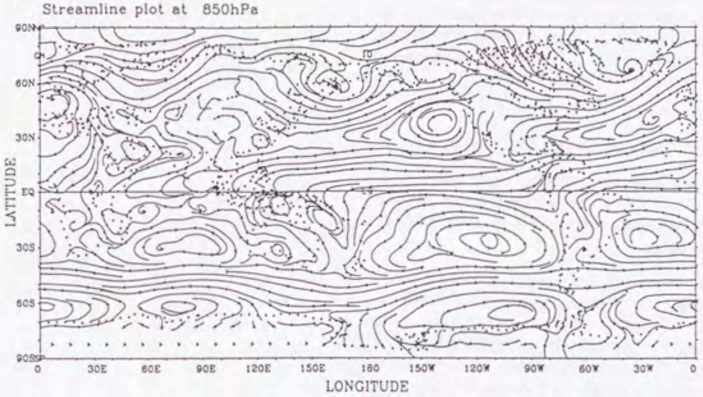

(b)

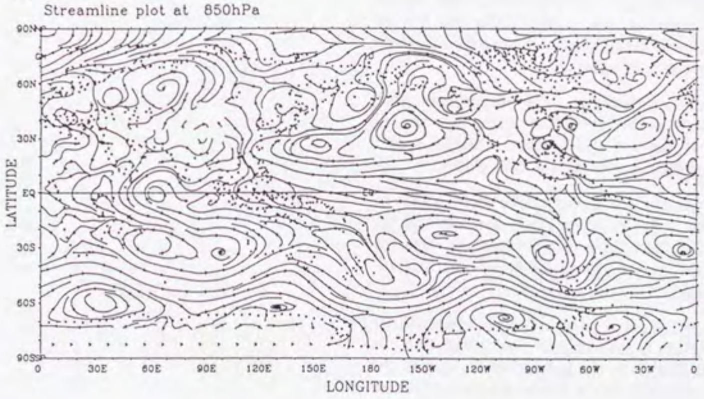

Fig. 16. Streamline of monthly-averaged winds at 850 hPa: (a) January 1989, (b) July 1989.

In July (Fig. 16b), although the south-to-north conveyor belt over the Indian Ocean is apparent (Fig. 10a), at 20°N one cannot see any north-to-south conveyor belt over Africa, nor over the Central America (Fig. 11a).

Although it is interesting to note that the conveyor belt over the Indian Ocean in July is found in the monthly-averaged wind fields, it must be stressed that there is a limitation to defining conveyor belts using monthly-averaged winds. This limitation is caused by both time variation of the wind and cross isentropic motion of the air masses. Therefore, isentropic analysis has nothing to do with this difficulty. In some global atmospheric tracer models, monthly-averaged wind is used with an artificial diffusion parameter. In those models, the north-south exchange rate might depend on the realization of the conveyor belt in the monthly-averaged wind. It is highly possible that a large artificial diffusion in the model is compensating for the lack of conveyor belt in the monthly-averaged wind.

## 7. Conclusions

Conclusions obtained in this study are as follows:

(1) There are preferred paths, conveyor belt or pipe lines, which cross the barrier between the air masses belonging to the Northern and Southern Hemispheres.

(2) The conveyor belt has a different vertical path, depending on whether it goes from north to south or south to north. When it goes from the winter to the summer hemisphere, it passes through the lower troposphere in the tropics and is lifted gradually as it descends in the high latitudes. When it goes from the summer to the winter hemisphere, it descends in the original hemisphere, is lifted in the ITCZ, and is then transported into the other hemisphere through the upper troposphere.

(3) In January, there are three major paths from north to south: low-altitude paths over the Indian Ocean and the Amazon and the upper-tropospheric path over the East Pacific.

(4) In January, the major paths from south to north are in the upper troposphere east of the Amazon, and three convection areas over the Atlantic Ocean, Madagascar Island, and Indonesia.

(5) In July, the major paths from north to south are in the upper-tropospheric flow connecting the North Pacific to the Indian Ocean, and in the convection regions in Africa and Central America.

(6) In July, the major paths from south to north are in the lower troposphere over the Indian Ocean.

# Chapter 4: Application of a chemical transport model (1): Carbon Dioxide

## Abstract

A three-dimensional tracer transport model is used to investigate the temporal trend and the annual cycle of atmospheric $CO_2$. The model transport was driven by a semi-Lagrangian scheme, using winds of 1992, analyzed at the European Centre for Medium-Range Weather Forecasts (ECMWF). A simple planetary boundary layer formulations was used to investigate the sensitivity of the model results.

Two sources/sinks distributions were used independently: fixed emission of 5.3GtC/year, estimated from fossil fuel consumption (fossil run), and a monthly distribution of the emission/absorption, estimated from a land ecosystem of the size of 14.5GtC, in terms of the Growing Season Net Flux (GSNF) (vegetation run).

The simulated inter-hemispheric contrast of the mean surface concentration, in terms of North Pole minus South Pole, is about 4 ppmv for the fossil run, and 2ppmv for the vegetation run. These results suggest that the so-called missing sink should be found in the Northern Hemisphere. On the other hand, the contrast in the vegetation run was changed by 40% while the fossil run changed by only 4% when the instantaneous planetary boundary layer (PBL) height was replaced by monthly average of PBL height. This result suggests that the monthly average PBL height can be used in place of the instantaneous PBL height only in limited cases, if it is scaled with an appropriate factor.

## 1. Introduction

The concentration of carbon dioxide in the atmosphere has been increasing since the industrial revolution. Global warming is predicted in the next century due to this increase. The primary reason for this increase is attributed to the emissions released from the combustion of fossil fuels. The amount of atmospheric $CO_2$ is increasing by only 3GtC/year, in contrast to the emission rate of 5GtC/year. The fate of the remaining 2GtC is unknown. If the emission from deforestation is taken into account, the unknown sink must be much larger. Unfortunately, the sizes of the sinks of fertilization and net oceanic absorption are not well determined. Moreover, in the 1990's, the increase in the rate of the concentration of atmospheric $CO_2$ has decreased; simultaneously, the increase in the rate of atmospheric methane has also decreased. The cause for these decreases cannot be determined due to the lack of the knowledge about the sources and sinks for both these gases. Undoubtedly, further investigations of the sources and sinks are required for the prediction of future amount of atmospheric $CO_2$.

The annual mean surface concentration of atmospheric $CO_2$ at the North Pole is higher than that at the South Pole, by about 4ppm. The peak to peak amplitude of the surface concentration in the Northern Hemisphere is about 15ppm, and 1ppm in the Southern Hemisphere. Longitudinal variation of the mean concentration and the amplitude of seasonal variation may contain information related to the surface exchange of atmospheric $CO_2$. To estimate sources and sinks of $CO_2$, an accurate three dimensional atmospheric transport model is required.

The estimation of sources and sinks has been attempted using global three dimensional atmospheric chemical transport (ACT) models. The most widely used ACT is the one developed at the Goddard Institute of Space Studies (GISS) of the National Aeronautics and Space Agency (NASA). Fung *et al.* (1983, 1987) estimated sources and sinks of atmospheric $CO_2$ by using a land ecosystem model and AVHRR data, and tried to reproduce surface concentration using the

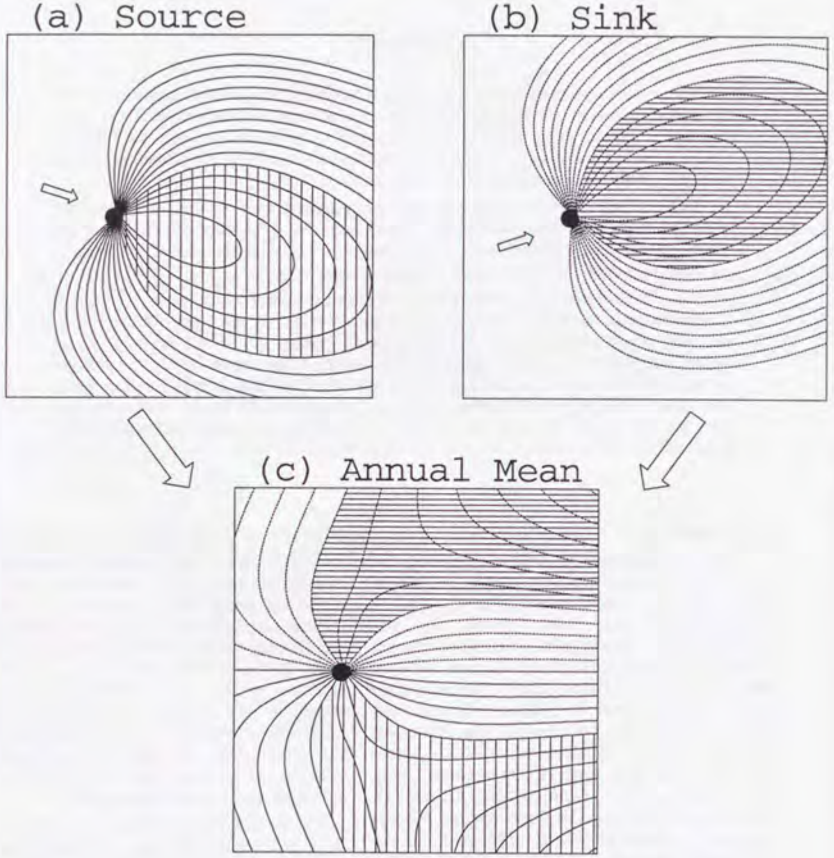

**Fig.1** Schematic interpretation of the annual average in the vegetation run. Supposing a region where $CO_2$ is emitted in the winter and absorbed in the summer, and a prevaling wind is northwest in the winter(a) and southwest in the summer(b). The area where the source makes an influence extends in the southwest and the area where the sink makes an influence extends in the northeast. Therefore, the annual average concentration has a horizontal distribution as shown in (c).

GISS model. The GISS transport model uses wind generated by a climate model (GCM), also developed at the GISS. Since the interhemispheric exchange time in the GISS transport model was too slow, Fung adjusted the exchange time by using the horizontal diffusion associated with cumulus convection in the tropics. Although the modified GISS transport model, in conjunction with Fung's land ecosystem model, could reproduce the basic features of the global distribution of minor constituents, the difference of the wind in the GCM from the observed values could easily create the difference in the distribution of the minor constituents. Furthermore, the interannual variation of the wind system, for example the El Nino Southern Oscillation, cannot be produced in the wind fields of GISS climate model. Therefore, the range of application of the GISS transport model is limited to the mean state of the atmosphere.

Heimann *et al.* (1989) further modified the GISS transport model to adopt meteorological data analyzed at the ECMWF. Since the interhemispheric exchange time was too fast using the First GARP Global Experiment (FGGE) data of ECMWF, they reduced the vertical diffusion parameter used by Fung .ul et al. (1983, 1987). They also investigated the vertical transport of the model using $^{222}$**Rn**, however, the observation of $^{222}$**Rn** was not sufficient to narrow down the uncertainty of the vertical diffusion. The horizontal diffusion was also adjusted in the GISS model by Tans *et al.* (1990). They changed the inter-hemispheric exchange time to one year. They have concluded that the sink in the Northern Hemisphere is larger than that in the Southern Hemisphere which is consistent with the observed inter-hemispheric contrast of the $CO_2$ concentration. Enting *et al.* (1992) estimated the strength and the uncertainty of the sources and sinks of atmospheric $CO_2$ with their inversion technique, using the results of the GISS model.

Although there are some variations in each application of the GISS model, all the users mentioned above appreciated the convection statistics in the GISS climate model for the vertical diffusion of the constituents. These statistics contain two types of convection: dry and moist. Dry convection takes place near the surface of the ground when the atmosphere adjacent to the ground is heated. On the other hand, moist convection takes place where moisture is abundant, i.e. in the tropics. The inter-annual variation of tropical convection may alter the global circulation of the atmosphere and may be a major source of the inter-annual variation of trace gas amounts. In this respect, there is a limited possibility of studying the inter annual variation of minor constituents using the GISS model.

Horizontal diffusions are also introduced in those GISS models that assumed that moist convection has a significant role in the horizontal diffusion due to vertical lifting, through convection and mixing by the vertical transport. The results look quite reasonable for minor constituents without surface sinks, such as CFC-11 ( Prather *et al.* , 1987).

The surface concentrations of the minor constituents at the down wind region of their surface sources and sinks are subjected to the prevailing winds at each season if the region is a source in a particular season and is a sink in another season. Figure 1 illustrates the situation where prevailing winds at the source season, say winter, are north-west and in the sink season, say summer, are south-west. The observed surface concentrations are larger than the background in the south-east area in the winter(a), whereas they are smaller than the background in the north-east area in the summer(b). The annual mean concentrations are the summation of these distributions, thus they are sensitive to the prevailing winds in the transport model and the diffusion strength, for both horizontal and vertical directions.

The pole to pole difference of the surface concentration of $CO_2$ has interannual fluctuations which can be detected in the monthly average data (Trends'91). These oscillations may be interpreted from both the fluctuations in the source strength and those in the prevailing winds. Tans .ul et al. (1990) reported that the pole to pole difference in the surface concentration is 0.25ppm, if only the land ecosystem sources and sinks are applied to the GISS model.

Taylor (1989) developed a Lagrangian transport model and simulated a global distribution of $CO_2$. His model uses assimilated meteorological data both for transport and scattering. A bimonthly average is used to calculate the position of the particles and the standard deviation of winds are used to calibrate a random number to scatter particles. The advantages of this model are that the observed winds were used and that the adjustment for interhemispheric exchange was not necessary, although the interhemispheric exchange time is 1.2 years which is 20% longer than that of Tans .ul et al. (1990). Although PBL is not specified explicitly, his model takes into account the effect of PBL automatically through the use of standard deviation of vertical motions near the surface. The disadvantage of this model is that the fluctuations of concentration with a time scale of less than two months cannot be resolved. If the pole to pole difference of surface concentration is adjusted using oceanic sinks, the difference in the concentration of the Northern Hemisphere and the middle latitudes of the Southern Hemisphere is larger than observed value, by about 2ppm.

The objectives of this paper are to describe the model developed at the National Institute for Resources and Environment and the results of the simulation of atmospheric $CO_2$ for a project of intercomparison of atmospheric transport models (TRANSCOM). Among the results of the simulation, this paper intends to demonstrate the sensitivity of PBL formulation in the ACT models, especially for sources and sinks with seasonal variation, using a global three-dimensional transport model. This model is described in section 2. The results for fossil fuel and vegetation runs are described in section 3. Conclusions are described in section 4.

## 2. NIRE-CTM-93

### 2.1. Model Formulation

The global three-dimensional model used in this study was developed at the National Institute for Resources and Environment (NIRE) in 1993 (NIRE-CTM-93). Some concepts in the second version of the Community Climate Model of the National Center for Atmospheric Research (CCM2/NCAR) (Hack *et al.* 1993) were referred to the design stage of this model, although our model is completely different from CCM2. The flow of the data is shown in Figure 2. The meteorological data analyzed at the ECMWF (TOGA/Advanced) was used to model the transport and convection of minor constituents. The vertical resolution of the concentration is 15 sigma levels extending from 0.99 to 0.01, the horizontal resolution is 2.5*x*2.5° and the time interval is 6 hours. A semi-Lagrangian scheme was adopted to calculate the transport process with a mass fixer to conserve the total mass of the constituents. A non-local planetary boundary layer was used to diffuse minor constituents near the surface.

Vertical coordinates are displayed in Figure 3. Meteorological data are provided by the pressure levels (left, solid) and the concentrations of the minor constituent are estimated by the sigma coordinates (right, dotted). The trajectory data and the height of the PBL are produced using the meteorological data before calculating the tracer transport. Trajectory calculation takes 6 hours per month on a double CPU SPARC work station, whereas the PBL height is calculated in 10 minutes, monthly. The transport calculation needs 2 hours per year, using the pre-calculated trajectory data. Back trajectory data takes 470 Mega bytes per month, and the concentration data take 80Mega bytes per month. The major limitation of this model is not computing time but available disk space.

A five year simulation was performed from an initial condition of a globally homogeneous concentration of atmospheric $CO_2$ (350ppm).

We have noticed a problem in the current model. The turn around time of the stratospheric air mass is six months in the NIRE-CTM-93, if the stratospheric air mass is divided by flux through tropopause, although it should be two years, based on $^{14}C$ observations. The results at lower troposphere are probably insensitive to this shortcoming, so the revision of this deficiency is out of the scope of the present study.

### 2.2. Meteorological Data

Since the NIRE-CTM-93 is directly linked with the meteorological data, the description starts from the meteorological data. The meteorological data analyzed at the ECMWF were used for the setting of vertical coordinates, the departure point calculation and the planetary boundary layer height as shown in Figure 2. The ECMWF distributed the products of the assimilated meteorological data prepared for the initial condition of the operational numerical weather forecasts system. We adopted the data called the ECMWF/TOGA/Advanced data set. We used low resolution data interpolated from the original archive in the T213/L31 hybrid coordinate system. The data are given on 2.5 horizontal resolution and 15 vertical pressure levels, as shown in Figure 3.

The procedure to assimilate the data is partly described in ECMWF (1993). To summarize, radiosonde soundings, reports from aircraft, wind vectors from geo-stationary satellites and vertical temperature sounding from polar orbit

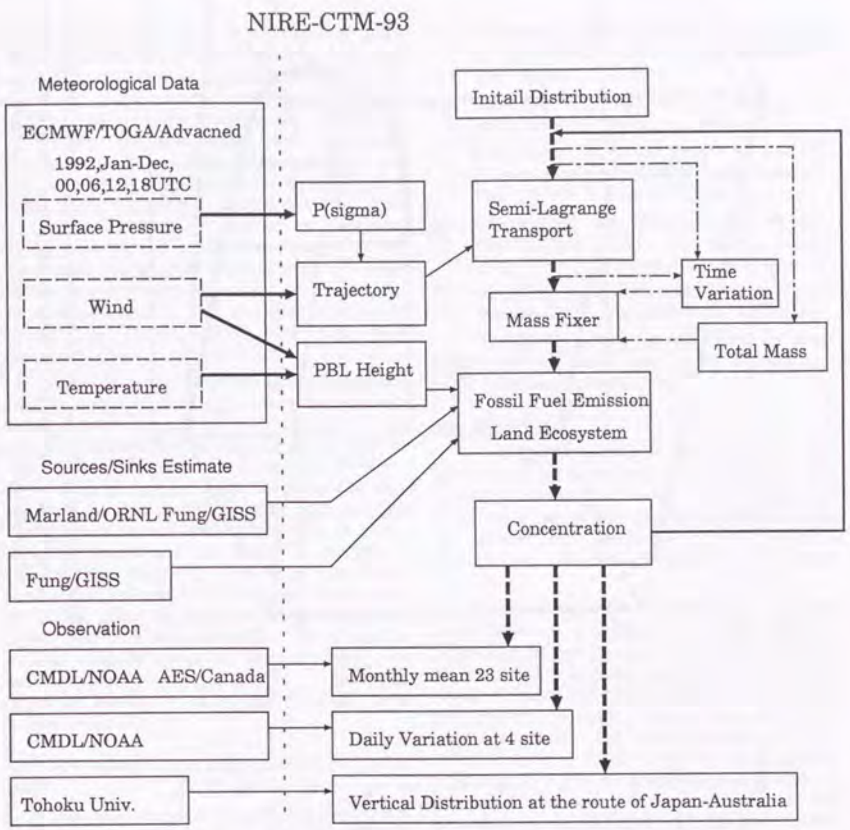

**Fig.2** Model flow and experimental design of NIRE-CTM-93 for TRANSCOM. The NIRE-CTM-93 uses meteorological data analyzed at the European Centre for Medium-Range Weather Forecasts for the calculation of pressure of the sigma coordinate, 6 hours back trajectory and planetary boundary layer height. Global homogeneous distribution of 350ppmv is set for the initial conditions. Two experiments for fossil fuel consumption and land ecosystem experiment were performed. The results are compared with CMDL and U. of Tohoku data.

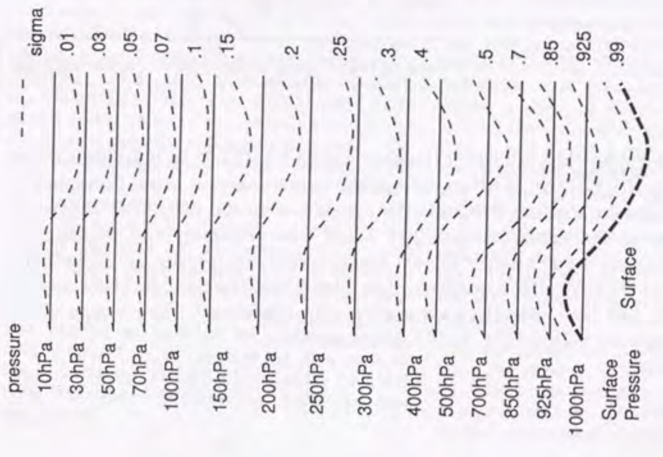

**Fig.3** Vertical coordinate system for meteorological data (presure, solid) and material concentration (sigma, dotted).

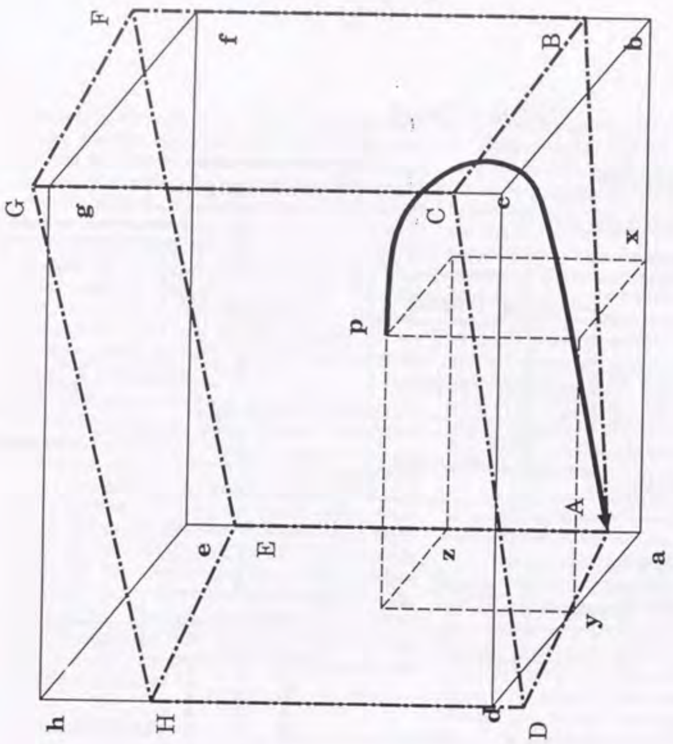

**Fig.4** Schematic view of the interpolation procedure in the material coordinate(sigma) embedded in the meteorological coordinate (pressure). The departure point P is set in the sigma coordinate system and is obtained from the wind given by the pressure coordinate system. The wind is interpolated from space and time at 30 minutes interval, although the data are given at 6 hours time intervals.

---

satellites were collected in appropriate time intervals and assimilated into data sets of a particular time. One of the most important features of the assimilated meteorological data set is that the predicted meteorological values are used in an area where the observation does not exist (Bengtsson *et al.* , 1982). The quality of the data are affected by the physical parameterization in the numerical weather prediction model. The quality of the data are studied by Trenberth (1992). He showed a significant change in the zonal mean omega field when a mass flux form of convective parameterization was included in the forecast model. The divergent component included by Unden (1989) may also have significant effects in omega fields.

When the twice daily data were used to estimate the height of PBL in the preliminary experiments, a large irregularity was observed in the surface concentrations that may be created due to local time differences. To avoid this problem, meteorological data are used four times per day, however, this did double the disk space needed. The aim to study the sensitivity of PBL height is to find a limitation in the usage of monthly or constant PBL height. It was found that inter-hemispheric exchange time was not altered with the change in the frequency of usage of meteorological data. In the preliminary test using an artificial material similar to Taguchi (1993), the inter-hemispheric exchange time is 1.0, year with respect to moving boundary, and 0.9 years, with respect to the Equator.

### 2.3. Interpolation and Departure Point Calculation

The interpolation method in this model is a simple linear with respect to three-dimensional space, similar to Taguchi (1993). A schematic view is displayed in Figure 4. Meteorological data are given on pressure coordinates (lower case, solid) and the concentration are given on the sigma coordinate system (upper case, dashed). In a semi-Lagrangian transport calculation, a departure point is estimated by successive linear interpolation of the three dimensional wind. The difference in the departure point makes different diffusion features. The departure point is stable if the wind is calculated in intervals of less than 30 minutes.

The departure point is obtained by the following procedures.

(1) Estimating a wind vector at t-15 minutes at an arrival point, using two wind vectors at t and t-6hours.

(2) Obtaining a position at t-30 minutes, by using the wind vector at t-15 minute.

(3) Calculating two wind vectors at the t-30 minutes position, by using linear interpolation in space at t and t-6 hours.

(4) Determining the wind vector at t-45 minutes, by using two wind vectors at t and t-6hours, both at the positions of t-30.

(5) Repeating steps 2 through 4 ten times, an estimate for the departure point is obtained.

Horizontal motion is calculated on three dimensional Cartesian coordinates to ensure a stable calculation at both poles.

### 2.4. Mass Fixer

A total mass fixer is incorporated since conservation of the total mass is not guaranteed during tracer transport calculation. There are at least two sources for the failure of mass conservation: convergence and divergence in the objective analysis data, and error generated by linear interpolation.

Figure 5 illustrates an example of the linear interpolation in a one dimensional framework. Supposing an initial trapezoidal distribution, as shown in (a), a homogeneous wind U transports this distribution to the right side (b). Using linear interpolation, all shapes between grid points are lost in the model. The model recognizes the distribution as (c). A simple geometric consideration may show that the shaded area in(a) and (c) are exactly the same if the grid intervals are homogeneous in the domain. In the current model, the interval of the grid is changing with pressure and latitude directions. Also, convergence and divergence in the three dimensional wind field are generated in the conversion process from the original archive (Trenberth, 1991).

A mass fixer is designed to compete with these failures in the following guide lines; (1) no adjustment on the grid (B), (2) if the total amount of $CO_2$ is increased in the model, the adjustment is applied on the concentration at the grid point of (A) only, and vice versa. With these conditions, the rate of change of time after the adjustment is always smaller than the rate of change estimated by the transport calculation.

The procedure to implement the above conditions is as follows. Let us assume M(t) and

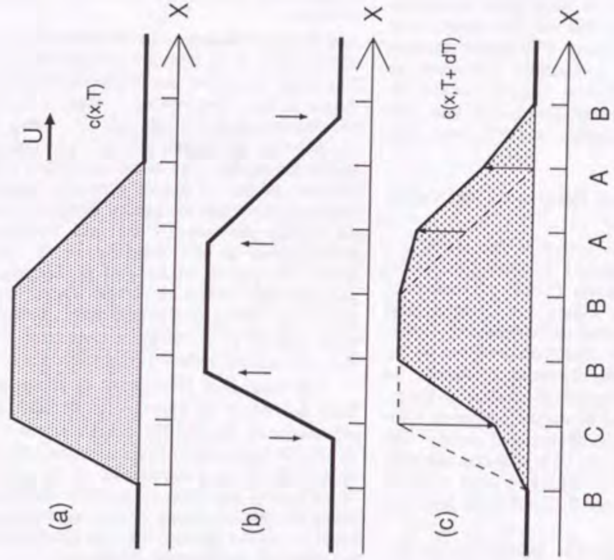

Fig.5 One dimensional explanation of the generation of artificial variation of total mass of a constituent by linear interpolation. Supposing a trapezoidal distribution of the concentration is transported by a homogeneous wind U. The total mass is indicated by the shaded area. Mass is conserved during transport procedure as long as the grid size remains the same; there is no way to conserve total mass if the grid size changes.

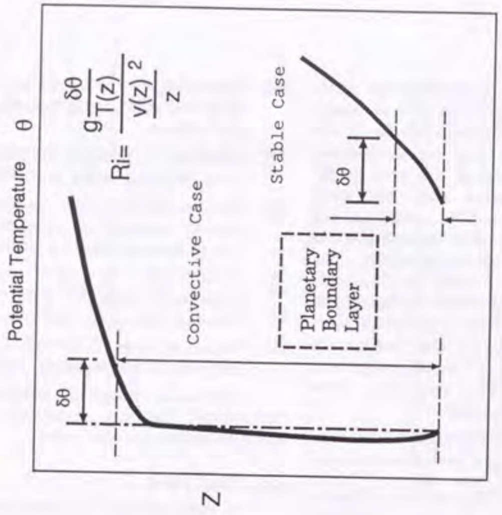

Fig.6 Schematic view of the bulk Richardson number and the height of planetary boundary layer for a typical stratification. A convective case is displayed on the left side and the stable case is on the right side.

M(t+6) as the total amount of the constituents at t and t+6hours. After the transport calculation, M(t) is not necessarily equal to M(t+6).

$$M(t+6) = \sum_{(A)}(c(t+6)_{i,j,k} - c(t)_{i,j,k})w_{i,j,l} + \sum_{(C)}(c(t+6)_{i,j,k} - c(t)_{i,j,k})w_{i,j,l} + M(t) \qquad (1)$$

where $c$ is the mixing ratio and $w$ is the weight represented by a grid point. Time variations of the weight represented by each grid are ignored.

If M(t+6) > M(t), that means that the absolute value of the first term of r.h.s. of Eq.(1) is larger than that of the second term. A coefficient $\alpha$ is introduced to the first term of the r.h.s. of Eq.1., that is,

$$0 = \sum_{(A)}(c(t+6)_{i,j,k} - c(t)_{i,j,k})w_{i,j,l}\cdot\alpha + \sum_{(C)}(c(t+6)_{i,j,k} - c(t)_{i,j,k})w_{i,j,l} \qquad (2)$$

Therefore, the concentration after the adjustment is

$$c'(t+6) = \alpha\cdot c(t+6) + (1-\alpha)\cdot c(t) \qquad (3)$$

When M(t+6)< M(t), $\alpha$ is applied to the second term of the r.h.s. of Eq.1.

The adjustment is applied at the grid point where a large variation is calculated through the transport calculation. This adjustment worked as a small diffusion. Using this mass fixer, modification is applied on 0.1% of the mixing ratio and the three digits are conserved throughout the integration for one model year (= 1464 steps ).

### 2.5. Planetary boundary layer

The interaction between the free atmosphere and the bottom boundary is modeled using a non-local planetary boundary layer. One of the aims in including the planetary boundary layer is to represent the rapid vertical mixing of the atmospheric concentration released from the surface. The other aim is to represent the trapping of the constituents below the inversion layer. The constituents released from the boundary are added with a homogeneous mixing ratio throughout the PBL. When the boundary absorbs a constituent, a homogeneous mixing ratio is subtracted form the concentration of the constituents in the PBL. When the departure point for the free atmosphere is estimated in the layer assigned as PBL, the concentration of the constituents is redistributed in the free atmosphere.

The height of the PBL is estimated by a bulk Richardson number (Troen *et al.* , 1986) defined as,

$$Ri = \frac{g\cdot\delta\theta(z)/T(z)}{v(z)^2/z} \qquad (4)$$

where $g$ gravitational acceleration, $z$ height, $\delta\theta(z)$ the difference of potential temperature between $z$ and ground, $T(z)$ temperature and $v(z)$ horizontal wind speed. Ri is a ratio between the stabilizing effect due to density stratification and the unstabilizing effect due to vertical wind shear. The layer with Ri value less than 0.25 is assigned to the PBL. Typical vertical profiles of the potential temperature and the height of the PBL for the convective and stable case are shown in Figure 6.

Monthly averages of PBL thickness at four selected months are displayed in Figure 7, where the shaded areas indicate that the PBL thickness is larger than 100 hPa. In January(a), thick PBL was obtained in the northern Pacific Ocean and the northern Atlantic Ocean, where horizontal winds are strong in that season. In April(b), thick PBL was observed in India and northwestern Africa, where the land is heated by the migration of the sun. In July(c), thick PBL was obtained over the continents in the Northern Hemisphere and over the oceans, in the Southern Hemispheres. In October(d), thick PBL was observed over the ocean, both in the Northern and the Southern Hemispheres.

### 2.6. CO$_2$ data

The monthly average of surface concentration of CO$_2$ was obtained from the National Oceanic Atmospheric Administration's Climate Monitoring and Diagnostics Laboratory (NOAA/CMDL) and from the Atmospheric Environment Service of Canada. Hourly averages of the surface concentration at the four stations were obtained by the CMDL. Monthly averages of the upper troposphere compiled by Tohoku University were used to evaluate the results of the simulation.

The location of the surface observation of CO$_2$ are shown in Figure 8. The altitude of most sites is lower than 100m, however, MLO is located at 3397m above sea level. Daily values were derived from hourly values at PBR, MLO, SMO and SPO.

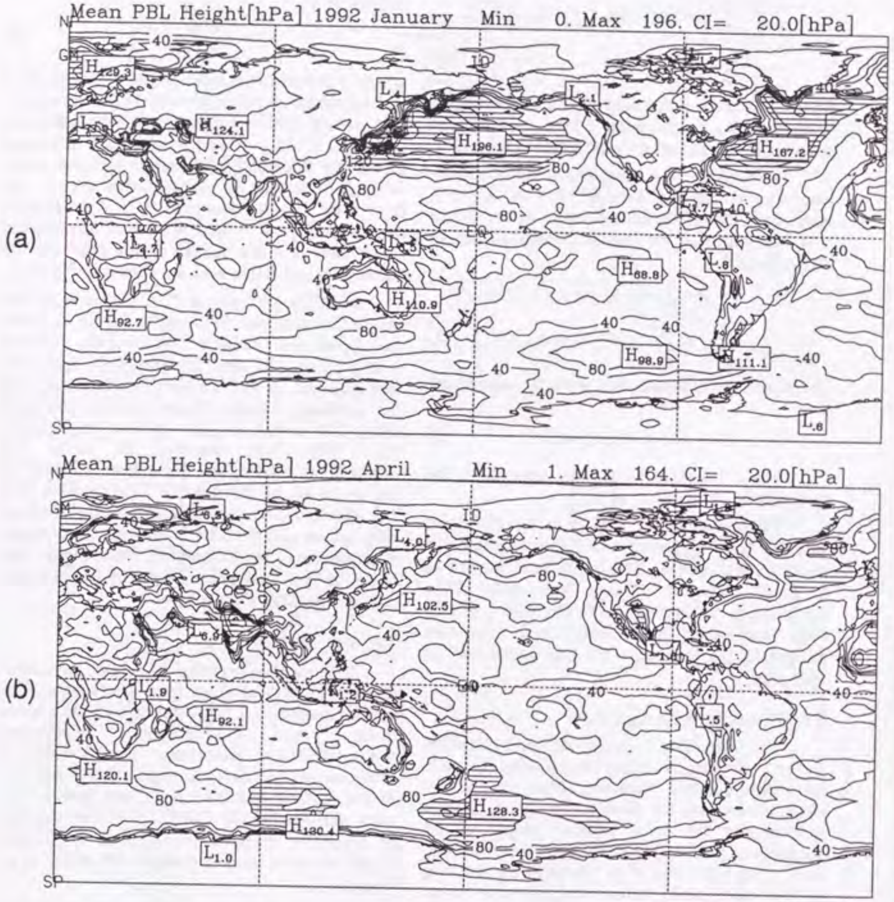

Fig.7 The thickness of the monthly mean planetary boundary layer for four month, (a) January, (b) March, (c) July and (d) October. The contour interval is 20 hPa and areas larger than 100 hPa are shaded.

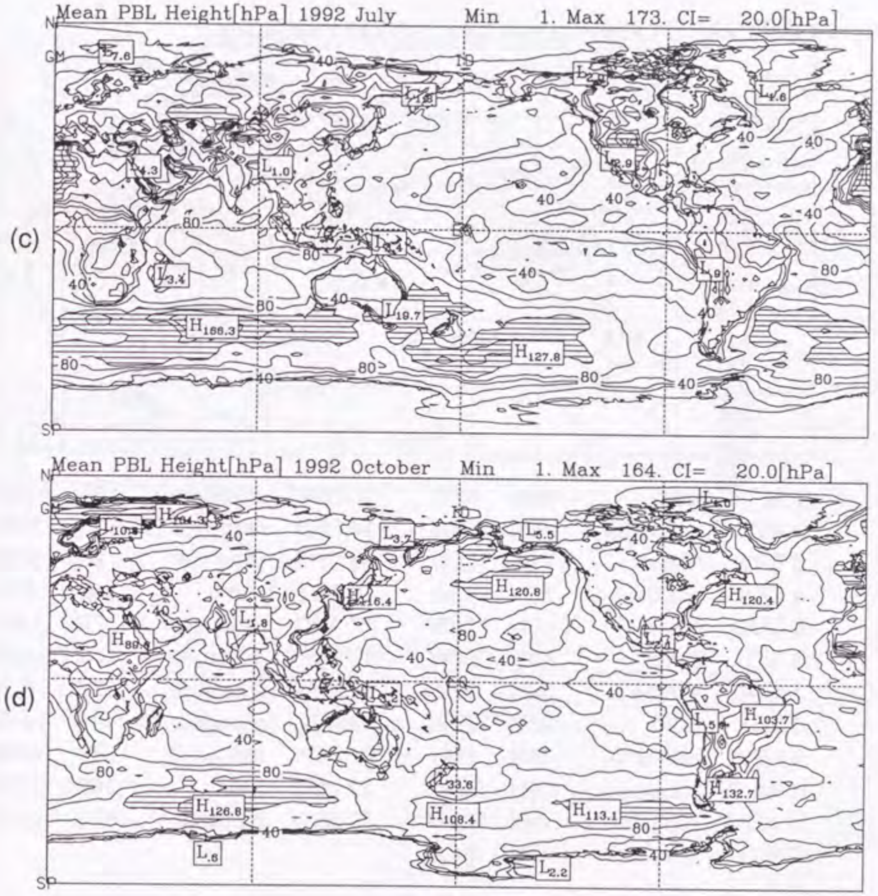

Fig.7 (continued)

CMDL/AES Observation site used in this study

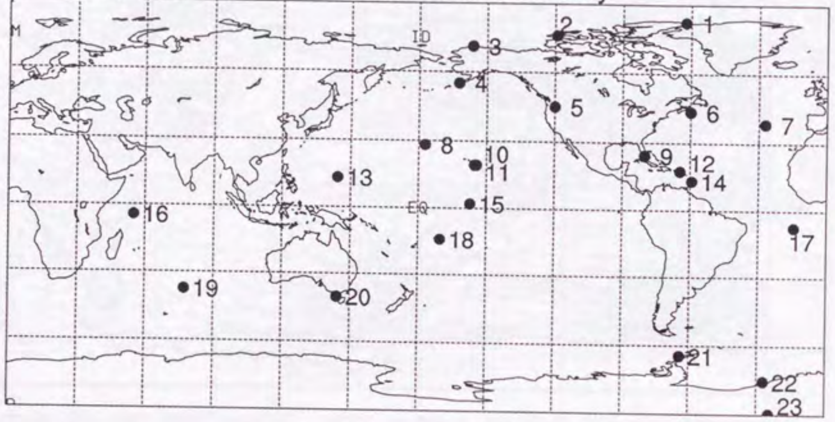

| | | | | | | | |
|---|---|---|---|---|---|---|---|
| 1 ALT | alert | 82N | 62W | 13 GMI | mariana | 13N | 144E |
| 2 BMC | mouldbay | 76N | 119W | 14 BRB | ragged | 13N | 59W |
| 3 BRW | barrow | 71N | 156W | 15 CHR | christma | 2N | 157W |
| 4 CBA | coldbay | 55N | 162W | 16 SEY | mahe | 4S | 55E |
| 5 CMO | meares | 45N | 120W | 17 ASC | ascensio | 7S | 14W |
| 6 SIC | sable | 43N | 60W | 18 SMO | matatula | 14S | 170W |
| 7 AZR | azores | 38N | 27W | 19 AMS | amsterda | 37S | 77E |
| 8 MID | sand | 28N | 177W | 20 CGO | capegrim | 40S | 144E |
| 9 KEY | biscayne | 24N | 80W | 21 PSA | palmer | 64S | 64W |
| 10 MLO | maunaloa | 19N | 155W | 22 HBA | halley | 75S | 27W |
| 11 KUM | kumukahi | 19N | 154W | 23 SPO | amundsen | 89S | 24W |
| 12 AVI | stcroix | 17N | 64W | | | | |

**Fig.8** Location of the sites for which atmospheric $CO_2$ records were used in this study.

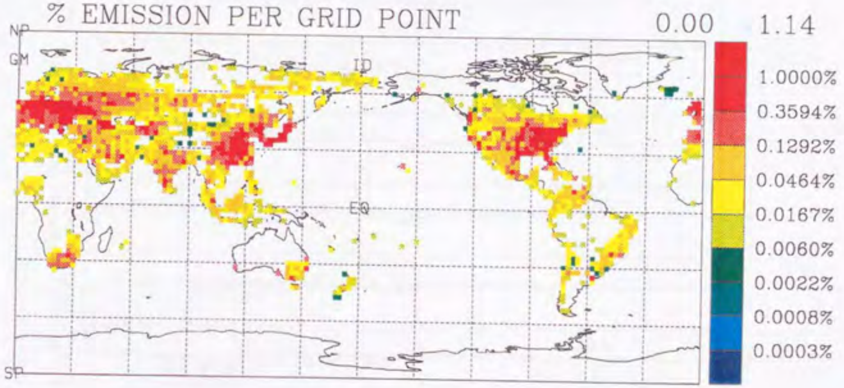

**Fig.9** Distribution of the emission of $CO_2$ produced by fossil fuel consumption in 2.5 degrees resolution. The distribution was created from the distribution given by TRANSCOM in 1x1 degree. The original value was estimated by Marland and modified by Fung et al..

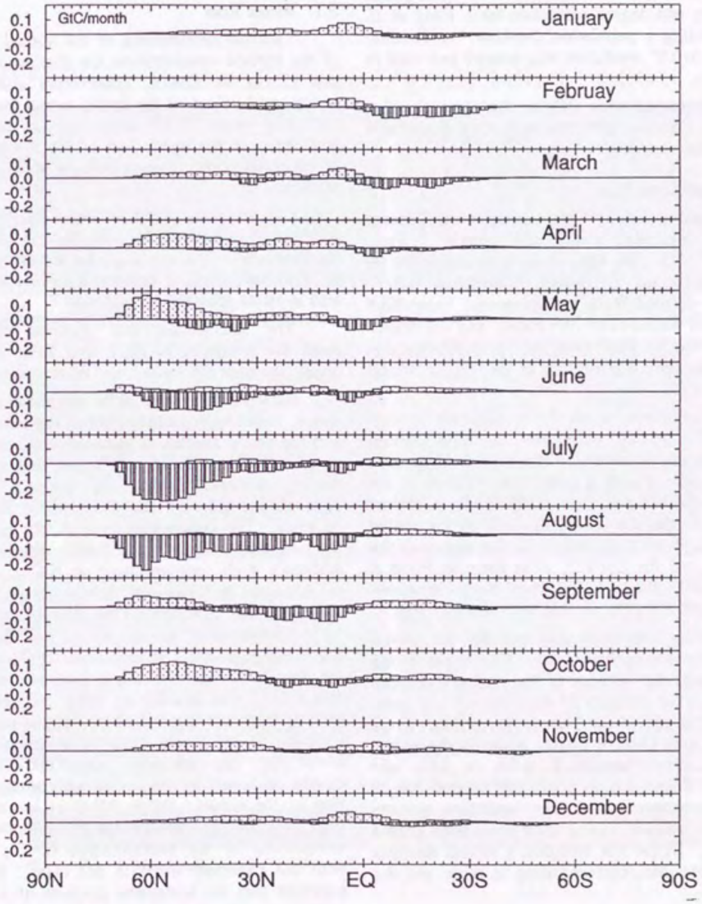

**Fig.10** Latitude distribution of sources and sinks of $CO_2$ produced by terrestrial biosphere in 2.5 degrees resolution. The distribution is created from the distribution given by TRANSCOM in 4x5 degrees, the unit used is GtC/month. The sources and sinks changed step-wise at the first day of each month.

### 2.7. Fossil Run

The fossil fuel experiment uses a source distribution (Fig.9) of carbon dioxide estimated from fossil fuel consumption. The original data were produced for each country by Marland (1982). The sources were distributed into the grid points at one by one degree resolution by I. Fung *et al.* (1987), using a population database. A distribution at 2.5*x*2.5° resolution was created and used in this study.

The source adds $CO_2$ to the atmosphere at the rate ot 5.3GtC per year, without seasonal and interannual variations.

### 2.8. Vegetation Run

Monthly 2.5*x*2.5° sources/sinks are created from the estimation at 4*x*5° resolution by I. Fung *et al.* (1987). The $CO_2$ sinks were estimated by the "Normalized Difference Vegetation Index" (NDVI), derived from the Advanced Very High Resolution Radiometer (AVHRR), and the source is estimated by land type use, precipitation and the atmospheric temperature of the GISS climate model.

Nevertheless, when the distribution is converted to a 2.5*x*2.5° resolution, the total sources and sinks are conserved. The annual integration of the source or sink is sometimes referred as the Growing Season Net Flux (GSNF). It is important to note that the GSNF depends on the spatial resolution of the distribution. If the sources/sinks are estimated for 2.5*x*2.5°, as is done by Fung *et al.* (1987), the GSNF may have increased because less $CO_2$ is canceled within a grid area.

Zonally integrated sources/sinks are shown for each month in Figure 10. The height of the bar indicates the strength of the source and depth of the bar, the strength of the sink. If one compares the height of the bars in the vertical direction, one may observe double peaks in the source in the northern middle latitudes in May and October. These double peaks are created due to the combination of a long emission periods (spring to autumn) and a short absorption period (summer). In the low latitudes, a simple seasonal cycle is obtained, corresponding to rainy and dry seasons.

Horizontal distributions of the sources/sinks are shown in Figure 11. The values show sources/sinks at each grid per six hours.

Siberia and Canada are assigned as a source region in May and sink region in June; from August to September, opposite changes are observed there. India is a source region in May and June, probably due to dry periods there.

## 3. Results

### 3.1. Fossil Run

Latitude distributions of the annual average of the surface concentration are displayed in Figure 12, at 23 CMDL observation sites. The nearby grid values of the model output for second and third years of the fossil run are shown in solid lines in the upper part of the figure. Each of the three years' observations are shown in dotted lines.

The temporal trend is larger in the model than the observed one, because there is no sink in the fossil run. The results of the second year will be discussed, mainly because the horizontal pattern is stable after the second year.

The inter-hemispheric gradient estimated from the averages at ALT and SPO is about 4ppm, for both the second and third years.

Between 20°N and 40°N, the mean concentration varies with latitude both in the observation and the model results. The concentrations at two stations, SIC and KEY, are higher than those of nearby stations. They are located at the downwind region of the $CO_2$ source in North America. The concentrations at AZR, located in the Atlantic Ocean, is lower than others. Although high concentrations at SIC and KEY are obtained in the model, low concentrations at AZR, are not obtained. This may be explained by the omission of an oceanic sink in the fossil run. Although MID is located in the middle of the Pacific Ocean, the mean concentrations are larger there than at KEY in 1988. The emission of $CO_2$ from the tropical ocean may explain this feature. At MLO, the observed concentration is lower than that calculated one. This difference can be explained by the use of surface concentration in the model. While MLO is located at a high altitude, the model level appropriate for comparison of the concentration of the model with the observed value is not clear. We can conclude that the horizontal gradient of the concentration at the down wind positions of America is reproduced in the model, because the difference between down wind regions and the other sites in nearby latitude is not inconsistent with the observed values, if AZR, MID and MLO are excluded.

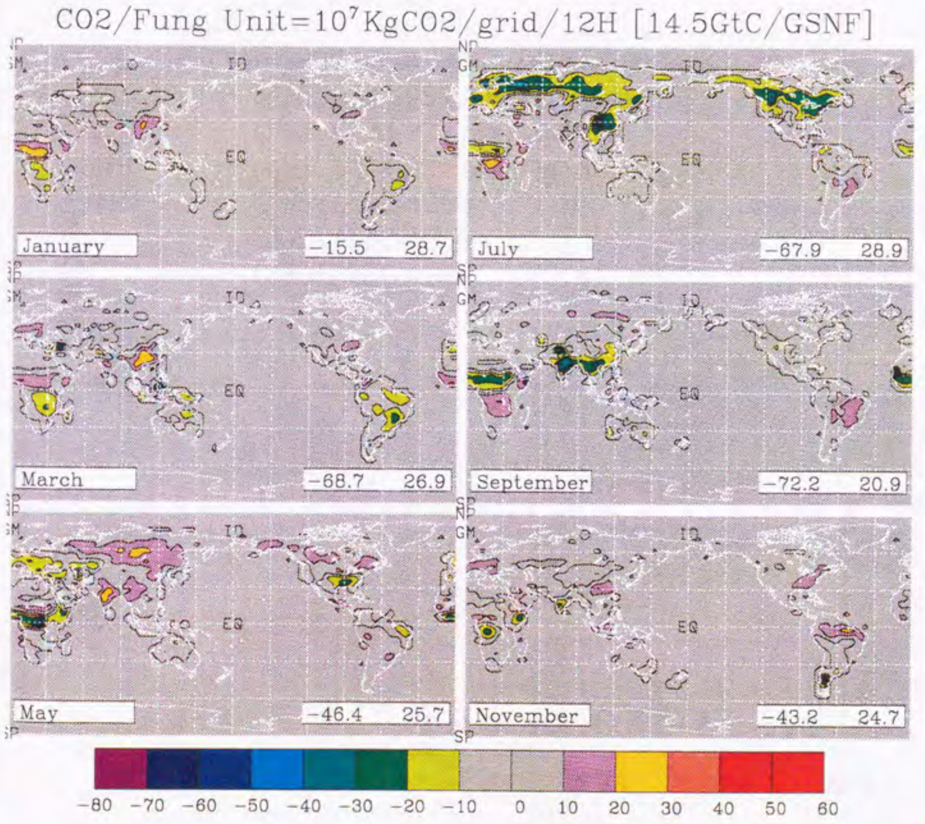

**Fig.11** Horizontal distribution of boundary flux

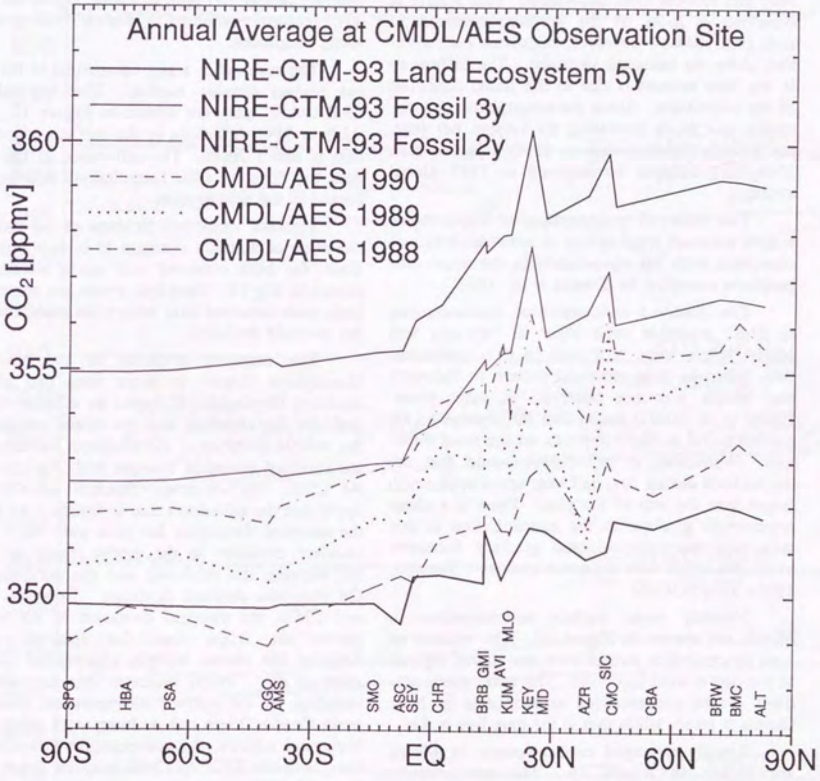

**Fig.12** Annual average concentration of $CO_2$ at observation sites. Three years of observation (88,89,90) and two years of simulation (2nd and 3rd) are shown.

Daily concentrations are compared with observations, in Figure 13, at four sites, (a) BRW, (b) MLO, (c) SMO (d) SPO. In each case, the observation site and the grid point of the model are indicated in latitude and longitude. Note that the scale of the vertical axis is different for each site.

Observed concentrations at BRW are stable during the spring and summer, but decrease in May and recover from September. This feature is observed at most of the northern hemispheric sites (not shown), however, calculated concentration show no seasonal variation. The difference in the base amount is due to the initial condition of the calculation. Since the atmospheric concentration of $CO_2$ is increasing by 1.4ppm per year, the average concentration in 1992 is higher than 350ppm ( 350ppm corresponds to 1987 global average).

The observed concentration at MLO shows a slow increase from spring to summer, which is consistent with the observation in the upper troposphere compiled by Tanaka *et al.* (1987).

The observed and calculated concentrations at SMO resemble each other in February and March where there is a peak in $CO_2$ concentration, however, this particular pattern in February and March was not observed in other years. Halter *et al.* (1987) found that the observed $CO_2$ concentration at SMO depends on the wind direction. Watterman *et al.* (1989) found that the fluctuations during first half year are always much larger than the rest of the year. There is a sharp north-south gradient in the concentration at this area, and this compositional gradient fluctuates north and south with time and seasons ( Taguchi, 1993).

Monthly mean surface concentrations in March are shown in Figure 14. The regions of high concentration extend from the source regions to the down wind locations. The north-south gradient of the concentration at Indonesia or New Guinia is steep, while that at the date line is flat.

Zonally averaged concentrations in March are shown in Figure 15. The concentration decreases with altitude in the Northern Hemisphere, while high concentration is observed in the middle of the troposphere. In the middle troposphere, concentration in the tropics is higher than in the sub-tropical regions, which may be explained by the convective activity in this area.

### 3.2. Vegetation run

Annual average and peak to peak amplitude of the vegetation run are shown in Figure 16. A simple explanation for the cause of this residual as an annual mean concentration has been already given in the Figure 1. Positive residuals are observed in China and northern Europe (a). Negative residuals are observed in South Africa and southern Europe. Peak to peak amplitude (b) reached almost 100 ppm in China. Over the oceans, seasonal variation is almost homogeneous along longitudes.

The residual is a key component in the global carbon dioxide burden. The residuals at CMDL/AES sites are shown in Figure 12. The ALE to SPO difference in the surface concentration is about 2ppm. The difference in the residual for different PBL formulations will be discussed in the next section.

Seasonal variations, in terms of the standard deviation of monthly averages at surface observations, for both observed and model results are shown in Fig.17. Temporal trends are subtracted from each observed data before the calculation of the standard deviation.

The standard deviation of the Northern Hemisphere (5ppm) is larger then that of the Southern Hemisphere (0.5ppm) by a factor of ten, both for the observed and the model results. In the middle latitudes of the Northern Hemisphere, the standard deviation changes with the latitudes. At CMO, the observed standard deviation is 3ppm but the calculated one is 4ppmv. At AZR, the standard deviations for each year vary. The standard deviation in the model results at AZR fell between the minimum and the maximum of the observed standard deviation. Between KEY and CMO, the standard deviation of the model results are larger than the observed ones. Because the recent isotopic observation (Nakazawa *et al.* , 1993) indicates that the seasonal variation in the surface concentration over the north Pacific Ocean can be interpreted using only biological activity, the sources/sinks effective for sites between KEY to CMO may be larger than those of the land ecosystems.

Daily concentrations are compared in Fig. 18. At BRW, the calculated concentration is about 10ppmv lower than observed values, except from May to July, which may be due to the seasonal variation of the sources and sinks, as shown in Fig.10 and 11. Calculated concentration from May and July are also higher than that in April in

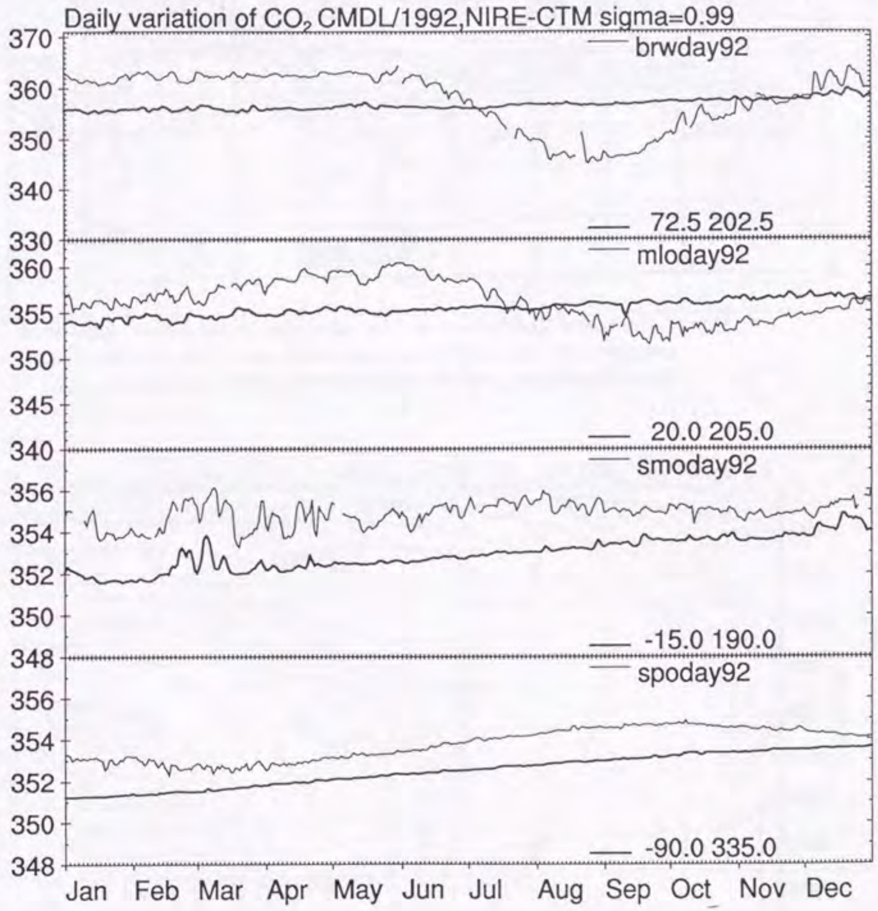

**Fig.13** Daily variations of $CO_2$ at CMDL sites in 1992 and the second model year. (a) Point Barrow, (b) Mauna Loa, (c) Matatula, (d) Amundsen Scott.

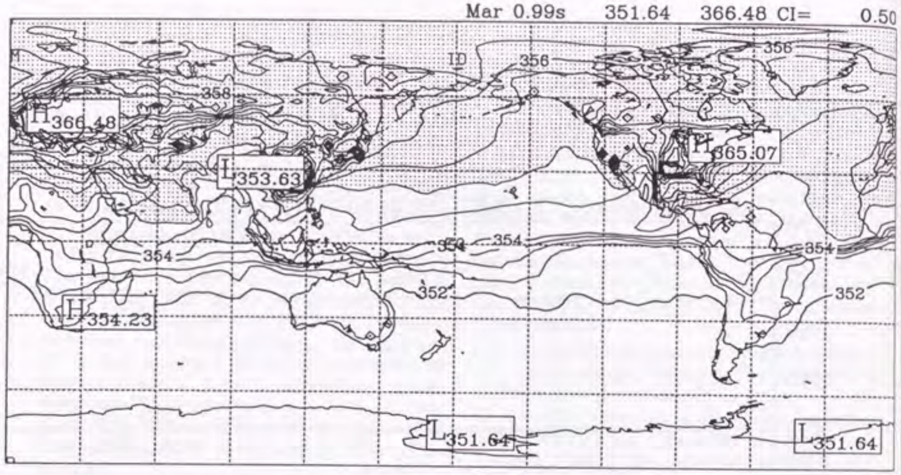

**Fig.14** Horizontal distribution of $CO_2$ calculated at the lowest sigma level averaged over March of the second model year. Concentrations larger than 355ppmv are shaded and the contour interval is 0.5ppmv.

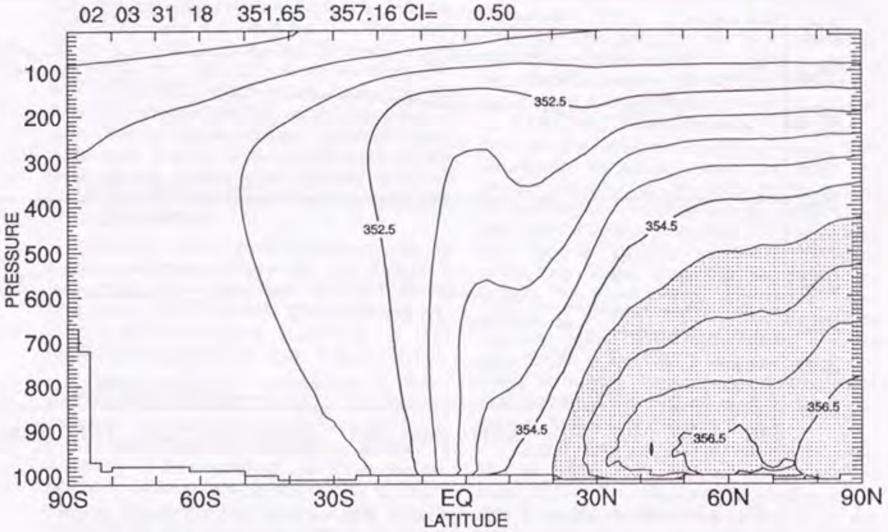

**Fig.15** Monthly mean concentration in latitude vertical cross section averaged at each sigma level in March of the second model year. The contour interval is 0.5ppmv.

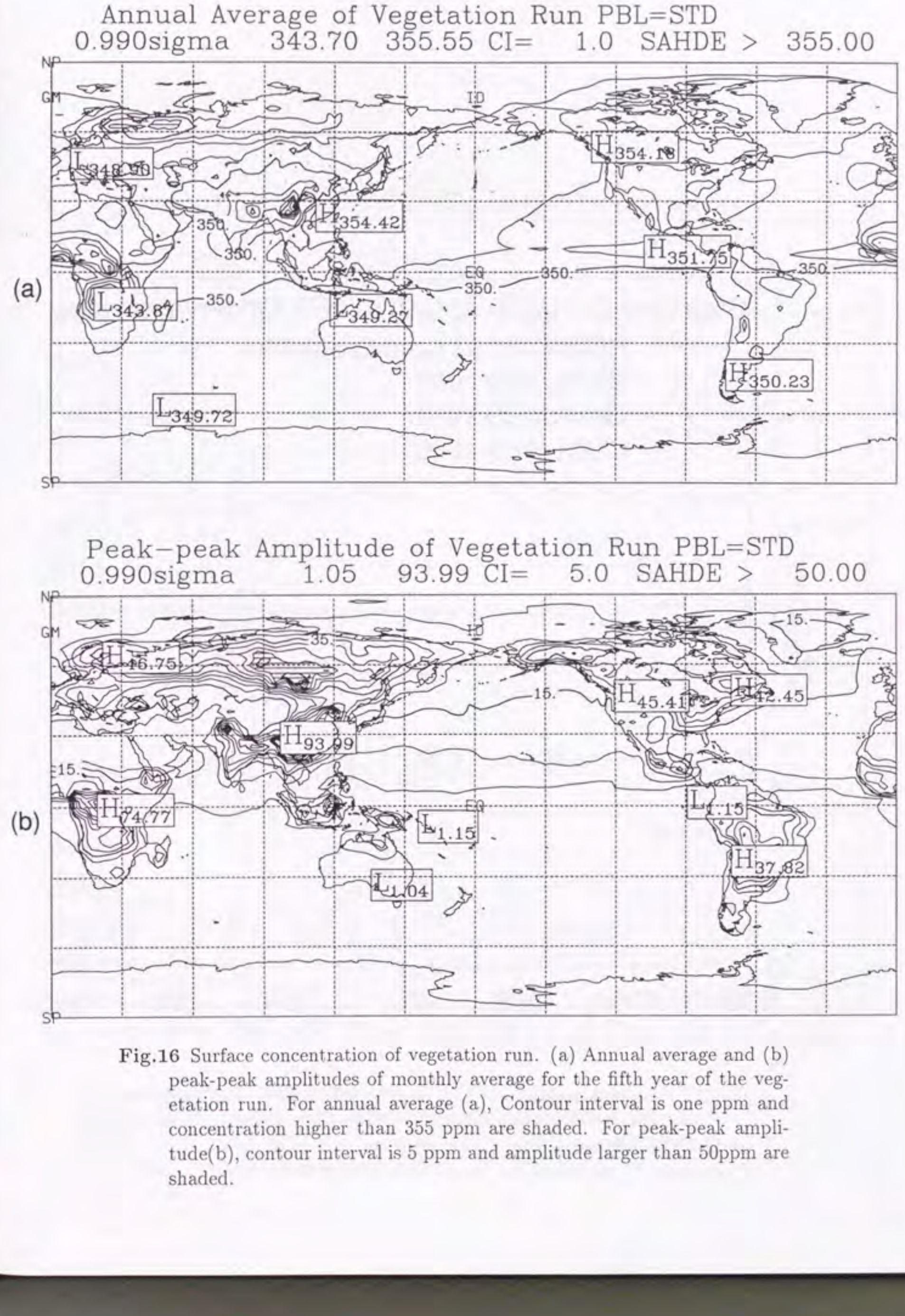

**Fig.16** Surface concentration of vegetation run. (a) Annual average and (b) peak-peak amplitudes of monthly average for the fifth year of the vegetation run. For annual average (a), Contour interval is one ppm and concentration higher than 355 ppm are shaded. For peak-peak amplitude(b), contour interval is 5 ppm and amplitude larger than 50ppm are shaded.

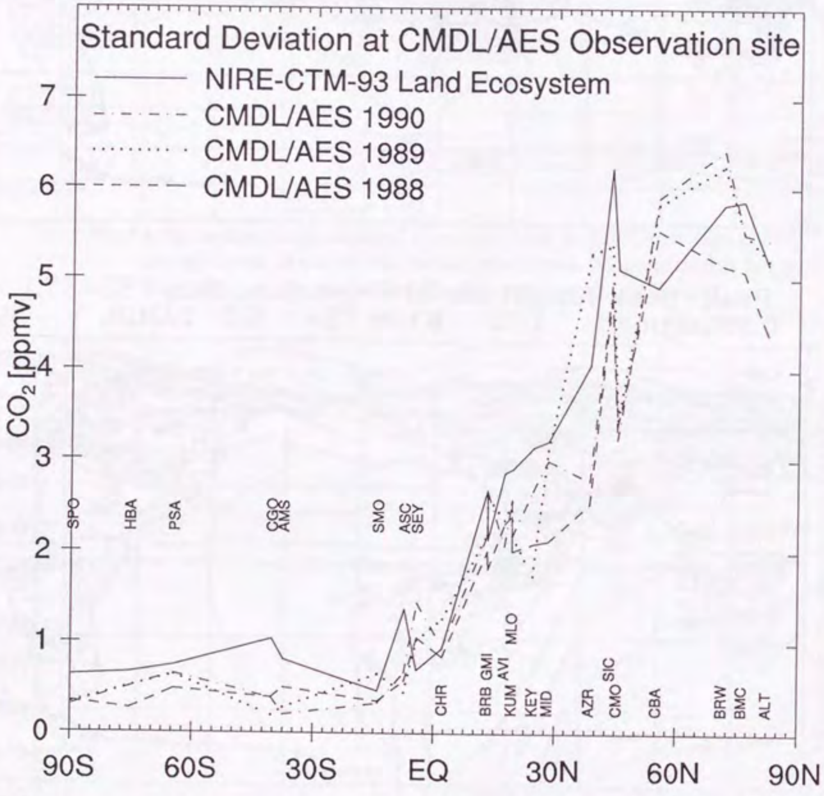

Fig.17 Standard deviation of $CO_2$ at observation sites. The temporal trend is subtracted from the observation before the calculation of the standard deviation.

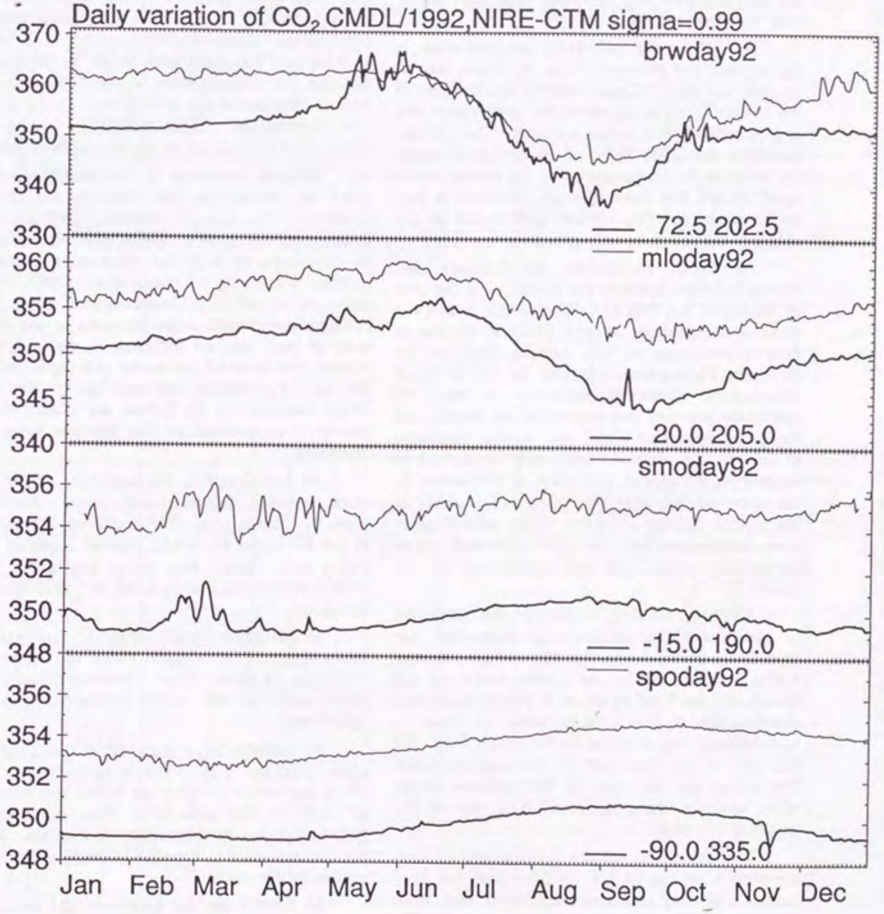

Fig.18 Daily variation of $CO_2$ produced by terrestrial biosphere at CMDL sites. (a) Point Barrow, (b) Mauna Loa, (c) Matatula, (d) Amundsen Scott.

other sites listed in Fig.8 in the Northern Hemisphere (not shown).

Daily variations at BRW in July and October resemble some feature of the observed fluctuations. These fluctuations can be explained by the horizontal and temporal variations associated with the land ecosystem.

At MLO, the calculated concentration is higher than the observed value by 5ppm, except in June and July. Concentrations are sampled at the lowest sigma level, while the observation site is located at 3397m above sea level. The concentration in the upper layer of the model is almost the same as the concentration in the lowest sigma level, except that there is small reduction in seasonal variation. The vertical distribution of the seasonal variations is discussed later.

At SMO, fluctuations in February and March are reproduced in the model, as is the case of the fossil run (Fig.13). The reason is that the north-south gradient around SMO is similar in both experiments at this season; high in the Northern Hemisphere and low in the Southern Hemisphere. Seasonal variations in terms of amplitude are well reproduced in the model, but the phase is shifted about one month; maximum at July in the observed case may be shifted to August in the model, minimum at November in the observed case may be shifted to December in the model. In the observed value, several short term fluctuations may be associated with ocean interaction, which are not reproduced in the model.

At SPO, seasonal variations, the minimum in March and the maximum in September, are reproduced in the model. In November, one may notice a sharp dip in the concentration of the model. In the time series of 6 hourly horizontal distributions, a low concentration air mass is tracked from the Amazon to the South Pole, but this dip is not observed in the measurements. The reason for this may be the problem in the wind analysis there, however, it is out of the scope of this study.

The calculated surface distributions of $CO_2$ are shown in Fig.19 for (a) May and (b) September. In May, the concentration is high over Siberia and Canada, where the source of $CO_2$ extends. In the Southern Hemisphere, the mean concentration is only 0.5ppmv lower than the initial value, except in the Amazon, where a large sink is located. In September, the concentration in the Northern Hemisphere is lower than that in the Southern Hemisphere, while the concentration in the Southern Hemisphere is still higher than the initial condition, but only by 0.7 ppm.

The zonal average of the concentration is shown in Fig.20 for May(a) and September (b). The north-south gradient of the concentration is reversed during these two months throughout the troposphere. Concentration decreases with height in May and increases with height in September, because the concentration in the stratosphere is almost constant in this experiment. In the Southern Hemisphere, concentration variations are transmitted through the upper troposphere.

Seasonal variations of the vertical distribution are shown for six sites in Fig.21; (a) Anchorage, (b) Japan, (c)Mariana, (d) Rabaul, (e) Sydney and (f) Syowa. These sites were selected to be compared with the observation made by Tohoku University ( Tanaka *et al.* 1987, Nakazawa *et al.* 1991). Concentrations lower than 350ppm are shaded, while the latitude and longitude of each site are indicated in the upper left corner, and those of the model grid are written in the second parentheses of each figure. The sites of (c) Mariana and (d) Rabaul, are located on the course of commercial air line between Japan and Australia.

At Anchorage(a), the amplitude of the seasonal variation decreases with height. Measurement by Tanaka *et al.* (1987) showed 10ppm(p-p) at 7.5 km while the model showed 8ppm at 0.35 sigma level (about 8km above sea level). The observed maximum is in May, but it is June in the model.

At the Japan site(b), observed amplitude at the tropopause is 10ppm while the calculated amplitude is about 7ppm. Minimum and maximum occur at the month consistent with the observation.

At Mariana (c), a sharp dip at 0.275 sigma ( about 10,000m ) in April is remarkable. This sharp depression is observed in the measurement of 1985 at 5°N and 10°N. The minimum is observed either in September or October, while the concentration in October is smaller than September in the model.

At Rabaul (d), the maximum and minimum are observed in the upper troposphere. The maximum in July and minimum in October correspond with the maximum and minimum in the Northern Hemisphere. The concentration in the lower troposphere is low in March. At least two factors are related to this low concentration;

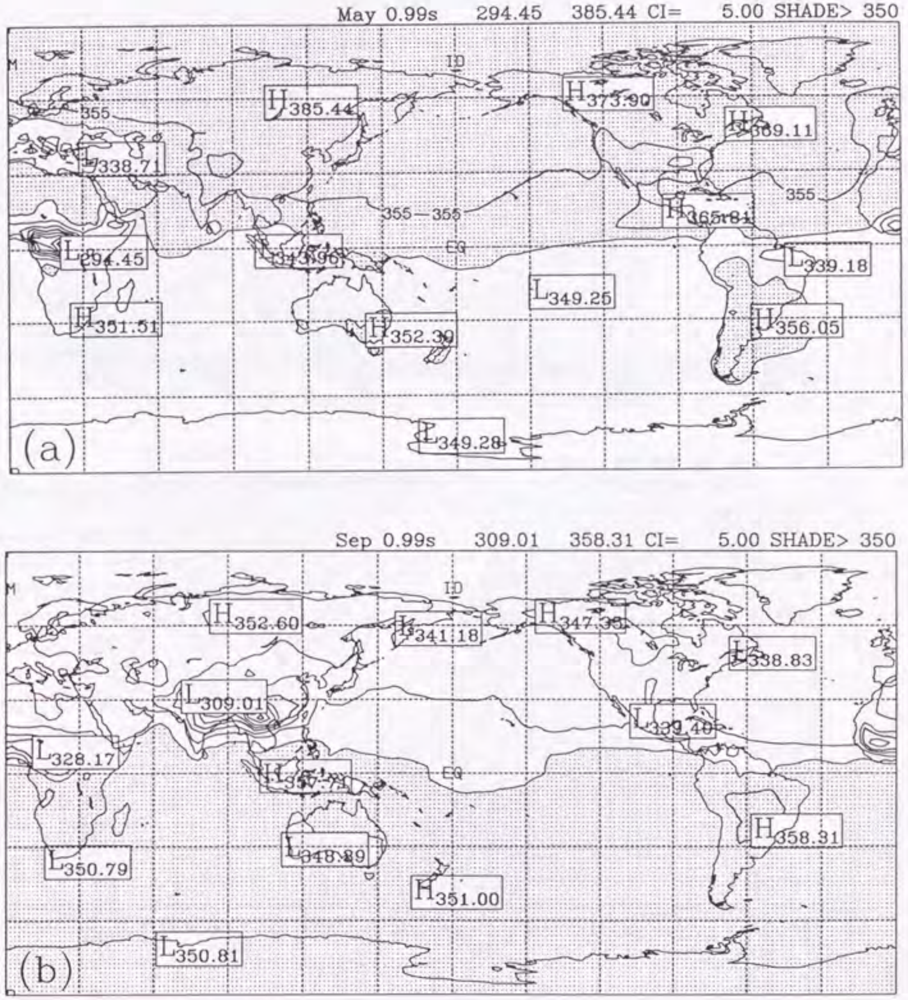

**Fig.19** Horizontal distribution at the lowest sigma level in May (a) and September (b) of $CO_2$ concentrations (ppm), as simulated in the model. The contour interval is 5ppm. Concentrations higher than 350ppmv are shaded.

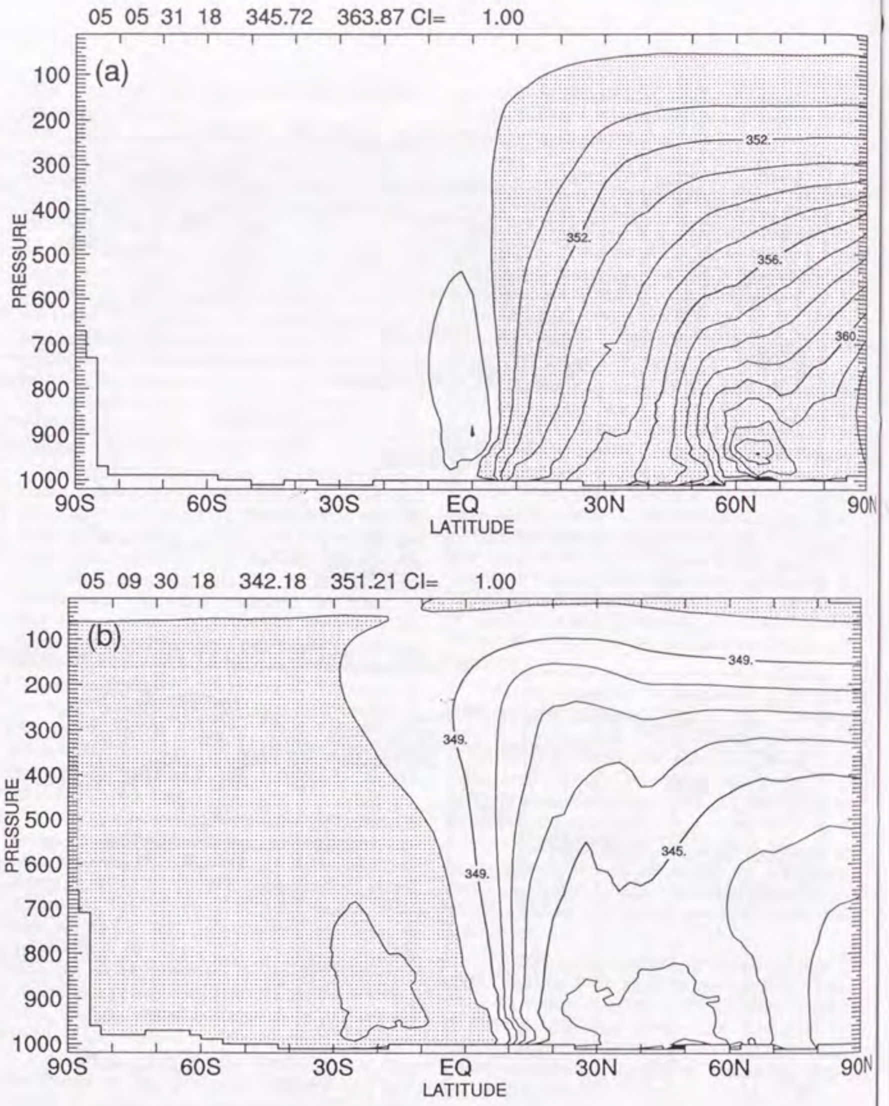

**Fig.20** Monthly mean concentration in latitude-vertical cross section averaged at each sigma level in May (a) and September (b). The contour interval is 0.5ppm.

(a) Anchorage

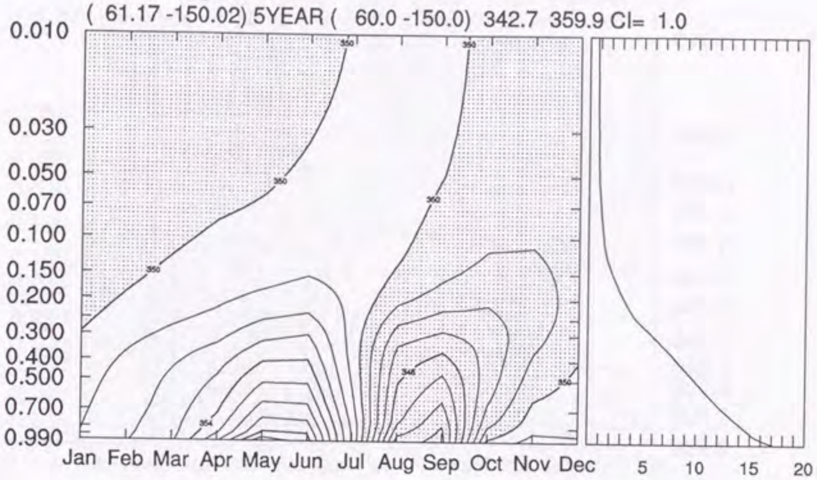

(b) Japan

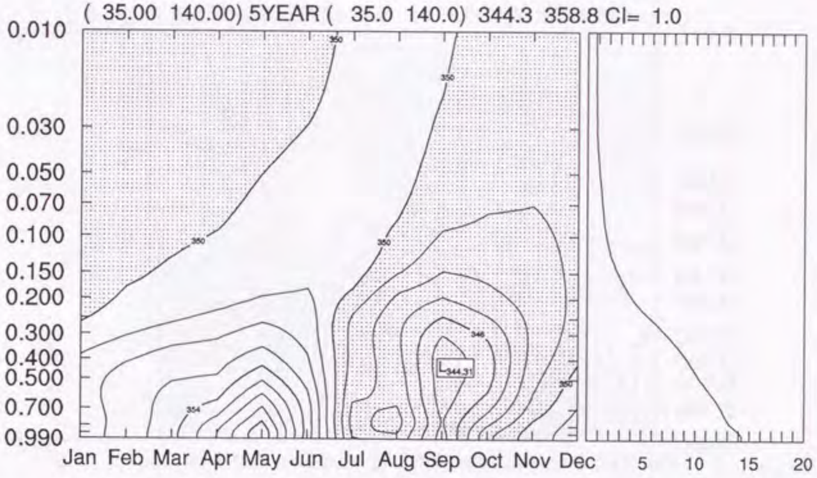

**Fig.21** Seasonal variation of the vertical concentration distribution. (a) Anchorage, (b) Japan, (c) Mariana, (d) Rabaul, (e) Sydney and (f) Syowa. Areas less than 350ppmv are shaded. Contour interval is 1.0ppmv for (a) and (b), 0.5ppmv for (c), 0.2ppmv for (d) and (e), 0.1ppmv for (f), respectively.

(c) Mariana

( 13.43 144.78) 5YEAR ( 12.5 145.0) 346.9 354.8 CI= 0.5

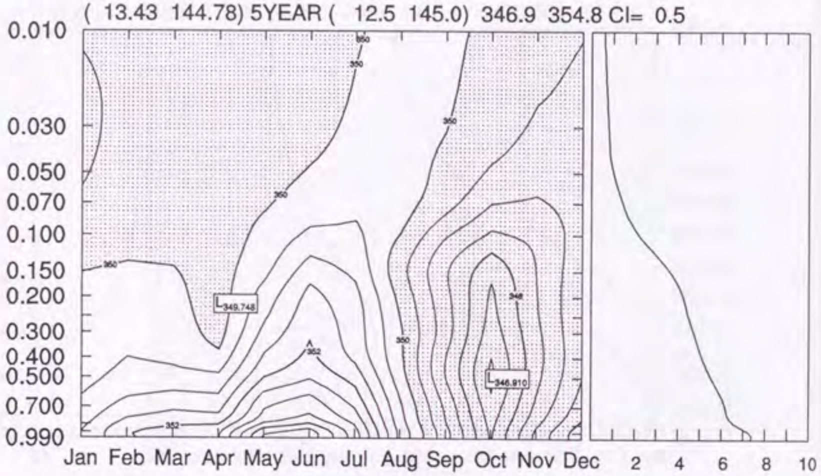

(d) Rabaul

( -4.22 152.18) 5YEAR ( -5.0 152.5) 348.3 351.2 CI= 0.2

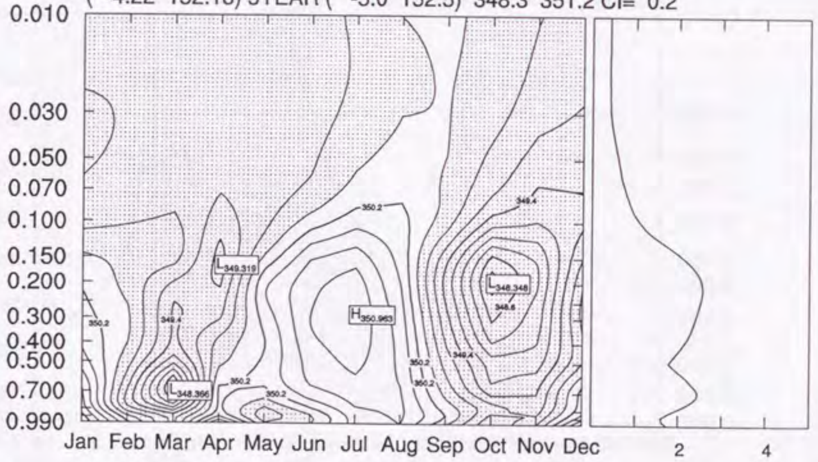

Fig.21 (continued)

(e) Sydney

( -33.87 151.20) 5YEAR ( -35.0 150.0) 348.2 351.2 CI= 0.2

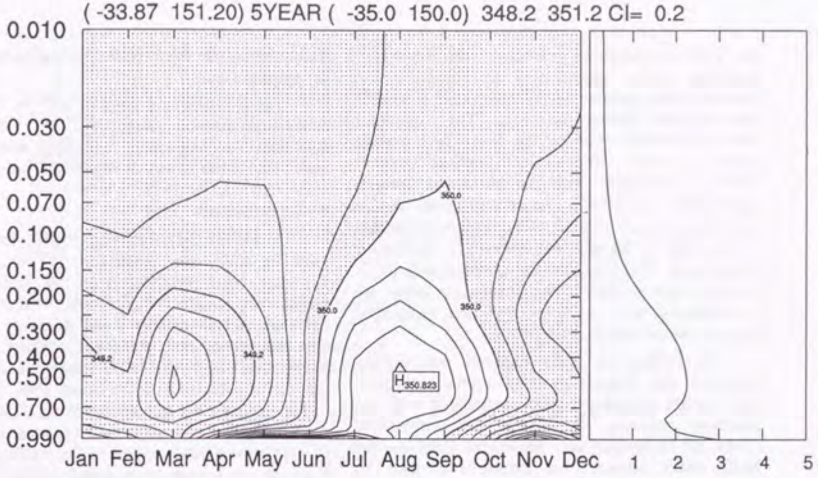

(f) Syowa

( -69.00 39.58) 5YEAR ( -70.0 40.0) 349.0 350.8 CI= 0.1

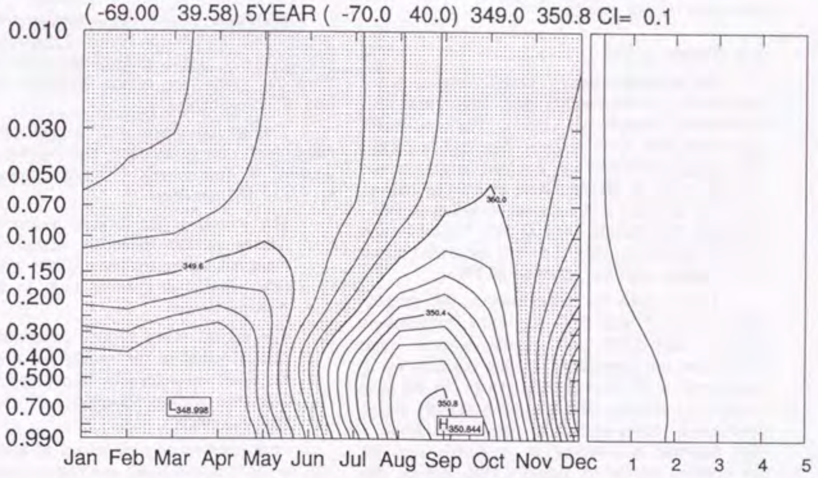

Fig.21 (continued)

one is the convergence associated with the winter monsoon in this period and the second is the enhanced sink, related to the precipitation associated with the winter monsoon. The first point can be observed even in the fossil fuel experiment. A steep compositional gradient zone at 150°E is associated with the horizontal convergence there. (Fig.14). The second factor can be seen from Fig.10 and 11. The horizontal pattern of the sink in March (not shown) is similar to that in May (Fig.11a), but the absorption strength is larger than in May. The observed minima are in February and in June, but the calculated minima are in January and in June.

At Sydney (e), the maxima occurred in February and August at 0.35 sigma and these maxima are considered to be associated with the observed maxima, in March and September (1984) or in January and September (1985). The phase delay between the lowest level and the lower troposphere is about four months.

At Syowa (f), the lowest tropospheric concentration lags the upper level concentration in the model by one month.

### 3.3. Effects of PBL

The simulated pole to pole difference in the vegetation run was eight times larger than that obtained by Tans *et al.* (1990). We have tested four additional formulations: Monthly averaged PBL heights (Month) and doubled heights of the monthly value (2xMonth) were studied to address the effect of daily and seasonal variation of PBL. Constant PBL height of 100 hPa (100hPa) and lowest sigma level only (Lowest) were also tested to investigate regional variation of PBL.

Table 1 lists the differences in the concentration at ALT and SPO for these formulations for both the fossil and vegetation runs. The differences are normalized against the case using instantaneous PBL height (Standard). In the case of monthly average PBL height, a slightly larger contrasts is observed in the fossil run, while a 40% increase is observed in vegetation run. In the doubled height of monthly PBL values, the contrast is decreased by 10% in fossil run and 22% in the vegetation run. These results are consistent with the increase in the vertical diffusion rate in the doubled PBL heights.

If only the lowest sigma level is used for PBL, the contrast becomes larger than that obtained for the monthly averaged PBL case. If 100hPa thickness is used for PBL, the contrast becomes smaller than standard case, especially for the vegetation run.

These differences suggest that the traditional calibration method using CFC or _$^{85}$Kr is not sufficient for seasonally changing sources and sinks, like those found in vegetation runs.

### 4. Conclusions

A global 3-D transport model model was used to study the sensitivity of the planetary boundary layer formulation on the global atmospheric $CO_2$ burden. Two sources and sinks used by Tans *et al.* (1990) were adopted: a source only run (fossil run) and a sources and sinks run (vegetation run). The main results of this study are that the North Pole to South Pole difference in the surface concentration is about 6 ppm, when the source from fossil fuel and sources and sinks of land ecosystem are used in the NIRE-CTM-93. Because the observed contrast is 4ppm in the annual average, this result indicates that the so-called missing sink should be found in the Northern Hemisphere.

Although, further evaluation of the source strength and distribution is out of the scope of the present study, some conjectures were obtained from the comparison of the observed concentration of atmospheric $CO_2$.

The annual mean surface concentration in fossil fuel run reproduced the interhemispheric gradient of atmospheric $CO_2$, nevertheless there are some discrepancies.

1. The annual mean surface concentration at Azores in the model is higher than the observed value, by about 50%, which indicates significant oceanic sinks in the north Atlantic Ocean.
2. The annual mean surface concentrations at tropical sites in the model are lower than the observed values by about 1ppm, which indicates surface emission of $CO_2$ from tropical oceans.

Daily surface concentrations of atmospheric $CO_2$ in 1992 in the fossil run and vegetation run were compared at four observation sites of CMDL.

1. Amplitudes and phase of fluctuations in the time scale of few days are reproduced in the model at BRW and MLO, which indicate that these short term fluctuations are produced by synoptic scale disturbances passing over a land ecosystem.

2. A short term high concentration at SMO from February to March was reproduced in both in the fossil and vegetation runs, which indicates that the fluctuation is produced by temporal fluctuation of the north to south gradient in the surface concentration.
3. Fluctuations observed at SMO with a time scale of few days are not contained in the model concentration, which indicates that these fluctuations are produced by oceanic sources and sinks.
4. The model produced a seasonal cycle at SMO that is not detected in the observation, which indicates the sources and sinks with seasonal variation are located over the tropical ocean.

The difference in the annual mean surface concentration between ALT to SPO was used to investigate the sensitivity of the PBL formulations

1. The difference in the fossil run was about 4ppm for the standard run. It was rather insensitive to the modifications of PBL formulation.
2. The difference in the vegetation run was about 2ppm for standard run, and was altered with the change in PBL formulations.
3. Monthly averaged PBL heights can be used instead of instantaneous PBL within a limited purpose if they are scaled by an appropriate factor.

# Capter 5: Application of a chemical transport model (2): Methyl chloroform and Methane

## Abstract

A global tracer transport model was developed incorporating semi-Lagrangian transport with a mass fixer and non-local diffusion in the planetary boundary layer. The time evolution of methyl chloroform ($CH_3CCl_3$) and methane ($CH_4$) were calculated with 2.5° horizontal resolution at 15 vertical sigma levels four times per day. One year of meteorological data for 1992 provided four times per day from the European Center for Medium Range Weather Forecasts (ECMWF) was used to calculate the back trajectories and height of the planetary boundary layer.

The inter-hemispheric exchange time was calculated as 0.86 years for the northern hemisphere and 1.08 years for the southern hemisphere based on the time evolution of an artificial material.

Time evolution of methyl chloroform was calculated from an initial concentration value of 110pptv in the northern hemisphere and 70pptv in the southern hemisphere with source estimates based on electric power consumption and industrial reports. Removal by hydroxyl radical was calculated explicitly. The global average hydroxyl radical concentration deduced to get a $380x\,10^9 g$ sink of methyl chloroform was $4.7x\,10^5 (molecules/cm^3)$. The seasonal variation of methyl chloroform is compatible with ALE/GAGE data.

The time evolution of the methane source to the atmosphere was calculated using source estimates based on net primary productivity and fossil fuel consumption. Global removal of methane through reaction with the hydroxyl radical was 463Tg/yr for an initial homogeneous distribution of methane of 1600 ppbv. The source of methane was 524 Tg per year. This combination resulted in a 40Tg (15 ppbv) increase in atmospheric methane per year, which is compatible with CMDL data in the 1980's.

## 1. Introduction

Methane plays an important role in the earth's radiation budget and the chemistry of the atmosphere. Both the estimates of the source of methane to the atmosphere and the rate of removal have large uncertainties.

The hydroxyl radical (OH) is the most important factor for the removal of methane in the troposphere. The estimate of the global hydroxyl radical concentration has been changing with the accumulation of observations and with each change in the atmospheric transport model used for the evaluation. Volz *et al.* (1981) estimated the global average OH concentration as $6.5x\,10^5 molecules/cm^3$ based on the analysis of atmospheric carbon monoxide. Prinn *et al.* (1983) obtained an estimate of $5.0x\,10^5 molecules/cm^3$ based on the three year methyl chloroform data obtained by the Atmospheric Life Time Experiment (ALE) in combination with a nine box atmospheric model. Prinn *et al.* (1987) recalculated the hydroxyl radical concentration as $7.7x\,10^5 molecules/cm^3$ based on 7 years of ALE and Global Gases Experiment (GAGE) data. Prinn *et al.* (1992) obtained $8.7x\,10^5 molecules/cm^3$ based on 12 years of ALE/GAGE data. Spivakovsky *et al.* (1990) obtained an estimate of $7.7x\,10^5 molecules/cm^3$ using a three dimensional global tracer transport model. Taylor *et al.* (1991) obtained a value of $6.37x\,10^5 molecules/cm^3$ based on ALE/GAGE data using a 2.5° resolution three dimensional Lagrangian transport model. In the above studies, exept Spivakovsky *et al.* (1990), it is assumed that OH is homogeneous with longitude. The diurnal variation of OH was also ignored. Thus, the estimate of OH represents the amount needed to reproduce the observed concentration of methyl chloroform in the atmosphere. In the present study we have made the same assumptions.

The amount of methane has been observed and archived by CMDL. Taylor *et al.* (1991) simulated the three dimensional distribution of methane using an OH concentration adjusted to match the required sink for methyl chloroform in a global Lagrangian tracer transport model. Fung *et al.* (1991) simulated the methane distribution using the GISS tracer transport model using a three dimensional OH field. The objective of this paper is to estimate the OH concentration and to evaluate the source strength of methane for the global tracer transport model developed at the National Institute for Resources and Environment.

## 2. NIRE-CTM-93

The details of the model were written in the previous chapter. Figure 1 shows the flow of the data. The meteorological data analyzed at the ECMWF (TOGA/Advanced) was used to estimate the reaction rate in addition to the transport and convection of minor constituents. The vertical resolution of the concentration is 15 sigma levels extending from 0.975 to 0.02 which is different from the model used in the previous chapter. The results are insensitive to this difference.

## 3. Artificial tracer transport and the interhemispheric exchange time

To demonstrate the mass fixer and to calculate the interhemispheric exchange time a one year simulation of the evolution of an artificial tracer was investigated. Tracer was initially distributed across the globe with a linear gradient from the south pole to the north pole. The initial amount was homogeneous with respect to longitude and height. Figure 2 shows the latitudinal distribution of the monthly, vertically and zonally averaged mixing ratio of the artificial tracer.

Figure 3 shows the boundary of the hemispheric air masses and the fluxes between hemispheres. The definitions and procedures used to estimate the flux are the same as Taguchi (1993) and this figure corresponds to Fig.7(a). Although the year and time interval of the meteorological data are different in this study ( 1992, 6 hours ) than that of Taguchi (1993) (1989, 12 hours ), the position of the boundary and the magnitude of the flux are almost the same. The interhemispheric exchange time is estimated to be 0.86 years for the northern hemisphere and 1.08 years for the southern hemisphere. The difference is due to the mean location of the boundary separating both hemispheres.

## 4. Methyl Chloroform

Figure 4 shows the source distribution estimated by Hartley *et al.* (1993). The amount was interpolated linearly onto a 2.5° horizontal grid from the original data by Mulquiney ( Personal communication ). The interannual variation of the total emission is the same as listed in Table 4 of Prinn *et al.* (1992;. The emission of methyl chloroform from 1979 to 1989 ; 546 544 518 579 587 596 617 659 701 $x10^9 g$). Time variation of the source distribution was not included.

The reaction coefficient for the $OH+CH_3CCl_3$ reaction was obtained from DeMore *et al.* (1992). This reaction rate was used in conjunction with the zonally homogeneous hydroxyl radical concentration provided by Spivakovsky (Fig.5) and the ECMWF temperature data. A global average of OH of 4.7 $molecules/cm^3$ was required to obtain a 380 x $10^9 g/yr$ removal rate for $CH_3CCl_3$ at an average $CH_3CCl_3$ concentration of 100 pptv. This value yields a 7.56 ppt/yr increase in the globally averaged $CH_3CCl_3$ concentration.

Figure 6 shows a comparison between methyl chloroform concentrations observed at monitoring sites in the ALE/GAGE network and those simulated and sampled at a point near to the observation site.

The seasonal variation in $CH_3CCl_3$ at Oregon(b) and Tasmania (c) is well reproduced in the model. The time variation at Ireland (a) is larger than is observed, probably because of the removal of "pollution" events from the observational records.

Inter-annual variation of concentrations almost coincide with observations in early the 80's, but is larger than observed in the late 80's. If the emission amount is correct, the OH concentration may have increased in the late 80's as was suggested by Prinn *et al.* (1992).

The base amount is smaller than observed only at Oregon (b). Figure 7 shows the horizontal distribution of $CH_3CCl_3$ at the lowest sigma level averaged over the second year in August. The horizontal gradient is largest at Oregon among ALE/GAGE sites. The base amount is sensitive to the selection of the grid point used for comparison at Oregon.

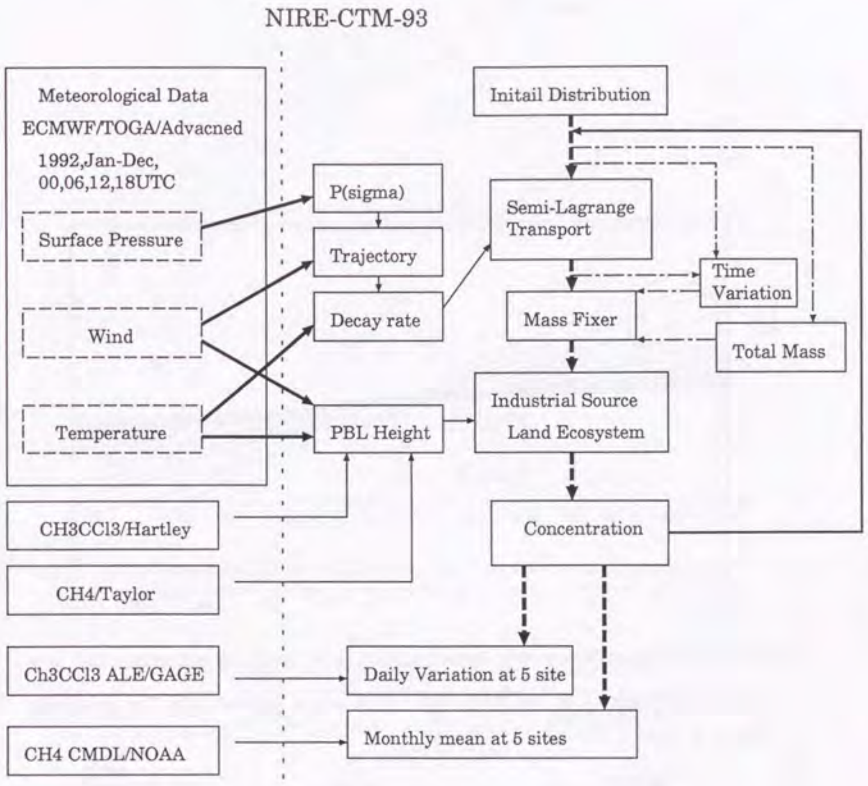

Fig.1:Model flow and experimental design of NIRE-CTM-93 for Methane and Methyl Chloroform.

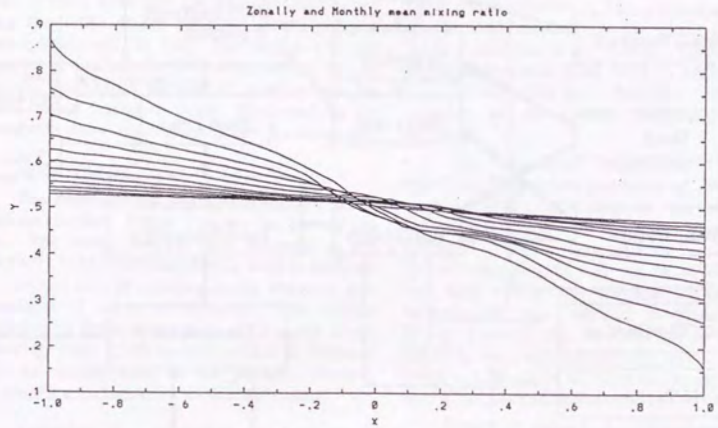

Fig.2:Time evolution of mixing ratio. Initially uniform in the zonal and vertical directions with a linear distribution from one at the north pole to zero at the south pole. The unit is arbitrary.

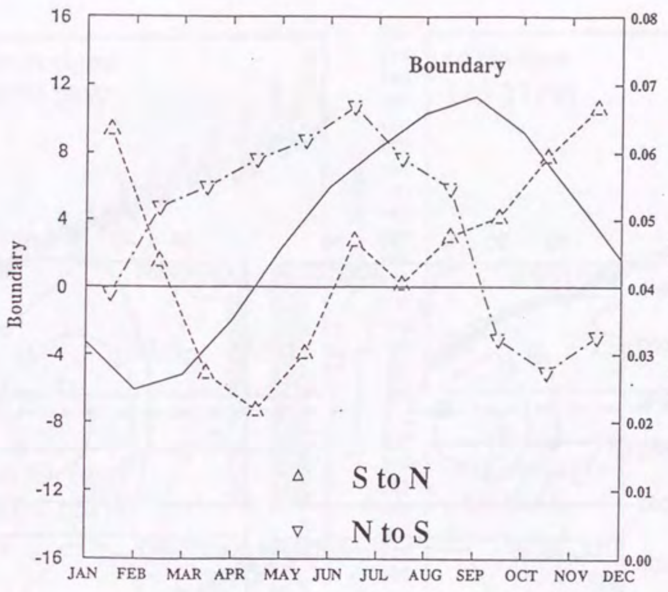

Fig.3:The position of the boundary and flux from north to south and *vice-versa*.

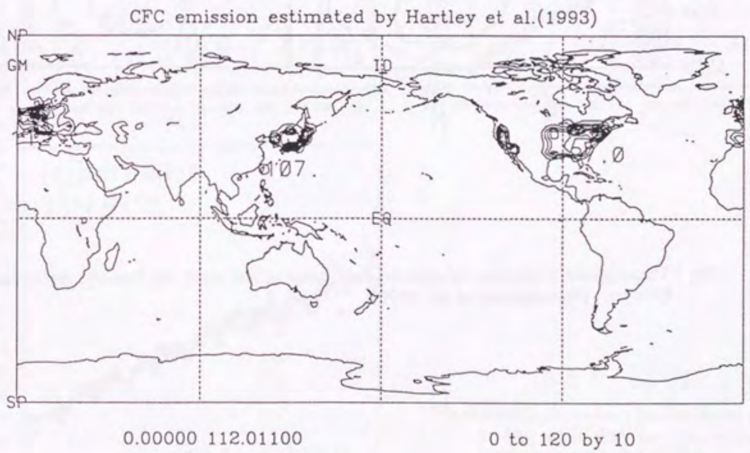

Fig.4:A source distribution estimated by Hartly *et al.* (1993) and interpolated by Mulquiney (personal communication).

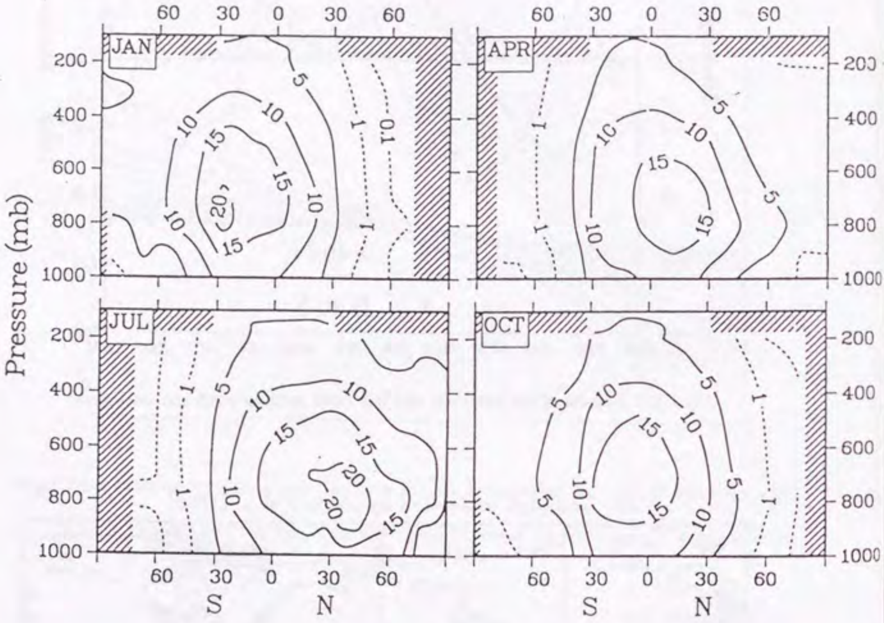

Fig.5:Tropospheric OH(units: $10^5 molecules/cm^3$) used in this study for January, April, July, and October. (Spivakosfsky *et al.* 1990.).

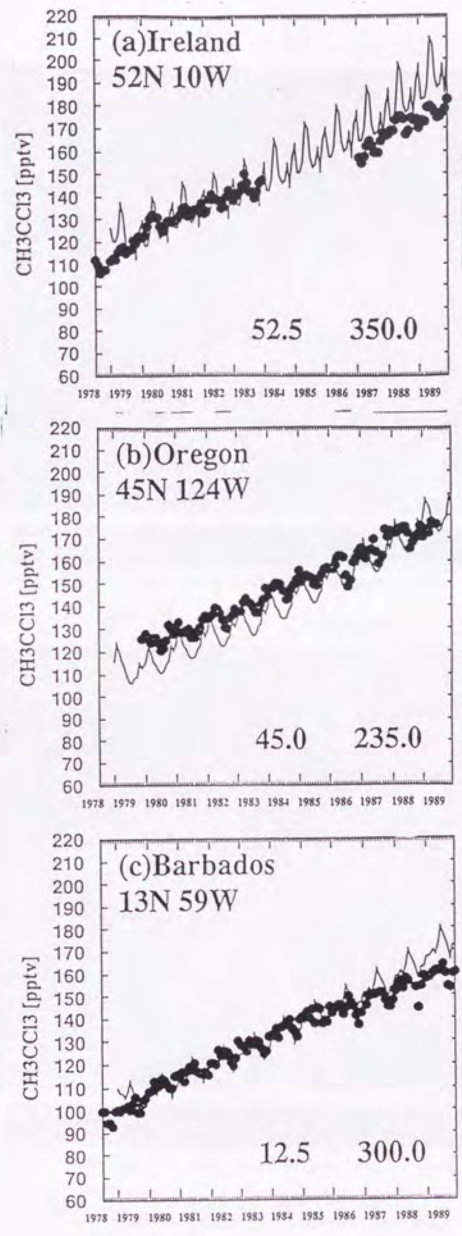

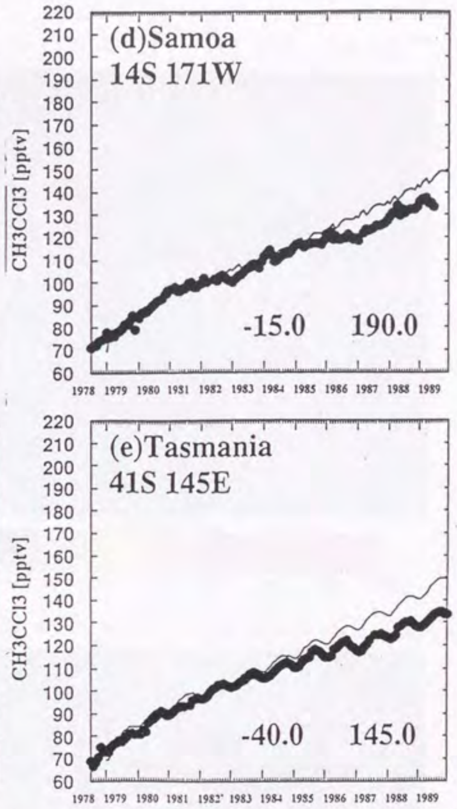

Fig.6:Methyl chloroform concentration recorded at five ALE sites for the period 1978-1983 as reported by *Prinn et al.* [1992] along with corresponding model predictions. (a) Ireland, (b) Oregon, (c) Barbados, (d) Samoa, (e) Tasmania.

CH3CCl3 [pptv]

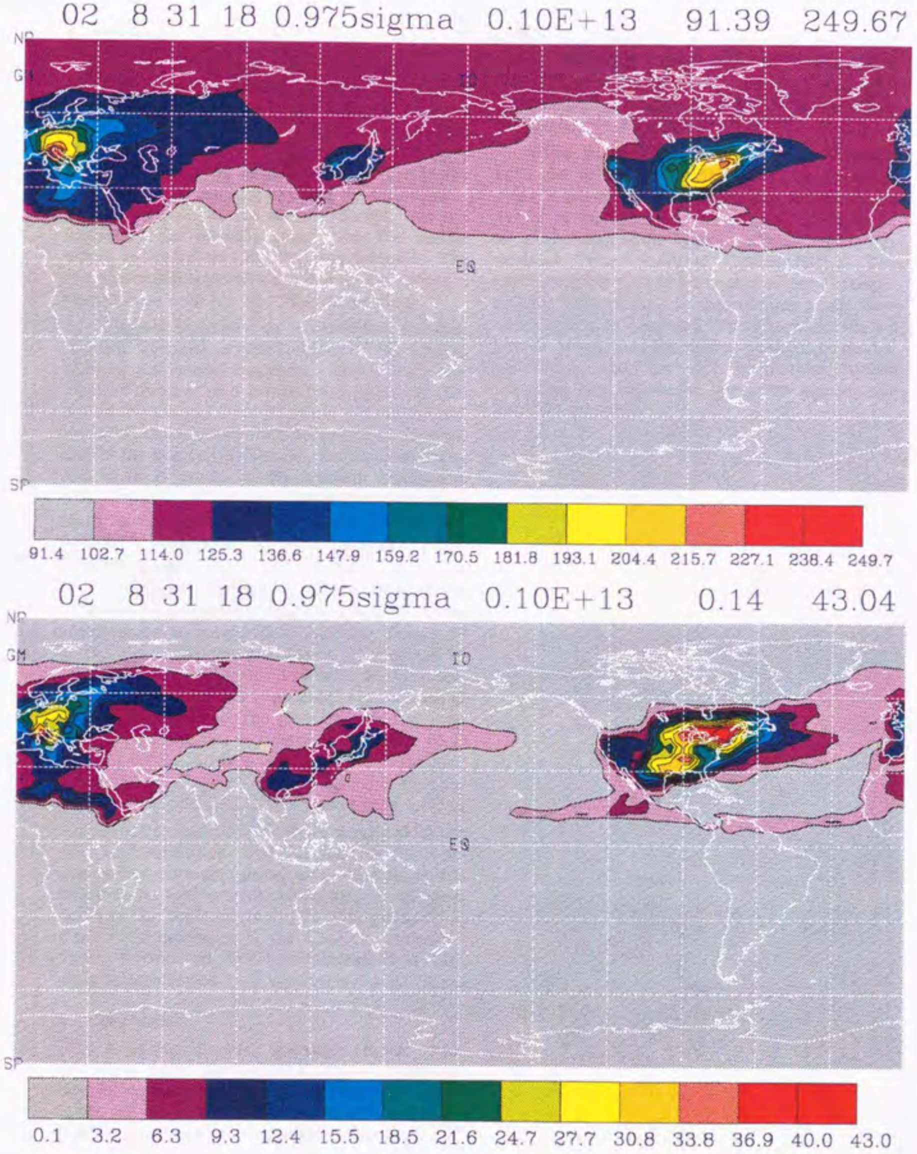

Fig.7:The spatial distribution of methyl chloroform simulated in the model. (a) Monthly average, (b) Standard deviation of the lowest sigma level in August of the second year.

## 5. Methane

A globally homogeneous mixing ratio of 1600 ppbv was assumed as an initial mixing ratio. The source distribution assigned as SF-1 (Table 11) in Taylor *et al.* (1991) was employed in this study (Fig.8). The source strength is calibrated to obtain the amount of 524Tg/yr in the atmosphere in the run without a sink. Interannual variation of the source strength was not included. The monthly zonal mean OH radical value, as scaled to $CH_3CCl_3$, was adopted. The reaction coefficients of Vaghjiani & Ravishankara (1991) were used for the $CH_4$+OH reaction.

Figure 9 shows a comparison between methane at some selected points of the CMDL network and model estimates. In the high latitudes of the northern hemisphere, ((a) alert), the seasonal variation is out of phase. At middle latitudes of the northern hemisphere, ((b) Oregon) and in the tropics ((c) Samoa), the seasonal variation is fairly good. In the southern hemisphere ((d) Tasmania, (e) Syowa), the seasonal variation is compatible with the observations but the base amount is larger than that observed at the CMDL monitoring sites.

At high latitudes in winter the model estimated concentration one is lower than the observations as measured at Alert(a). Figure 10 shows the horizontal distribution of methane in January of seventh year. High latitudes have low concentrations and this is probably not the case in the real atmosphere. The simulated concentration does not exhibit bias at Oregon(b). This is a clear contrast to the $CH_3CCl_3$ case (Fig.7b). If the horizontal gradient around Oregon is smaller than for the $CH_3CCl_3$ case (Fig.8) this explains the bias.

If an increase of OH as is suggested in the $CH_3CCl_3$ simulation were applied in the $CH_4$ simulation, then the global trend in $CH_4$ is not going to be well reproduced as long as methane emission is kept constant. At this point, it is difficult to determine if the $CH_3CCl_3$ emissions should be reduced, OH levels increased or $CH_4$ emissions increased.

## 6. Conclusion

A global tracer transport model was developed using the semi-Lagrangian methodology in conjunction with the ECMWF advanced upper air data set. The calculated interhemispheric exchange time was about one year.

A global distribution of the OH radical amount originally estimated by Spivakovsky *et al.* (1990) was modified to match the amount of methyl chloroform observed at ALE/GAGE sites. The The adjusted OH amount was 4.7 $moledule/cm^3$ which is 36% lower than Spivakovsky's estimates.

The methane distribution was simulated with the OH field derived from the study of methyl chloroform and the source estimation by Taylor *et al.* (1991). The seasonal variation of all sites except at the highest northern hemisphere latitudes was modeled successfully. The interhemispheric contrast was not large enough and the base amount in the southern hemisphere was larger than observed. From these results we plan to investigate the source strength of methyl chloroform and the OH distribution further assuming that the model represents atmospheric transport precisely.

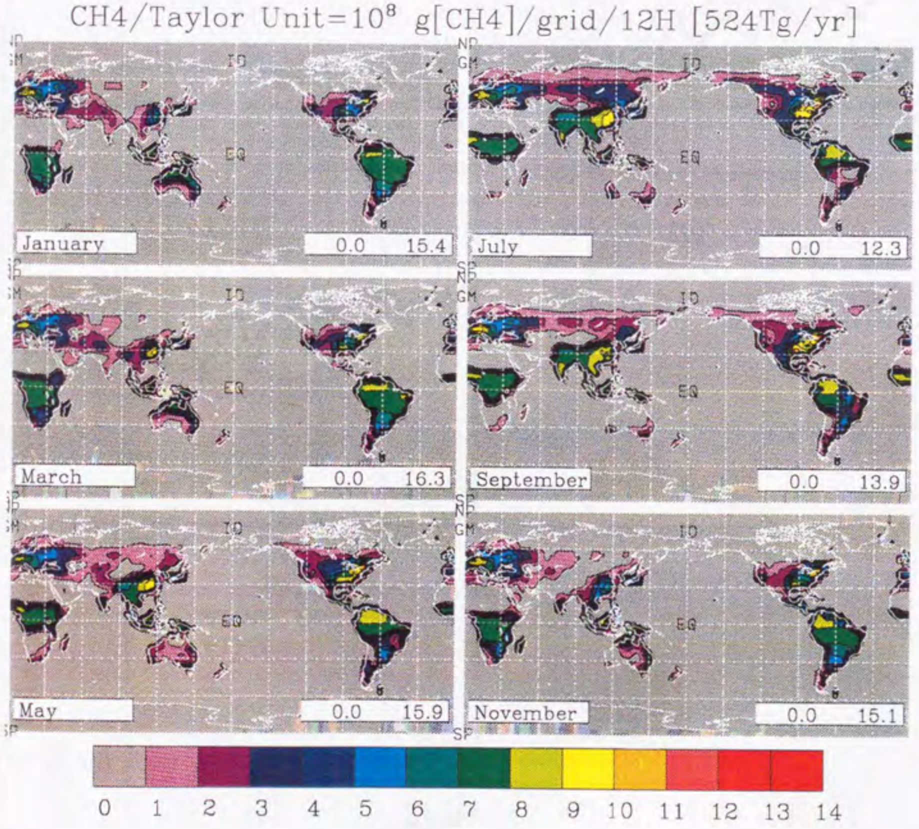

Fig.8:The spatial distribution of the source of methane estimated by *Taylor et al.* [1991].

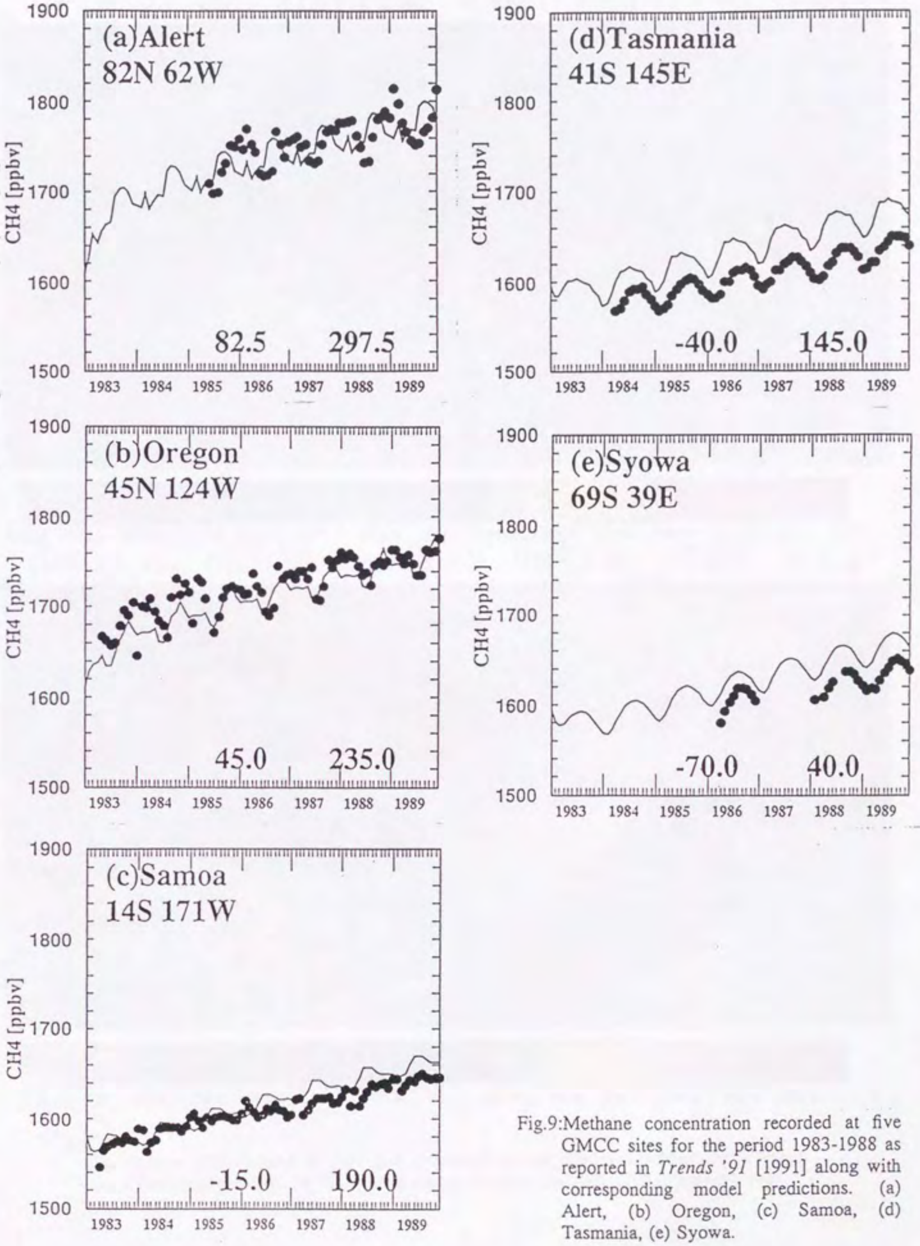

Fig.9:Methane concentration recorded at five GMCC sites for the period 1983-1988 as reported in *Trends '91* [1991] along with corresponding model predictions. (a) Alert, (b) Oregon, (c) Samoa, (d) Tasmania, (e) Syowa.

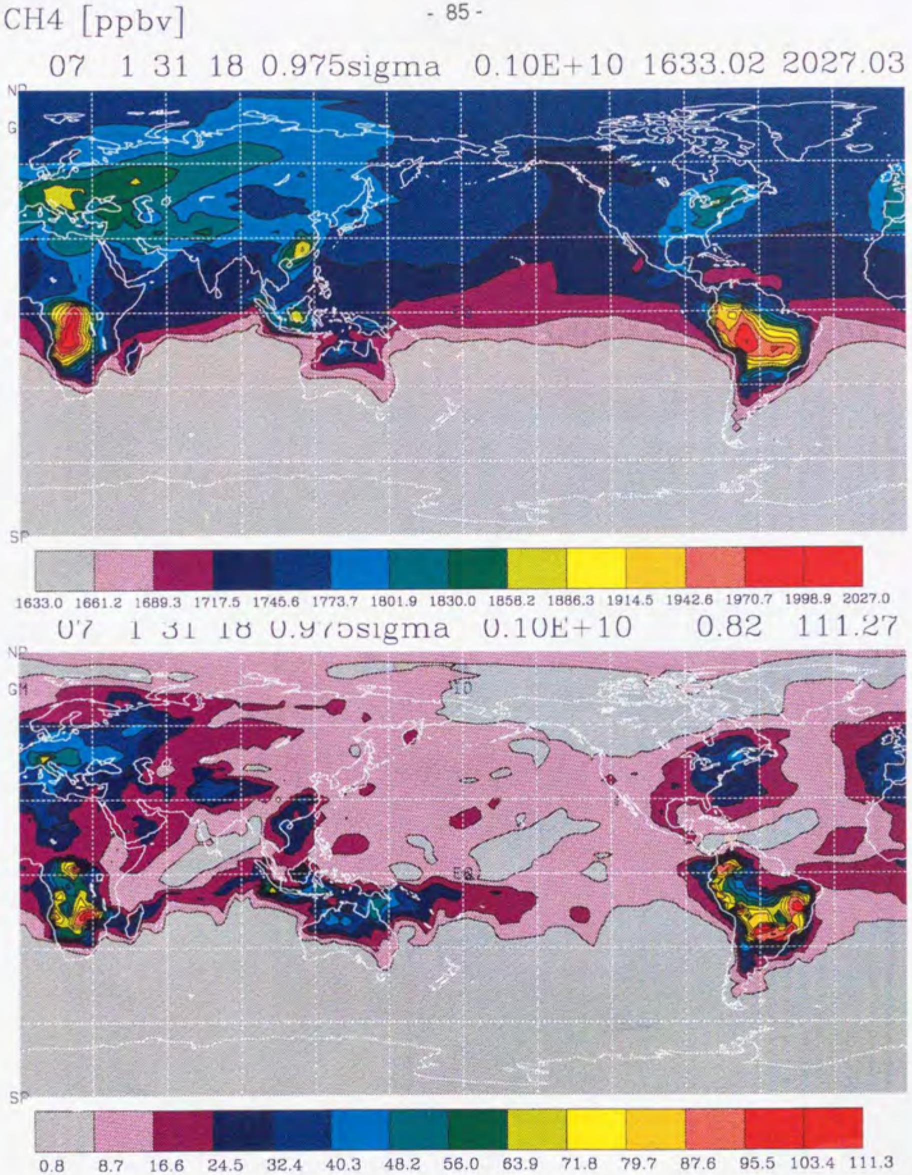

Fig.10:
The spatial distribution of methane simulated in the model. (a) Monthly average, (b) Standard deviation of the lowest sigma level in January of the seventh year.

# Chapter 6: Conclusions

An atmospheric transport model (ATM), a Lagrangian trajectory model(LTM) and a chemical transport model(CTM) were developed using analyzed meteorological data. Both the ATM and CTM were used to analyze the time evolution of the mixing ratio of chemical species in the atmosphere. The LTM was used to examine the trajectories of air parcels. The results obtained in this study may be summarized as follows:

1. All models reproduced the atmospheric barrier in the tropics. The barrier shifted from north to south with the seasons. Longitudinal variations of the barrier were also observed.
2. The ATM and CTM indicate that the inter-hemispheric exchange time is about one year, although the meteorological data were different in each model. The inter-hemispheric gradient of methyl chloroform in the CTM was about 25 pptv which is consistent with the ALE/GAGE observations. This result indicates that the interhemispheric exchange time was well represented in both the ATM and CTM.
3. Three dimensional trajectories for inter-hemispheric exchange processes in January and July were described using the LTM; upper tropospheric paths were found in most cases. An asymmetry was found for the trajectories in the lower troposphere. When one moves from the winter to the summer hemisphere, the Lagrangian trajectories only pass through the lower troposphere. The trajectory from the summer to the winter hemisphere begins in the lower troposphere in the summer hemisphere, is lifted in the tropics and then is transported into the winter hemisphere in the upper troposphere.

This study demonstrated that the ECMWF/TOGA data set represents real atmospheric motion, in terms of the transport of minor constituents using a semi-Lagrangian form for the transport model. Because the TOGA data were provided without normal mode initialization, they still contain gravity wave components. These components are important in the vertical transport in the troposphere, but may cause a problem with the troposphere/stratosphere exchange rate in the CTM. However, this potential problem is outside the scope of the present study.

Based on the study in ATM and LTM, a CTM was developed incorporating a simple PBL and chemical reactions. A source distribution of $CO_2$ estimated from the combustion of fossil fuel was applied in the model. The distribution of the sources and sinks estimated from the land ecosystem model was also used to investigate the three dimensional distribution of the atmospheric $CO_2$. We found that the annual mean surface concentration in the vegetation run is much more sensitive than that in fossil run. This result indicates that the traditional calibration technique to check the inter-hemispheric exchange may not be enough. Assuming the sources and sinks used in this study are correct, we have found that the missing $CO_2$ sink is in the Northern Hemisphere.

The global average of hydroxyl radical concentration was 64% that of the previous study ( Spivakovsky *et al.)*, although the reason is not yet clear. We are expecting that a direct measurement of OH radical amount in the future will help to refine the CTM.

The methane distribution was simulated with the OH field derived from the study of methyl chloroform and the source estimation by Taylor *et al.* (1991). The seasonal variations of all sites, except at the highest northern hemisphere latitudes, were modeled successfully. The inter-hemispheric contrast (100ppbv) was not large enough when compared to CMDL observation (120ppbv). The effect of the PBL representation in the CTM, the seasonal variations of the OH radical amount and the source strengths of methane are possible reasons for this discrepancy. These studies are also outside the scope of the present study.

## Acknowledgements

This study originated with an analysis of synoptic scale disturbances, using analyzed meteorological data. The analysis was performed at the Ocean Research Institute of the University of Tokyo, during the author's tenure as a graduate student. The author is grateful to Professors T. Asai and R. Kimura, both of the Ocean Research Institute of the University of Tokyo, for their encouragement throughout the course of this study. He is also grateful to the staff members of the Environmental Assessment Division of the National Institute for Resources and Environment for their very constructive discussions and support for this study. The auther is indebted to I. Enting (CSIRO), J. Taylor (ANU), P. Tans (CMDL) and M. Takahashi (CCSR/U.Tokyo) for their comments on parts of this manuscript. He also thanks E. Whitney and M. Michalska at the National Institute for Resources and Environment for their fruitful discussions on the manuscript. The author is greatful for I. Fung to Victoria University for her estimate of $CO_2$ sources and sinks, Dr. John A. Taylor(ANU) for his estimated source strength of $CH_4$, Dr. Spivakovsky of Harvard University for her estimated amount of OH, and Dr. Hartley of Georgia Institute of Technology for her estimated source distribution of CFC. Meteorological data were supplied by the European Center for Medium-Range Weather Forecasts (ECMWF). The data of methyl chloroform and methane was provided by the Carbone Dioxide Information and Analysis Center (CDIAC). The calculations were performed on work stations at the Research Information Processing System of the Agency of Industrial Science and Technology (AIST) of the Ministry of International Trade and Industry (MITI). A part of this study was conducted during a short stay in the CSIRO and the ANU. This study was funded by the Global Environment Research Program Budget of the Japan Environment Agency and the Special International Joint Research Project of ITIT/AIST.

## Appendix: List of Acronyms

| | |
|---|---|
| GFDL | Geophysical Fluid Dynamics Laboratory |
| MIT | Massachusetts Institute of Technology |
| GISS | Goddard Institute of Space Studies |
| SIO | Scrips Institute of Oceanography |
| MPI | Max Plank Institute |
| ANU | Australian National University |
| LANL | Los Alamos National Laboratory |
| LLNL | Lowrence Livermore National Laboratory |
| CCM1 | Community Climate Model version one |
| NCAR | National Center for Atmospheric Research |
| CCM2 | Community Climate Model version two |
| NIRE | National Institute for Resources and Environment |

## References

Bengtsson, L., M. Kanamitsu, P. Kallberg, and S. Uppala, 1982: FGGE 4-dimensional data assimilation at ECMWF. *Bull. Amer. Meteor. Soc., 63*, 29-43, 1982.

Bishop, K. F., H. J. Delafield, A. E. J. Eggleton, C. O. Peabody, and B. T. Taylor: The tritium content of atmospheric methane. *Symposium on the detection and use of tritium in the physical and biological sciences*, Vienna, May 1961. Paper No. TTS/79, 1961.

Brasseur, G., P., and S. Madronich: Chemistry-transport models, In *Climate system modeling*, K. Trenberth (ed.) Cambridge University Press, 788pp, 1992.

Brenninkmeijer, C. A. M., M. R. Manning, D. C. Lowe, G. Wallace, R. J. Sparks and A. Volz-Thomas: Interhemispheric asymmetry in OH abundance inferred from measurements of atmospheric $^{14}CO$. *Nature, 356*, 50-52, 1992.

Cunnold, D. M., and R.G. Prinn: Comment on "Tropospheric OH in a three-dimensional chemical tracer model: An assessment based on observations of $CH_3CCl_3$" by C. M. Spivakovsky *et al.*. *J. Geophys. Res., 96*, 17391-17393, 1991.

Czeplak, G., and C. Junge: Studies of interhemispheric exchange in the troposphere by a diffusion model. In *Advances in Geophysics, 18B*, Academic Press ( New York), 57-72, 1974.

ECMWF: The description of the ECMWF/WCRP level II-a global atmospheric data archive. *European Centre for Medium-Range Weather Forecasts*,

Fung, I, J. John, J. Lerner, E. Matthews, M. Prather, L. P. Steele, and P. J. Fraser: Three-dimensional model synthesis of the global methane cycle. *J. Geophys. Res., 96*, 13033-13065, 1991.

Halter, B. C. , J. M. Harris and T. J. Conway, 1988: Component signals in the recoed of atmospheric carbon dioxide concentration at American Samoa. *J.Geophys.Res., 93*, 15914-15918, 1988.

Hartley, D., R. Prinn: Comment on "Tropospheric OH in a three-dimensional chemical tracer model: An assessment based on observations of $CH_3CCl_3$" by C. M. Spivakovsky *et al.*. *J. Geophys. Res., 96*, 17383-17387, 1991.

Hartley D. and R. Prinn: Feasibility of determining surface emissions of trace gases using an inverse method in a three-dimensional chemical transport model. *J.Geophys.Res., 98*, 5183-5197, 1993.

Hartley, D., D. L. Williamson, P. J. Rasch and R. Prinn, Diagnosis of tracer transport in the NCAR CCM2: comparison of $CFCl_3$ simulation with ALE/GAGE observations. *J.Geophys.Res., 99*, 12,885-12,896, 1994.

Heimann, M. and C. D. Keeling, 1989: A three-dimensional model of atmospheric CO2 Transport based on observed winds: 2. model description and simulated tracer experiments. In *Geophysical Monograph, 55*, American Geophysical Union, 237-275, 1989.

Hoskins, B. J., H. H. Hsu, I. N. James, M. Masutani, P.D. Sardeshmukh and G.H. White, Diagnostics of the global atmospheric circulation based on ECMWF analyses 1979-1989. *World Climate Programme*, WMO/TD-No.326, 217 pp, 1989.

Hunt, B. G. and S. Manabe: Experiments witha stratospheric general circulation model. II. Large-scale diffusion of tracers in the stratosphere. *Mon. Wea. Rev., 96*, 503-539,s 1968.

Jacob, D. J., M. J. Prather, S. C. Wofsy and M. B. McElroy: Atmospheric distribution of $^{85}$Kr simulated with a general circulation model. *J. Geophys. Res., 92*, 6614-5526, 1987.

Junge C. E.: Note of the exchange rate between the northern and southern atmosphere. *Tellus, 14*, 242-246, 1962.

Kao, C. K., X. Tie, E. Mroz, D. Cunnold, F. Alyea2: Simulation of the global CFC11 using the Los Alamos chemical tracer model, *Geophys. Res., 97*, 15,827-15,838, 1992.

Keeling, C. G.: The concentration and isotropic abundances of carbon dioxide in the atmosphere. *Tellus, 12*, 200-203, 1960.

Kida, H: General circulation of air parcels and transport characteristics derived from hemispheric GCM. Part 1. A determination of advective mass flow in the lower stratosphere. *J. Meteor. Soc. Japan, 61*, 171-187, 1983a.

Kida, H.: General circulation of air parcels and transport characteristics derived from hemispheric GCM. Part 2. Very long-term motions of air parcels in the troposphere and stratosphere. *J. Meteor. Soc. Japan, 61*, 510-523, 1983b.

Mahlman, J. D. and W. J. Moxim: Tracer simulation using a global general circulation model: results from a midlatitude instantaneous source experiment. *J. Atmos. Sci., 35*, 1340-1374, 1978.

Maiss, M. and I. Levin: Clobal increase of SF$_6$ observed in the atmosphere, *Geophys. Res. Let., 21*, 569-572, 1994.

Kaye, J.A., S.A.Penkett and F.M.Ormond: Report on concentrations, lifetimes, and trends of CFCs, Halons, and related species, *NASA reference publication 1339*, NASA office of mission to planet earth, serveice division, Washington, D.C., 1994.

Newell, R. E., Vincent, D. G. and Kidson, J. W.: Interhemispheric mass exchange from meteorological and trace substance observations. *Tellus, 21*, 641-647, 1969.

Newell, R. E., G. J. Boer and J. W. Kidson: An estimate of the interhemispheric transfer of carbon monoxide from tropical general circulation data. *Tellus, 26*, 103-107, 1974.

Pearman, G. I. and P. Hyson: Activities of the global biosphere as reflected in atmospheric co2 records. *J. Geophys. Res., 85*, 4457-4467, 1980.

Pierrehumbert R. T. and H. Yang: Global chaotic mixing on isentropic surfaces. *J. Atmos. Sci., 50*, 2462-2480, 1993.

Plumb R. A. and J. D. Mahlman: The zonally averaged transport characteristics of the GFDL general circulation/transport model, *J. Atmos. Sci., 44*, 298-327, 1987.

Prather, M., M. McElroy, S. Wofsy, G. Russel and D. Rind, Chemistry of the global troposphere: Fluorocarbons as tracers of air motion. *J. Geophys. Res., 92*, 6579-6613, 1987.

Prather, M *ed.*: WCRP workshop on long-range transport of trace gasses 10-14 December 1990: Special numerical experiment: Simulation of $CFCl_3$ as a test for 3-D atmospheric models. World Meteorological Organization, (*in preparation* ).

Prinn, R., D. Cunnold, R. Rasmussen, P. Simmonds, F. Alyea, A. Crawford, P. Fraser and R. Rosen, Atmospheric trends in methylchloroform and the global average for the hydroxyl radical. *Science, 238*, 945-950, 1987.

Prinn, R., D. Cunnold, P. Simmonds, F. A.yea, R. Boldi, A. Crawford, P. Fraser, D. Gutzler, D. Hartley, R. Rosen, and R. Rasmussen2: Global average concentration and trend for hydroxyl radicals deduced from ALE/GAGE trichloroethane ( Methyl Chloroform ) data for 1978-1990. *J. Geophys. Res., 97*, 2445-2461, 1992.

Schiavone J. A., and T. V. Papathomas: Visualizing meteorological data. *Bul. Ame. Met. Soc., 71*, 1012-1020, 1990.

Shaw, D. B., P. Lonnberg, A. Hollingsworth and P. Unden, Data assimilation: The 1984/85 revisions of the ECMWF mass and wind analysis. *Quart. J. Roy. Met. Soc.*, 113, 533-566, 1986.

Spivakovsky, C. M., R. Yevich, J. A. Logan, S. C. Wofsy, M. B. McElroy, and M. J. Prather: Tropospheric OH in a three dimensional chemical trace model: An assessment based on observations of CH$_3$CCl$_3$. *J. Geophys. Res., 95*, 18441-18471, 1990.

Staniforth, A. and J.Cote: Semi-Lagrangian integration schemes for atmospheric models - A review. *Mon. Wea. Rev., 119*, 2206-2223, 1991.

Taguchi, S.: Inter-hemispheric exchange in the troposphere by an atmospheric transport model based on observed winds. *J. Meteoro. Soc. Japan, 71*, 123-135, 1993.

Taguchi, S.: Cross Tropical trajectories in the troposphere. *J. Meteoro. Soc. Japan, 72*, 531-553, 1994.

Taguchi, S. and J.A. Taylor: A simulation of Methane and Methyl Chloroform using the NIRE global three-dimensional tracer transport model, *Proceedings of the International Symposium on global cycles of atmospheric greenhouse gases*, 319-332, 1994.

Tanaka, M., T. Nakazawa and S. Aoki, Time and space variation of upper tropospheric carbon dioxide over Japan, Tellus, 39B, 3-12, 1991.

Tans, P. P., T. C. Conway and T. Nakazawa, Latitudinal distribution of the sources and sinks of atmospheric carbon dioxide derived from surface observations and an atmospheric transport model. *J. Geophys. Res., 94*, 5151-5172, 1989.

Taylor, J.A., A stochastic Lagrangian atmospheric transport model to determine global CO$_2$ sources and sinks - a preliminary discussion, *Tellus, 41B*, 272-285, 1989.

Taylor, J. A.: A study of the sources and sinks of methane and methyl chloroform using a global three-dimensional Lagrangian tropospheric tracer transport model. *J. Geophys. Res., 96*, 3013-3044, 1991.

Trenberth, K. E.: Climate diagnostics from global analyses: Conservation of mass in ECMWF analyses. *J. Climate, 4*, 707-722, 1991.

Trenberth, K. E.: Global analyses from ECMWF and atlas of 1000 to 10mb circulation statistics. *NCAR Tech. Note, NCAR/TN-373+STR*, Boulder, CO., U.S.A., 191pp., 1992.

Trenberth, K. E.,and J. G. Olson: ECMWF global analyses 1979-1986: Circulation statistics and data evaluation. *NCAR/TN-300+STR* , Boulder, CO., U.S.A., 94pp, 1988.

Troen IB., L. Mart, A simple model of the atmospheric boundary layer; sensitivity to surface evaporation, *Boundary Layer Meteorology, 37*, 129-148, 1986.

*Trends'91: A Compendium of data on global change*, Carbon dioxide information analysis center, Oak Ridge National Laboratory, Oak Ridge, Tennessee, T. A. Boden, R. J. Sepansk and F. W. Stoss, ed., 1991

Unden P., Tropical data assimilation and analysis of divergence. *Mon. Wea. Rev., 117*, 2,495-2,517, 1989.

Watterman, L. S., D. W. Nelson, W. D., Komhyr and T. B. Harris: Atmospheric carbon dioxide measurements at cape matatula. *J. Geophys. Res., 94*, 14,817-14,829, 1989.

Waugh, D. W.: Contour surgery simulations of a forced polar vortex. *J. Atmos. Sci., 50*, 714-730, 1993.

Williamson D. L. , J. T. Kiehl, V. Ramanathan, R. E. Dickinson and J. J. Hack: Description of NCAR Community Climate Model (CCM1). *NCAR Tech. Note, NCAR/TN-285+STR*, Boulder, CO., U.S.A., 112pp, 1987.

Williamson D. L. and P. J. Rasch: Two-dimensional semi-Lagrangian transport with shape-preserving interpolation. *Mon. Wea. Rev., 117*, 102-129, 1989.

Yamazaki, K., The statistical analysis of long-term trajectory calculation based on the observed data. *J. Meteor. Soc. Japan, 70*, 1167-1173, 1992.

Yamazaki, K., and M. Chiba: The transport simulation of passive tracers from the northern hemisphere to the southern hemisphere. *Proc. NIPR Symp. Polar Meteoro. Glaciol., 5*, 9-23, 1992.

Yamazaki, K. and M. Chiba: A 3-D global simulation of the advective transport of passive tracers from various northern hemisphere sources. *Tellus, 45B*, 160-178.

Zimmermann, P.H., J.Feichter, H.K.Rath, P.J.Crutzen and W. Weiss, A global three-dimensional source-receptor model investigation using $^{85}$Kr. *Atmospheric Env., 23*, 25-35, 1989.